NORTHWESTERN UNIVERSITY

Coupling Quantum Emitters and Plasmonic Nanocavities for Energy Transfer and Lasing

A DISSERTATION

SUBMITTED TO THE GRADUATE SCHOOL

IN PARTIAL FULFILLMENT OF THE REQUIREMENTS

for the degree

DOCTOR OF PHILOSOPHY

Field of Applied Physics

By

Weijia Wang

EVANSTON, ILLINOIS

March 2018

Abstract

Plasmonic nanocavities consisting of metal nanoparticle (NP) arrays support surface lattice resonances (SLR) or lattice plasmon, emerged as an exciting platform for manipulating light-matter interactions at the nanoscale. Their recent prominence can be attributed to a combination of desirable photonic and plasmonic characteristics: high electromagnetic field enhancements extended over large volumes with long-lived lifetimes. Chapter I provides an overview on design rules for achieving high-quality optical responses from metal nanoparticle arrays, nanofabrication advances that have enabled their production, and the theory that inspired their experimental realization. Rich fundamental insights will focus on weak and strong coupling with molecular excitons as well as semiconductor excitons and the lattice resonances. As another powerful application of SLR, lattice plasmon lasers will be discussed in detail on theoretical modeling and experimental characterization. Finally, prospects and questions will be discussed.

This thesis is mainly focused on ultrafast dynamics of lattice plasmon coupling with excitons in various light emitting materials. In Chapter II, we used metal NP arrays in square lattice as plasmonic nanocavities for lasing action. Cold cavity lifetime measurements showed picosecond scale lifetime of lattice plasmon, indicating their long-range scattering feature. In contrast to the femtosecond lifetime of surface plasmons, lattice plasmons can dramatically slow down the group velocity of light and enable significant optical feedback for stimulated emission. We also identified amplified spontaneous emission (ASE) as an energy transfer channel co-existing with lasing in periodic laser cavities. Side-by-side spectral and temporal investigation on ASE and lasing reveal how coherence of stimulated emission builds up in the system.

In Chapter III, we introduce a new lattice geometry that sustains dual-mode SLR. This provides a platform for investigating self-selective exciton-plasmon coupling under the influence of two lattice plasmons with spatially distinct nano-optical field enhancement. We fabricated and characterized optical properties of NPs arranged in rectangular lattice. FDTD simulations showed that the dual-mode SLR has two orthogonal dipolar field enhancement distributions. With organic dye molecules as gain medium, switchable dual-mode lasing with clear threshold behavior and identical plasmonic lasing dynamics was investigated. The dual-mode lasing does not have mode competition which could be applied for on-chip multiplexing.

Besides changing the plasmonic nanocavity design, we also explore the new selection of quantum emitters that can interact with lattice plasmons. Chapter IV and Chapter V introduce two types of new emitters: metal-organic frameworks (MOFs) and colloid quantum dots (QDs). Transient absorption measurements characterized the formation of hybrid exciton-plasmon modes in (MOF) conformally coated around plasmonic nanoparticle arrays, which led to mode splitting in spectra. The splitting energy of the modes could be tailored by the detuning of SLR in different index-environments from a single nanostructured materials system. We also demonstrated mode splitting in photoluminescence, that contributed to the faster recombination from the electrons in the hybrid states. Strong enhancement of the emission, over 16-times stronger than that of the pristine Zn-porphyrin, was achieved. Our results established MOFs as a type of molecular emitter materials with great promise to couple with plasmonic nanostructures for energy exchange and transfer.

QDs are proposed to serve as gain medium in the prototype of plasmonic lasers. However, few reported on achieving plasmonic lasing with QDs, due to non-radiative process in QDs hindering

their application in lasing applications. Chapter V demonstrates a new type of biaxial strained QDs that enables the plasmonic lasing actions. Specifically, the QD plasmonic lasing emission was investigated through light-light curve and showed a decrease of lasing threshold compared to waveguide structure. Time-resolved emission dynamics also exhibited the typical rising time feature in plasmonic systems, indicating the ultrafast energy transfer process. Material dependence study further confirm that the plasmonic component of the SLR was attributing to lasing actions.

Acknowledgement

First and foremost, I would like to thank my two advisors, Prof. Teri Odom and Prof. George Schatz for their continuous support and guidance during my Ph.D. study. Teri is an incredible researcher from whom I learnt how to effectively conduct impactful research and convey the ideas to the broader audience in forms of manuscripts and presentations. Especially as a female scientist, she showed me a great example of balancing life and work. George has always enlightened me on the fundamental science in pursuit of my tough research questions. He flourishes me with his extensive knowledge and discussing science with him has always been an intellectual pleasure. I am very lucky to have both of them as my advisors.

Besides my advisors, I would like to thank the rest of my thesis committee: Prof. Lincoln Lauhon and Prof. Nathaniel Stern for their insightful comments on my research proposal and projects, to help me approach my research from a wider perspective. Also, I would like to thank Prof. Rich Schaller who helped me with the experimental set-up in Argonne national lab. From him I learnt how to operate femtosecond laser and design optical experiments. He has always been generous with his time and worked with us even at late hours during the long day every time we visited the national lab.

I would like to acknowledge my collaborators who made the work in this dissertation possible: Dr. Ankun Yang, Dr. Jianxi Liu, Ran Li, Danqing Wang, Yuanhai Lin, Dr. Fengjia Fan, Dr. Oleksandr Voznyy and Prof. Edward Sargent. I am also grateful for colleagues in Odom and Schatz groups for the enjoyable time. My special thanks go to Dr. Jae Yong Suh, Dr. Ankun Yang, Dr. Montacer Dridi who trained me when I first joined the groups, and Dr. Steven Lubin, Dr. Yi

Hua, Dr. Mark Huntington, Dr. Alex Hryn, Dr. Claire Deeb, Dr. Jian Zhang, Michael Knudson, Jingtian Hu, and Dr. Daniel Park, whom I worked closely with.

PhD study is an odyssey, but I have been lucky enough to have friends who joined this journey and shared the moments of laughter and tear with me. Dr. Vince Cho, Dr. Bryan Lau, and Emily Sprague-Klein have been greatly helping me pursue academic advances. Catherine Zhong, Beier Yao, Cloudy Liu, Danny Tan, Tony Yang, Dr. Andy Li, Ann Liu, Conifer Guo, Grace Li, Ivy Li, Minzhou Jin, Tianyi Li, Xiaofeng Zhu, Patrícia Anzini, Dr. Eunhye Song, Antz Yang, Dr. Siyu Chen, Dr. Huajun Chen, Dr. Felix Amankona-Diawuo, Ran Xia, Theodore Ren, Michael Hammerman, Edward Hsieh and Steven To brought colors into my life.

Last but not the least, I would like to thank my parents, Aogang Wang and Peiming Shang for their endless care and support. Also, thanks my lovely cat friends Cheesecake, Spade, Hermes, and beloved Mulan.

List of Abbreviations

NP Nanoparticle

SLR Surface Lattice Resonance

ASE Amplified Spontaneous Emission

MOF Metal-Organic Framework

CQD Colloidal Quantum Dots

PL Photoluminescence

DL Dipolar

QL Quadrupolar

LSP Localized Surface Plasmon

SPP Surface Plasmon Polariton

FDTD Finite-difference Time-domain

PDMS Poly(dimethylsiloxane)

DMSO Dimethyl Sulfoxide

BA Benzyl Alcohol

NIR Near-infrared

CDA Coupled Dipole Approximation

FEM Finite Element Method

TA Transient Absorption

SEM Scanning Electron Microscope

AFM Atomic Force Microscope

Dedication

My dearest En Na

Table of Contents

List of Figures

CHAPTER I. THE RICH PHOTONICS WORLD OF PLASMONIC NANOPARTICLE ARRAYS

1.1. Introduction

Nanophotonics encompasses the manipulation of light at the nanoscale and has flourished in the past two decades because of a confluence of integrated advances in materials, nanofabrication, and modeling.[1] In particular, plasmonics, the resonant interaction of light with metals,[2,3] has driven much of the recent attention because of unprecedented optical properties and a wide range of unique applications.[1,4,5] Starting with the early work of Michael Faraday on gold nanocolloids [6] and stained glass windows in medieval churches,[7] the beautiful colors produced by "finely-divided" gold and other metal nanoparticles have been of high interest. Metal nanoparticles (NPs) exhibit localized surface plasmon (LSP) excitations, coherent oscillations of free electrons[8-10] whose optical response can be tailored by size, shape, and materials of the nanostructures.[11,12] LSPs can lead to large local electromagnetic field enhancements in deep sub-wavelength volumes;[13] if the NPs are in very close proximity, their near-fields can couple and further confine the fields.[14,15] The properties of these nearly-touching NPs have been used in a wide range of applications from spectroscopy to sensing and catalysis.[16-19]

Compared with individual and small clusters of NPs, metal particles organized into ordered arrays with spacings comparable to the wavelength of light can produce even greater field enhancements and higher quality resonances by exploiting short and long-range interactions.[20] Long-range (radiative) coupling between LSPs of single NPs can be mediated by two classes of photonic modes: diffraction modes in the plane of the array[21-28] and guided modes in supporting dielectric slabs.[29] Diffraction-mode coupling requires a uniform dielectric environment around the metal NPs to produce surface lattice resonances (SLRs, also called lattice plasmons), while guided-mode coupling generates waveguide polaritons or quasi-guided modes. The primary reason why

SLRs have gained prominence is their combination of desirable photonic and plasmonic attributes: high field enhancements characteristic of plasmonic nanostructures extended over large volumes and having long-lived lifetimes from photonic features.[30]

In this Chapter, we summarize the recent advances in plasmonic NP arrays and offer prospects for future emerging applications. First, the general design principles of NP array characteristics and corresponding linear optical properties will be established. Different classes of SLRs will be described by experiment and theory. Second, weak and strong coupling regimes between organic dye molecules and SLRs will be reviewed. Third, the use of SLRs as optical feedback for entirely new classes of nanoscale lasers will be discussed. Fourth, interactions between electronic materials and SLRs will be compared with organic dyes. Finally, broad applications of SLRs from sensing to solid-state lighting will be introduced.

1.2. Linear Optical Properties of Nanoparticle Arrays

1.2.1. Sample Preparation

High-quality SLRs require an optimized combination of NP unit cells and lattice geometry. Direct-write methods such as electron-beam lithography[23] are advantageous to design arbitrarily shaped nanostructures and were the first approaches to produce NP arrays that could support SLRs.[23,28] Serial processes, however, have challenges in scaling the array areas and in overall production costs, which has limited wide-spread dissemination and new applications. Parallel nanofabrication methods that use poly(dimethylsiloxane) (PDMS) stamps such as PEEL (**P**hotolithography + **E**-beam deposition + **E**tching + **L**ift-off) and Surface Conformal Imprint Lithography (SCIL) have opened opportunities to generate large-area (>10 cm^2) arrays of NPs. In

PEEL, free-standing metal thin films perforated with nanoholes[31] function as physical deposition masks to create NP arrays in a range of materials and shapes determined by the hole mask (**Figure 1.1a**). **Figure 1.1b** is a SEM image of Au nanohole array film partially peeled off from Al NP

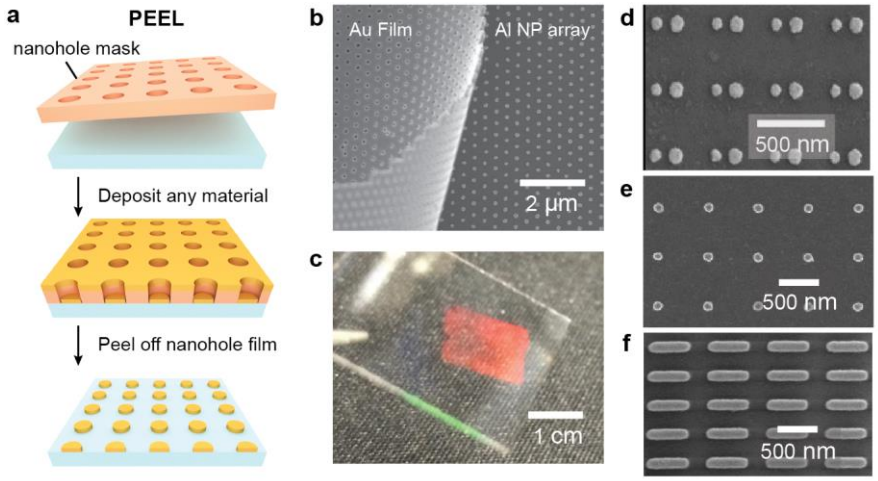

Figure 1.1 Nanoparticle array fabrication. (**a**) Scheme of using metal hole-array film as a deposition mask in the PEEL method. Reproduced with permission from [31]; copyright 2007 *Nature Publishing* (**b**) Scanning electron microscope (SEM) image of metal nanohole array film (partially peeled off) with NP array on a substrate. Reproduced with permission from [36]; copyright 2016 *National Academy of Sciences*. (**c**) Optical image of Au NP arrays that cover > 1 cm^2 (red diffraction pattern). Reproduced with permission from [34]; copyright 2015 *Nature Publishing*. (**d**) Ag dimer NP array fabricated by e-beam lithography. Reproduced with permission from [39]; copyright 2016 *American Chemical Society*. (**e**) Au monomer NP array fabricated by PEEL. Reproduced with permission from [34]; copyright 2015 *Nature Publishing.* (**f**) Au nanorods fabricated by SCIL. Reproduced with permission from [40]; copyright 2009 *American Physical Society*.

arrays. **Figure 1.1c** is an optical image of typical areal sizes (> cm^2) of NP arrays produced by PEEL. This masking method can also be extended to create NP superlattices with microscale arrays of finite-arrays of NPs (patches).[32] In SCIL, flexible stamps are used to replicate the lattice pattern in sol-gel on a substrate. This pattern combined with metal deposition and lift-off can produces wafer- scale arrays of metal NPs.[33]

Tuning the optical response for a fixed set of NP array parameters can be achieved by changing the refractive index environment[34,35] or by patterning NPs into mechanically stretchable materials such as PDMS.[36] Most SLR studies have focused on NP arrays made from Au and Ag because of their strong optical responses over the visible and near-infrared (NIR) wavelengths; arrays made from Al, however, have recently been shown to support lattice resonances with very high quality over the entire UV to NIR range[33,36-38] **Figure 1.1d-f** highlight different NP shapes, from NP dimers[26,39] to cylindrical NPs[34] to nanorods[40] whose arrays have produced SLRs. The ultra-narrow resonances (down to a few nm in experiments[30,34]) can be dipolar[26-28,32,34,36,41] or quadrupolar[36,39,42] in character depending on the geometric properties of the NPs and their coupled diffraction mode order.

1.2.2 Theory of Strongly Coupled Nanoparticle Arrays

Many years before strongly coupled NP arrays could be realized experimentally, Markel,[43] Carron,[44] and Schatz[21,22,24,25] predicted SLRs and provided design rules regarding how to optimize the ultra-narrow (< 1 nm) linewidths. The coupled dipole approximation (CDA) is most often used to understand the coupling between NPs in arrays, where each particle is treated as a single dipole resonator with polarizability α_{NP} depending on material, size and shape.[28] At the resonant condition, all NPs oscillate in phase, and NPs sit in the antinodes of standing wave formed in the plane of the lattice. Because diffractive scattering of photons by each NP can excite the LSPs of adjacent NPs instead of decaying into free space, the lattice resonances suppress radiative loss. Assuming the induced polarization in each NP is the same, the effective array polarization can be treated as the sum (S) of the incident and radiated fields from all other dipoles in the array. When the real part of ($1/ \alpha_{NP} - S$) vanishes, the imaginary part of the dipole sum is also reduced, and then a narrow

resonance peak arises in the extinction spectra. The SLR condition only exists at the longer-wavelength side of the diffraction mode where constructive interference results in a standing wave across the NPs.[21,28]

For larger NPs that support higher-order plasmon modes (beyond dipolar modes),[45] CDA cannot capture the appropriate physics; however, a model where the NPs are considered as electric dipole and quadrupoles independently can resolve this issue.[46] The discrete dipole approximation, where NPs are represented by polarizable cubes that include higher-order excitations, can also predict lattice resonances with higher-order modes.[47] Besides analytical models, numerical methods such as finite-difference time-domain (FDTD)[48] approaches and finite element methods (FEM)[49] solve Maxwell's equations on a meshed grid and can generate not only far-field spectra but also near-field properties such as phase, field intensity, and charge distribution of the electromagnetic field components. Near-field information is critical to identify the origins of SLR excitations.

1.2.3 Different Classes of Surface Lattice Resonances

Dipolar lattice resonances. Figure 1.2a highlights SLRs from a 2D square Au NP array (d = 120 nm, p = 600 nm) that exhibit very narrow linewidths (3-4 nm; quality factor $Q = \lambda/\Delta\lambda$ of ~200) at normal incidence ($\theta = 0°$). Like other plasmonic nanostructures,[12] NP arrays that support lattice resonances are sensitive to changes in refractive index. At higher indices, the SLR shifts to longer wavelengths, and at lower indices, the resonance shifts to shorter wavelengths.[34] Although the optimal SLRs result when the superstrate and substrate are index matched,[50] the collective lattice modes are tolerant to small mismatches ($\Delta n \sim 0.05$).[34] From FDTD simulations, at $\theta = 0°$ or zero *in-plane* wavevector ($k = 0$), the near-field regions around the NPs show a characteristic dipolar

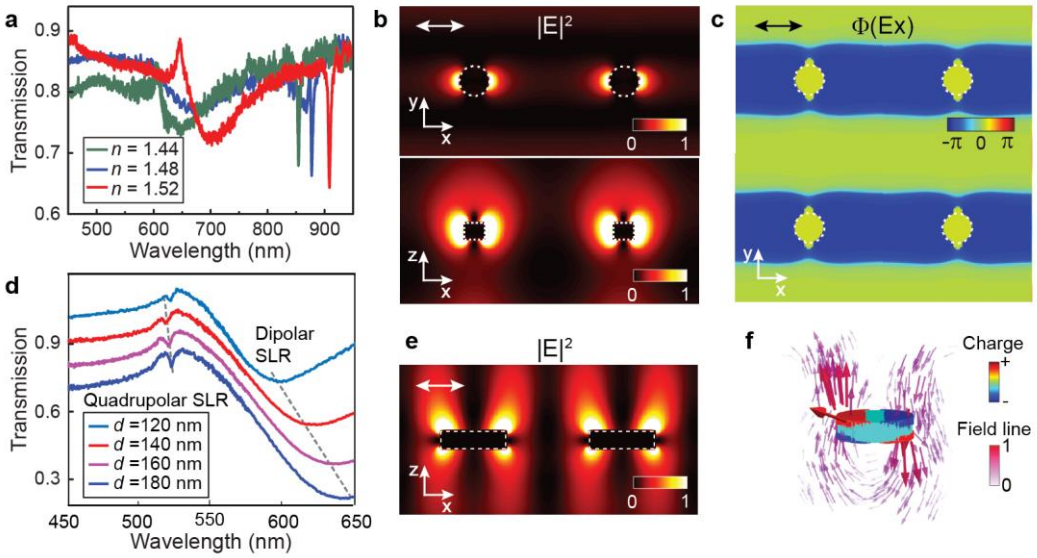

Figure 1.2 Dipolar and quadrupolar surface lattice plasmons. (**a**) Transmission spectra of Au NP array (2D square lattice, p = 600 nm, d = 120 nm, h = 50 nm) surrounded by different refractive index environments. SLRs red-shifted with increasing refractive index. Reproduced with permission from [34]; copyright 2015 *Nature Publishing*. (**b**) Simulated electric field pattern at SLR shows dipolar pattern. (**c**) Simulated phase information of E along x direction at the SLR. All NPs are oscillated in phase and formed a standing wave. Reproduced with permission from [53]; copyright 2013 *Nature Publishing*. (**d**) Transmission spectra of Al NP array (2D hexagonal lattice, p = 346 nm, n = 1.5) with increasing NP diameter. Both dipolar and quadrupolar SLRs were present when d >120 nm. Simulated (**e**) near-field pattern and (**f**) charge distribution at *out-of-plane* quadrupolar SLRs in (d). Field enhancement and charges distributed at four corners of the NP. Reproduced with permission from [36]; copyright 2016 *National Academy of Sciences*.

pattern with enhancements two to three orders of magnitude larger than the incident light, concentrated at opposite sides of NPs in the direction of polarization (**Figure 1.2b**). The neighboring NPs oscillate with the same phase and form a standing wave across the lattice perpendicular to the polarization (**Figure 1.2c**).

SLR modes can have either *in-plane* or *out-of-plane* character depending on NP geometry. The primary factor determining *in-plane* dipolar lattice modes is NP diameter.[34,36] For example, as 2D square NP diameter decreased from 120 nm to 60 nm, the LSP of the individual NPs blue-shifted towards a diffraction mode, and hence the SLR linewidth dropped from 30 nm to 5 nm (Q ~ 108).

Out-of-plane dipolar modes can be tuned by controlling NP height, and a minimum NP height is required.[41] For NPs with similar diameters and heights > 100 nm, both *in-plane* and *out-of-plane* dipolar LSPs coupled to the array structure, resulting in a Fano resonance within a broad resonance background.[41] The sharp resonance was associated with the *out-of-plane* component and sensitive to changes of NP height, while the broad resonance peak was from the *in-plane* component.

Quadrupolar lattice resonances. Progress in the fabrication of larger NPs such as rods[42] or cylinders[36] has made possible the observation of high-order SLRs. Because of their net zero dipole moment, quadrupolar resonances can only weakly interact with light (i.e. they are "dark" in optical far-field measurements) and are rarely observed.[51,52] In arrays of long Au rods (L= 420 nm), *in-plane* quadrupolar coupling between NPs can produce narrow resonances on a dipole background. The subradiant (dark) character led to much higher Q (>700) compared with radiant (bright) counterparts.[42] In contrast, for arrays of cylindrical Al NPs ($d \geq 120$ nm), *out-of-plane* quadrupole lattice resonances can be excited along with *in-plane* dipolar lattice plasmon modes[36] but with very different qualities (**Figure 1.2d**). To optimize the *out-of-plane* quadrupole lattice modes, the dipolar LSP must be detuned from the diffractive coupling condition. The electric near-field intensity and charge distribution of a quadrupole SLR (**Figure 1.2e-f**) show distinct characteristics different from dipolar SLRs.

Unit cells composed of NP dimers offer an alternative method to induce multi-polar resonance coupling in arrays[24] since the hot spot intensity in the gaps depend on polarization. Interestingly, in arrays of asymmetric disc dimers,[39] the plasmon modes can hybridize and produce two different modes with dipole moments on adjacent NPs either in-phase or out-of-phase with each other. The broken-symmetry of the dimers introduced radiative coupling of the dark mode to free-space light.

The dark mode related to the SLR exhibited one sharp resonance in addition to the one associated with the bright mode. Unlike quadrupolar SLRs in long nanorods that were not observed under normal incidence light, the asymmetric NP dimers sustain a non-vanishing net dipole moment and do not require oblique excitation to provide additional momentum for coupling to the far-field.

Superlattice plasmons. Lattices with hierarchical microscale structure (arrays of patches) can support extremely high-order diffractive mode coupling because of the microscale periodicity (10-25 μm).[32] Superlattice SLRs can be significantly narrower than finite-area NP arrays (patches) and exhibit stronger local fields. When shape and size of the NP units are kept constant, superlattice SLRs showed a linewidth reduction from 35 nm to 3 nm, and the localized near-field enhancement around the NPs increased from 10- to 40- fold depending on patch-patch spacing. Spectral separation between superlattice SLRs can be tuned by the Bragg modes defined by the microscale periodicity. Compared to SLRs from single-lattice arrays, superlattice SLRs share the same dominant modes (although scattering orders are different) with new satellite resonances at longer wavelengths with separations up to 120 nm.

1.2.4 Dispersion Diagrams of Coupled Nanoparticle Arrays

One significant advance that resulted from the fabrication of macroscale areas (> cm^2) of NPs is that photonic dispersion diagrams can easily be constructed. Different from LSP resonances in isolated particles, SLRs from NP arrays are dispersive because they originate from diffraction modes. Samples illuminated with collimated white light under transverse magnetic (TM) or transverse electric (TE) polarization at different incident angles can result in a wavelength vs. angle (θ) map (**Figure 1.3a-b**) that can also be plotted as an energy vs. in-plane wavevector (*k*)

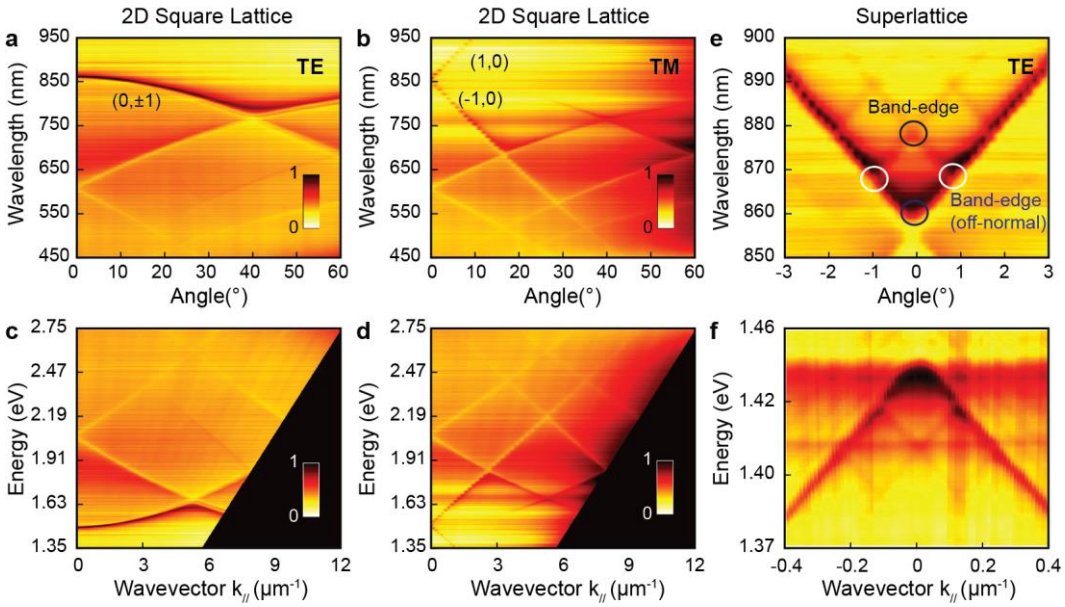

Figure 1.3 Dispersion diagrams of SLRs in single-lattice and superlattice arrays. SLRs in 2D square Au NP arrays (*p* = 600 nm, *d* = 120 nm, *h* = 50 nm, *n* = 1.44) follow (**a**) (0, ±1) diffraction modes under TM polarization and (**b**) (1,0) (-1,0) diffraction modes under TE polarization. (a), (b) can be converted to energy vs wavevector as shown in (**c**), (**d**). Reproduced with permission from [34]; copyright 2015 *Nature Publishing.* (**e**)-(**f**) Au superlattice supports off-normal band-edge modes and higher order SLR modes in the dispersion diagram. New band-edge mode emerged at off normal angles (white circled) because of patch-patch coupling. Reproduced with permission from [82]; copyright 2017 *Nature Publishing.*

dispersion diagram (**Figure 1.3c-d**). Under TM-polarized light, the dispersion of SLRs from 2D square arrays of cylindrical Au NPs follow the (0, ±1) diffraction orders at slightly red-shifted wavelengths, and these diffraction orders are degenerate. [34,40,53] Under TE-polarized light, SLRs follow (1,0) and (-1,0) diffraction orders. For superlattice SLRs, the TE modes had opposite *k*-vectors, equivalent to two waves propagating in opposite directions. At off-normal angles, the two *k*-vectors cancel to generate new modes in the dispersion diagram where the net *k*-vector is zero (**Figure 1.3e-f**). At a band-edge (or at any *net* zero wavevector), superlattice SLRs sustain a high local density of optical states (LDOS), which opens prospects to manipulate light-matter interactions including photoluminescence (PL) modification, nanoscale lasing, nonlinear optical processes, and quantum optics.[54,55]

Dispersion diagrams can also be measured with a *k*-space setup where the image of the back-focal plane is focused on a spectrometer slit to resolve angular energy distributions of transmitted light. Angular energy maps directly represent the in-plane momentum relation of NP arrays. Very different dispersion diagrams have been recorded from arrays fabricated into square, rectangular, hexagonal, honeycomb, and *Lieb* lattices.[56]

1.3 Strong and Weak Coupling Effects with Organic Molecules and Materials

Surface lattice resonances offer unique prospects for coupling with quantum emitters. Different from LSP resonances of single NPs, the collective lattice modes can support high-quality cavities and directional radiation.[57] The large LDOS and high intensity in the localized EM hot spots can affect the strength of light-matter interactions resulting in two broad categories: weak or strong coupling regimes.

1.3.1. Weak Coupling: Shaping the Fluorescence Emission

Organic molecules are attractive for testing fundamental interactions with lattice resonances because of their large dipole moments, solubility in polymers and solvents, and diversity in their emission and absorption wavelengths.[58] Minor drawbacks include their limited stability under high excitation intensities. Enhancement of the fluorescent emission was observed from arrays of long Au nanorods (Figure 1f) coated with a 50-nm polymer matrix containing ATTO 680 fluorescent molecules (0.01 mM).[59] When the pump polarization was along the short axis of the nanorods (**Figure 1.4a**), the fluorescence increased by seven-fold, and the enhanced emission followed the SLR coupled to the (1,0) diffraction mode (**Figure 1.4b**). Excited dye molecules preferentially decay into SLRs because the high LDOS improves light extraction. Similarly, when pump

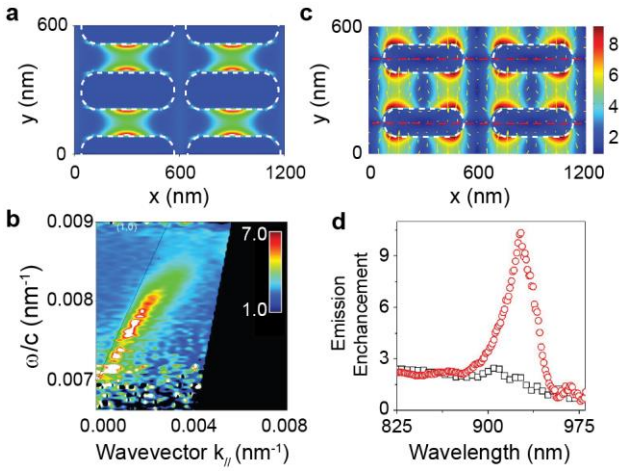

Figure 1.4 Weak coupling between SLRs and dyes at low concentration. (a) Simulated near-field map of an SLR excited along the short axis of the Au NPs. (**b**) Measured fluorescence of dye molecules (ATTO 680 dispersed in a polyvinyl butyral (PVB) matrix with concentration of 10^{-5} M) combined with the Au NP array, normalized by the emission from dyes on an unpatterned substrate. Reproduced with permission from [59]; copyright 2009 *American Physical Society*. (**c**) Simulated near-field map of a SLR excited along the long axis of the NP. (**d**) Emission enhancement at 0° (RA, black dots) and 20° (quadrupolar SLR, red dots). Reproduced with permission from [45]; copyright 2010 *American Physical Society*.

polarization was parallel to the long axis of the nanorods (**Figure 1.4c**), the quadrupolar SLR coupled to the (0,1) diffraction order also contributed a ten-fold enhancement in fluorescence.[45] Because quadrupolar LSPs are dark, off-normal detection was required. Fluorescence enhancement was much smaller if only photonic modes were considered (**Figure 1.4d**).

1.3.2. Strong Coupling with Organic Dye Molecules

The strong coupling regime is defined as when energy exchange rates of the interacting entities are faster than loss rates.[60] Energy exchange in time results in a splitting of the resonant energy in frequency into the so-caller lower and upper polariton bands. The splitting, called Rabi splitting, can be visualized as an avoided crossing in the dispersion diagram, where modes of the uncoupled system intersect. Rabi splitting must be larger than the linewidths of the uncoupled modes and is directly proportional to the dipole moment of the emitter and square root of dye concentration.[60]

Although strong coupling between surface plasmon polaritons and molecular excitons has been observed,[60,61] interactions between SLRs and organic emitters offer opportunities to explore the effects of collective modes with long life-times. For example, strong coupling was observed between Ag NP arrays and high concentrations (200 mM) of Rhodamine 6G (R6G),[62,63] which involved three different types of excitations: lattice plasmons, LSPs, and molecular excitons. Avoided crossings between the diffraction modes and LSP resonance can be seen in the dispersion diagram (**Figure 1.5a,** blue dots), with coupling strengths of 107 meV and 142 meV between the LSP and the first-order and second-order diffraction modes. Rabi splitting on the order of 100 meV between the R6G excitons and the LSP as well as the LSP and the two diffraction modes can also be observed (Figure 1.5a, red dots), but direct coupling between R6G excitons and diffraction

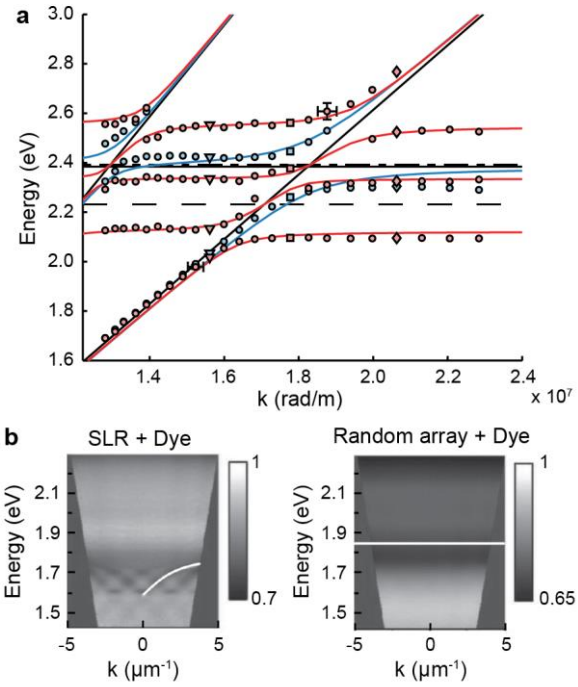

Figure 1.5 Strong coupling between SLRs and dyes at high concentration (**a**) Dispersion of the extinction spectra. Blue dots present the extinction maxima with the bare Ag NP array only, and red dots represent the extinction maxima when 200 mM of R6G in a 50-nm thick PMMA layer was added on top. Blue and red solid lines are fits with a three- and five-coupled modes models, respectively. Horizontal solid line indicates single-particle resonance, dashed and dashed-dotted lines the R6G main absorption peak and absorption shoulder, respectively. Reproduced with permission from [62]; copyright 2014 *American Chemical Society*. (**b**) Interference fringes with double slits experiment of (left) 800 mM DID on Ag NP array showing SLR and (right) 800 mM DID dye with a random NP array. Reproduced with permission from [64]; copyright 2014 *American Physical Society.*

modes was negligible. Notably, coupling between dyes and SLRs was mediated by the LSP component of the lattice modes.

Strong coupling between SLRs and molecular excitons also implies that distant emitters in the lattice can be spatially coherent. When emitters strongly couple to SLRs, the hybrid modes are expected to show properties of both constituents. Organic dyes coupled to Ag nanorod arrays were

found to be spatially coherent,[64] with strong coupling between excitons and the SLRs (150 meV) since the molecular absorption was below the LSP wavelength. In a double-slit set-up, interference fringes were measured in the dispersion diagram of the dye with NP arrays, which indicated spatial coherence (**Figure 1.5b**). Evolution of spatial coherence from strong to weak coupling was achieved by decreasing the dye concentration, and coherence lengths *L* of 6-10 μm were extracted both in weak and strong coupling regimes. Notably, these long coherence lengths were maintained even when the hybrid mode was very exciton-like due to existence of the SLR component in the hybrid.

1.3.3. Strong and Weak Coupling to Generate Condensates

In systems of inorganic and organic semiconductors combined with microcavities, hybrids of strongly coupled excitons and cavity modes (exciton-polaritons) have been shown to condense into a ground state that forms a macroscopic coherent quantum state.[60,65,66] Radiative recombination of exciton-polaritons can produce coherent emission similar to lasing, thereof called polariton lasing. Polariton lasers do not require population inversion, and hence the thresholds can be very low. Exciton-polariton condensates, including both Bose-Einstein condensates (BECs) and polariton lasing, and physical phenomena originating from non-linear interactions of exciton-polaritons are significant. In plasmonic NP arrays, strong light-matter coupling of excitons to SLRs can also produce hybrid light-matter quasiparticles.[60] The possibility of thermalization of exciton-polaritons, the redistribution of energy towards lower values and ultimately condensation,[65] has been demonstrated in NP arrays,[67] and polariton lasing has been observed,[68] which paves the way for strongly coupled condensates. Recently, a BEC in the weak coupling regime was observed in a plasmonic NP array.[69]

1.4. Nanoscale Plasmon Lasing

One of the most powerful applications of the properties of SLRs is their use as unconventional nanolasing cavities. The concept of a plasmonic nanolaser was first introduced as a spaser (surface plasmon amplified stimulated emission of radiation),[70] in which quantum emitters resonantly transferred their energy to plasmon excitations, and then the highly localized EM fields would lead to stimulated emission. Although plasmon lasing was first realized in hybrid waveguide modes—in a tour-de-force result—from semiconducting nanowires coupled to surface plasmon polaritons in supporting metal films, this architecture (nanowire plasmonic lasers) had some disadvantages, including high absorption loss of plasmonic films, operation at low temperatures,[71,72] and special geometric designs to decrease internal losses.[73]

NP arrays supporting SLRs integrated are an ideal nanocavity for nanoscale lasing because of their ultra- narrow linewidths and sub-wavelength localized field enhancement around the NPs.[21,26,28] Despite the absence of closed cavity walls, slow light can be trapped at the SLR band-edge (k = 0) with a standing wave formed across the lattice because of in-phase oscillations of dipole moments from each NP (Figure 1.2b-c). The array structure enables the amplified plasmons to be converted into free-space light and result in spatially coherent emission in the direction normal to the arrays.[74]

1.4.1. Lasing from Single-lattice Nanoparticle Arrays

Distributed feedback lasing has been observed by incorporating weakly coupled Au NP arrays (no SLR) in a polymer waveguide, although emission was not related to the NP LSP.[75] Lattice plasmon lasing action—where the lasing signal was at the same wavelength as the SLR mode—was first reported at room temperature in 2D arrays of Au and Ag NP arrays embedded in polymer

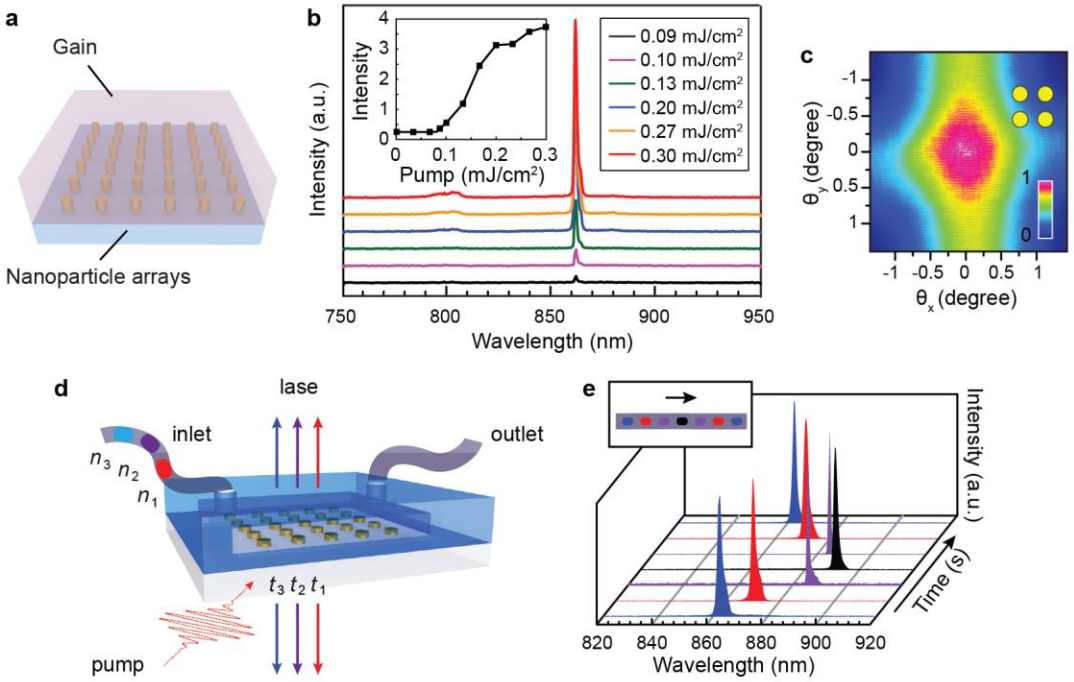

Figure 1.6 Lasing action from strongly-coupled plasmonic NP arrays (**a**) Scheme of a lattice plasmon laser consisting of Au NP array embedded in liquid or solid-state gain media. Reproduced with permission from [53]; copyright 2013 *Nature Publishing*. (**b**) Power-dependent lasing emission signal and input-power output intensity curves (inset). Lasing signal had a critical threshold. (**c**) Far-field beam profile with a highly directional lasing spot. Reproduced with permission from [34]; copyright 2015 Nature Publishing. (**d**) Scheme of the dynamic laser with a microfluidic channel. (**e**) Continuous shifting of lasing emission to longer wavelengths and then back to shorter wavelengths. Reproduced with permission from [34]; copyright 2015 Nature Publishing.

matrix filled with IR-140 organic dye.[53] When the dye was optically pumped by 800-nm fs pulses, excitons resonantly transferred their energy into the collective plasmon mode. The lasing emission showed a critical threshold behavior (~ 0.23 mJ/cm^2).[53] This architecture is general, and lasing was also observed with NP arrays coated with a different dye (R6G) dye in polymer.[76] The thresholds of lattice plasmon lasers can be decreased by dissolving the dye gain in organic solvents (**Figure 1.6a-b)**. Not only were the molecules solubilized and more uniformly distributed, but because of

Brownian motion, the dye in the EM hotspots was constantly being refreshed.[34] **Figure 1.6c** shows that the lasing signal exhibited high directionality normal to the surface with low divergence angle (< 1.5°). Exploiting the refractive index tolerance of SLRs between substrate and superstrate[50] enabled in dynamic control of lasing action.(**Figure 1.6 d-e**) Real-time nano-lasing tunability was achieved when Au NP arrays were integrated into a microfluidic device over the entire bandwidth of the dye ($\Delta\square$ = 50 nm) when different liquid gain materials surrounded the NP arrays.(Figure 1.6e)

A semi-quantum mechanical simulation method treating the four-level electronic system of the dye quantum mechanically and SLR excitations by Maxwell's equations revealed the microscopic details of lasing action.[53,77] **Figure 1.6d** shows that when an external pump excited gain, population inversion built up between states 2 and 1, and the energy of the excitons was resonantly transferred to plasmons to result ultimately in far-field emission. Time-evolution of the population inversion was characterized by rate equations modified with the total EM fields in the system. Macroscopic polarization of the EM fields modified absorption and emission of dyes, and the self-consistent interactions between dye emission and EM fields were modeled to simulate the lasing process. **Figure 1.6e** indicates that below lasing threshold, the stimulated emission rate was negligible compared to the spontaneous emission rate; above threshold (**Figure 1.6f**), however, the stimulated emission rate become orders of magnitude higher. One critical finding of this semi-quantum model was that deep-subwavelength regions of population inversion were co-localized within the EM hotspots—only gain in the vicinity (ca. 25 nm) of plasmonic NPs contributed to the lasing action.

1.4.2. Lasing from Finite Nanoparticle Arrays

Finite NP arrays provide an out-coupling mechanism for dark modes into the far-field because of dipolar radiation effects at the array edges.[78] **Figure 1.7a** shows that as the pump power increased, an intense narrow emission peak at the upper energy mode appeared first, and then a second peak at lower energy mode emerged later. The stronger lasing peak at higher energy can be attributed to the dark mode above the array diffraction lines, while the weaker lasing peak at lower energy was from the bright mode below the diffraction lines (**Figure 1.7b**). These two modes showed distinct far-field emission patterns (**Figure 1.7c**); the upper mode was a hybrid mode that showed radiative character of bright dipolar modes at the edges and a dark quadrupole mode in the center of the array. The lower energy mode showed radiation mainly from the center of the single patch, where the dipole moments of the NPs were maximized.

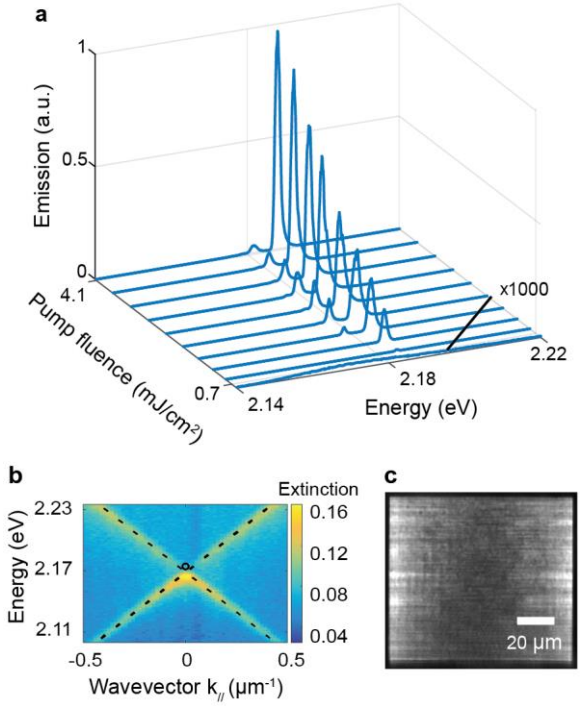

Figure 1.7 Lasing from both bright and hybrid dark modes in Ag finite-sized NP arrays (**a**) Power-dependent lasing emission from bright and dark modes in finite-sized Ag NP arrays. (**b**) Dispersion diagram. Black circle marked the dark mode with zero wavevector. (**c**) Real space far-field beam profile of hybrid dark mode lasing which is mostly visible at the edges of the finite-sized array (white area). Reproduced with permission from [78]; copyright 2017 *Nature Publishing.*

1.4.3. Superlattice Plasmon Lasing

Because the position of the SLR can result in plasmon lasing at the same wavelength,[34,53] the ability to create multiple SLRs can result in controlled multi-mode nanolasing. Precise control of multiple lasing modes within a single device is critical for next-generation opto-electronics and can facilitate nano-scale multiplexing and optical processing.[79-81] Superlattice SLRs in hierarchical NP arrays (**Figure 1.8a**) produce multi-modal lasing peaks at positions that can be understood by a detailed understanding of the contributing band-edge modes.[82] Multiple lasing peaks at λ_{SL}^{I}, λ_{SL}^{II}

and λ_{SL}^{III} with large modal spacing ($\Delta\lambda$ = 10 nm) and ultra-narrow linewidths (<0.5 nm) were

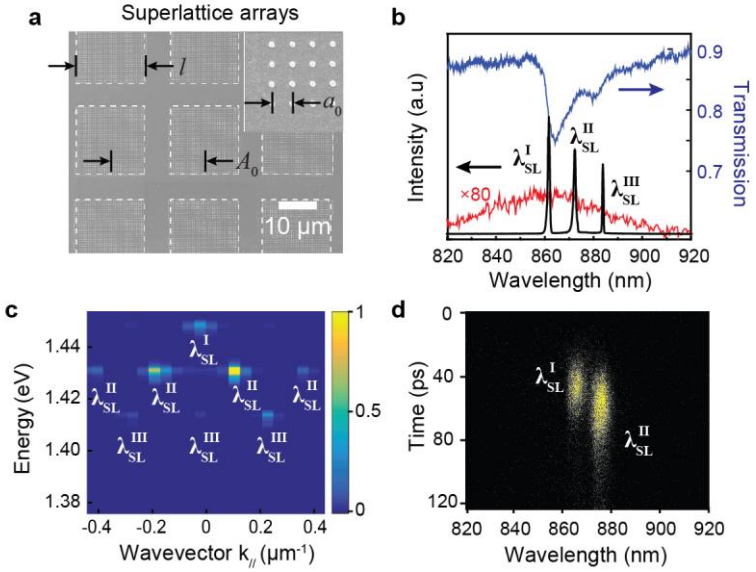

Figure 1.8 Multi-modal nanolasing in NP superlattices (**a**) SEM image of Au superlattice arrays with NP spacing a_0 = 600 nm, patch side length l = 18 μm and patch periodicity A_0 = 24 μm. (**b**) Lasing emission profile (black curve), dye emission profile (red curve), linear optical properties (blue curve). (**c**) Angle-resolved emission spectra of multi-modal lasing. (**d**) Life time measurements of the multiple lasing modes by time-correlated single-photon counting. Reproduced with permission from [82]; copyright 2017 *Nature Publishing.*

observed from NP superlattices (length l = 18 μm, patch periodicity A_0 = 24 μm) surrounded by IR140-DMSO (**Figure 1.8b**). Comparing transmission spectra of superlattice NPs at θ = 0° with their lasing spectra, λ_{SL}^{I} and λ_{SL}^{III} can be correlated in a straightforward manner with the two superlattice SLRs; however, the passive mode corresponding to lasing at λ_{SL}^{II} was missing. Dispersion diagrams revealed that λ_{SL}^{II} could be attributed to new band-edge modes at non-zero wavevectors (**Figure 1.8c**). Hence, the lasing mode λ_{SL}^{I} had origins similar to that of the single lasing mode in single-lattice NP arrays,[34,53] and λ_{SL}^{II} and λ_{SL}^{III} were lasing modes attributed to patch-patch coupling. The formation of band-edge modes at non-zero wavectors is unique to plasmonic

systems (vs. pure photonic) because of strong near-field coupling between patches. Variations in patch periodicity resulted in controlled lasing modes from different band-edge states, and changes in NP sizes could manipulate the input-output light-light behavior of the different modes.

Below lasing threshold, spontaneous emission from dye molecules surrounding the NP arrays showed a small reduction in decay lifetime because of the Purcell effect (800 ps). Above threshold, only two lasing wavelengths λ_{SL}^{I}, λ_{SL}^{II} were observed at this pump power because the multi-modal lasing was power-dependent (λ_{SL}^{III} was not visible under this condition) (**Figure 1.8d**). A significant reduction of lifetime was observed at both lasing modes because of fast stimulated emission. λ_{SL}^{I} showed decay lifetimes similar to single-lattice NP arrays (~13 ps), but λ_{SL}^{II} had a longer decay lifetime (~ 41 ps) because the patch-patch mode could trap photons for longer times. Interestingly, λ_{SL}^{I} emerged earlier than λ_{SL}^{II} because of the overall stronger near-fields at λ_{SL}^{I}. These dynamics studies demonstrated that the photonic features of the superlattice SLRs allowed for longer photon lifetimes in the cavities and better optical feedback, while the plasmonic features resulted in faster population inversion build up around the NPs in the EM hotspots.

1.4.4 Amplified Spontaneous Emission from Nanoparticle Arrays

Lattice plasmon based laser systems provide a unique platform to study competing effects between lasing action and amplified spontaneous emission (ASE) simultaneously. ASE is often a prerequisite to test whether a gain material can support stimulated emission.[83] In nanowire plasmonic lasers, ASE occurred as a transitional stage between spontaneous emission and lasing as the pump intensity was increased.[84,85] Because both ASE and lasing originated from the same hybrid waveguide mode,[84] they occurred at the same wavelength, even though the lasing peak was much narrower.

In lattice plasmon lasers, however, ASE arose from the propagating lattice plasmon modes that followed the Rayleigh anomalies and emitted at off-normal angles[9] (**Figures 1.9a-b**). Individual NPs no longer oscillated in phase as in the case of band-edge lattice modes, and a well-defined wavefront was formed in the plane of the array.[53] Hence, propagating lattice modes provided less optical feedback and resulted in ASE instead of lasing action. Interestingly, increasing the pump intensity well above lasing threshold resulted in a decrease of lasing peak intensity in Au and Ag lattice plasmon lasers[53] (**Figure 1.9c**). This reduction in lasing signal can be attributed to ASE emerging at off-normal emission angles following the diffraction mode (not dye degradation). Different from nanowire plasmonic lasers, NP array lasers produced ASE at higher thresholds than lasing. At high pump powers, the ASE decay lifetime became comparable with that of the lasing

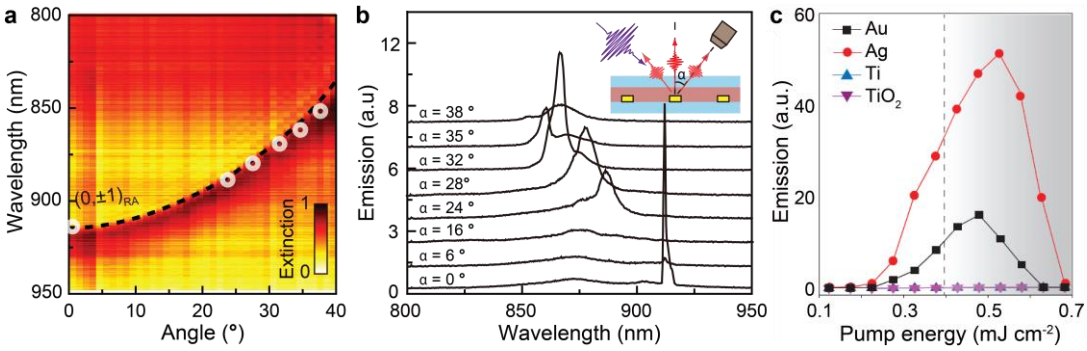

Figure 1.9 Amplified spontaneous emission (ASE) functioned as another decay channel besides lasing in gold NP arrays (**a**) Angle-dependent ASE. (**b**) ASE originated from dispersive modes that followed the Rayleigh anomalies. (**c**) Input-power output-intensity curves from spaser NP arrays with different materials. Figure adapted from ref. 53 with permission; copyright 2013 *Nature Publishing*.

signal,[34] which indicates ASE is a preferable and competing energy output channel under these conditions.

1.4.5 Theoretical Modeling of Plasmonic Lasing

Plasmon lasers have been predicted and inspired by theoretical models based on cavity mode analysis; however, there are remaining challenges in understanding and modeling lasing action in plasmonic cavities. In Purcell factor calculations, the traditional definition of mode volume *V* fails because the EM fields diverge exponentially away from the plasmonic cavity; a more accurate definition of *V* such as that in effective mode-volume theory is needed.[86,87] To understand lasing action, models need to include equations describing populated states in gain and how population inversion induces stimulated emission in the presence of the plasmonic cavity.

Dye photophysics can be described by a four-level electronic state model, and the optical cavity treated with classical electrodynamics.[88,89] In the classic work of Nagra and York,[90] who developed a theory where the FDTD method was used to numerically solve the EM fields, finite differencing was also used to describe rate equations and coupling between the field and populations. Related approaches have been applied to plasmon lasers[53,91,92] and expanded to non-plasmonic systems such as photonic crystals and random lasers.[93-98] The Nagra-York model[90] as well as variations that account for Pauli exclusion principle effects[94] have now been combined with standard FDTD codes, including commercial solvers like COMSOL and Lumerical and the public domain code MEEP.[99]

Using a semi-quantum time-domain approach,[53,92,100] lattice plasmon lasing can be simulated by stimulated energy transfer from the gain to the band-edge modes of the plasmons (**Figure 1.10a**). The lattice plasmon response from NP arrays can be described by classical electrodynamics, and Maxwell's equations can be solved numerically. Integration between the EM fields and gain can be described in auxiliary equations including both the macroscopic polarization of EM fields from

population inversion and the time evolution of the population density of the gain modified by EM fields. Overall, the rate equations, Maxwell's equations, and auxiliary equations can be solved by finite differencing on an FDTD grid[90] to determine emitted power as a function of pump energy.

Below lasing threshold, the stimulated transition rate is negligible compared to the spontaneous emission (**Figure 1.10b**). Above lasing threshold, the stimulated emission rate was four orders of magnitude higher than the spontaneous emission rate. A spatial map of the stimulation emission revealed that population inversion leading to lasing action had maximum values in hot spot regions within 25 nm of the NPs, which was in excellent agreement with the near-field EM patterns at the band-edge plasmon resonance. This calculation confirmed that the nanoscale localization of EM fields stimulated excited state gain to resonantly transfer energy into surface plasmons.

Describing gain material merely by evolution of rate equations is incomplete in their treatment of coherence effects. At high dye concentration, the dye excitons may dephase, transfer energy to each other, or be quenched close to the metal NPs. Recently, more sophisticated models describing

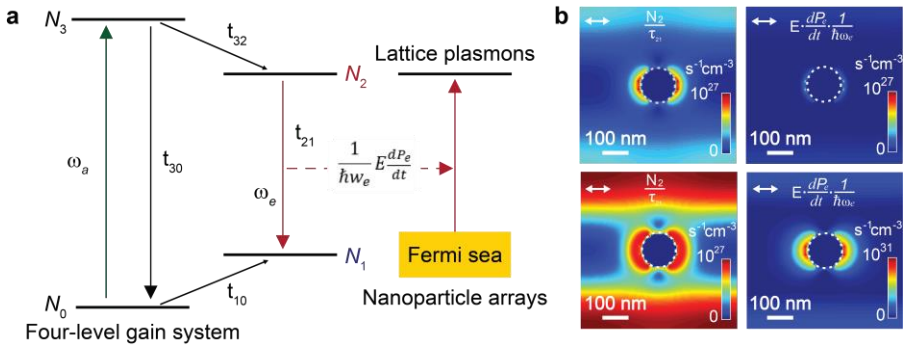

Figure 1.10 Modeling of nanoscale energy transfer with semi-quantum four-level system for lasing action. (**a**) Scheme of the energy transfer process from four-level gain media to lattice plasmon resonances in spaser NP arrays. (**b**) Calculated distribution maps of spontaneous transition rate (left) and stimulated transition rate (right) in the middle plane of NP arrays below threshold (top) and above threshold (bottom). Reproduced with permission from [53]; copyright 2013 *Nature Publishing*.

emitter photophysics have been based on the classical picture of oscillating dipoles, and quantum pictures include phonon and electron-phonon coupling as well as excited state dynamics. Time-evolution of the quantum density matrix of the emissive species can describe the dephasing of emitter states,[101] and the Maxwell-Liouville approach and variants have already been applied to non-lasing plasmonic systems.[102-108] New theoretical models can provide insight into plasmonic lasing processes and motivate experimental studies on fundamental light-matter interactions.

1.5. Interactions with Electronic Materials

Recently, strongly coupled NP arrays have been integrated with electronic materials, including 2D transition metal dichalcogenides (TMDs),[109] carbon nanotubes (CNTs),[110] and hexagonal boron nitride (hBN). Like their organic counterparts, inorganic materials exhibit a range of distinct properties, from modified photonic band structures to enhanced single-photon emission.

Single-layer TMD materials (2D TMDs) exhibit unique optical and electronic properties. As the dimensionality of the semiconductors is reduced, the electronic band gap changes from indirect to direct.[111] Their large exciton binding energies, which results in efficient light emission and large absorption cross-sections, offers possibilities for Wannier-Mott exciton (delocalized) coupling to SLRs. Importantly, Ag NP arrays could be fabricated by e-beam lithography on single-crystalline MoS_2 flakes without damage (**Figure 1.11a**). In the dispersion diagram, the SLR was visible along with the avoided crossing of the exciton-polariton bands in the strong coupling regime.[109] Compared to the case of strong coupling with dye molecules (localized excitons) with energies on the order of 150 meV, the measured coupling strengths were 10-20 meV; however, long-range

SLRs provide coupling of MoS_2 with plasmonic resonances beyond the length scales of individual NPs.

Semiconducting carbon nanotubes (CNTs) can emit light at wavelengths that depend on their chirality and surface ligands,[112,113] but applications in optical devices have been hindered from

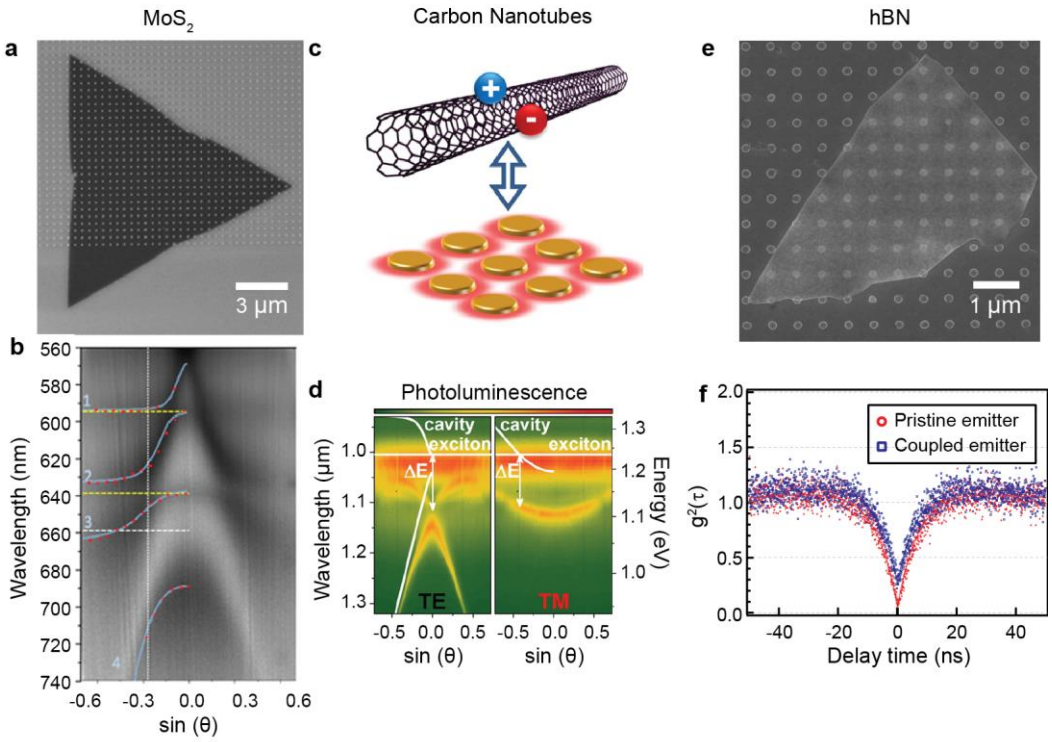

Figure 1.11 Electronic materials coupled to NP arrays (**a**) SEM image of monolayer MoS_2 below Ag NP array. (**b**) Angle-resolved reflectance spectra of the sample in (a). Reproduced with permission from [83]; copyright 2016 *American Chemical Society.* (**c**) Scheme of a carbon nanotube coupling with Au NP arrays. (**d**) Dispersion measurements showing the strong coupling of excitons in carbon nanotubes to different SLRs. Reproduced with permission from [84]; copyright 2016 *American Chemical Society*. (**e**) SEM image of hBN on top of a Ag NP array. (**f**) $g^{(2)}$ measurements comparing pristine hBN and hBN coupled with SLRs. Single photon emission is preserved in the coupled system. Reproduced with permission from [90]; copyright 2017 *American Chemical Society*.

their low PL efficiency (<0.1%).[114] CNTs can be dried into mats of random networks so their

excitons can couple to both TE and TM SLRs of Au NP arrays. A top coating layer of 150-nm poly(methyl

methacrylate) for index-matching the glass substrate to preserve high-quality SLRs. In the weak coupling regime,[115] CNT emission was tailored by SLRs to achieve broadband tunable emission. In the strong coupling regime,[110] high concentrations of CNTs resulted in hybridization of excitons and SLRs with coupling strengths (Rabi splitting) of 120 meV (**Figure 1.11b**).

Another electronic material that was recently coupled to SLRs is 2D hexagonal boron nitride (*h*-BN), whose defects can show room-temperature single-photon emission. To understand how the single-photon emission changed in the presence of SLRs, defect locations within the flake were first determined by PL imaging, and then the same *h*-BN flake was assembled on 2D arrays of Ag and Au NPs. This deterministic coupling resulted in enhanced PL emission by 2-3 fold because of the Purcell effect and with a corresponding reduction in decay lifetime.[116] Second-order coherence $g^{(2)}$ measurements showed that even after weak coupling interactions with SLRs, the single-photon emission still preserved its quantum profile (**Figure 1.11c**). Promisingly, this work demonstrated that large-area NP arrays provide a versatile platform for coupling to single-photon emitters without need for precise control over their location.

1.6. Conclusions and Prospects

Metal NP arrays are an exciting platform for a range of fundamental studies and technological applications. The primary characteristics of SLRs combine the desirable properties of plasmonics and photonics: high localized EM field enhancements and high-quality resonances. With advances in fabrication tools, the scalable production of NP arrays has enabled integration with a wide range

of emitters, from organic dyes to semiconducting quantum dots to 2D electronic materials, and in both weak and strong coupling regimes. This simple system offers rich properties, and the future is bright for open challenges that require a diverse materials and scientific community to solve.

First, understanding and determining the cavity mode volume, a classical concept in optics, of SLRs is non-trivial because of the debate regarding the reliability of using absorptive materials as cavities. Conventionally, the Purcell factor *F* is defined by the ratio between quality factor *Q* and mode volume *V* and is used to quantify the enhancement of transition rate in emitters.[117] Although *Q* can be extracted from the linear optical properties, *V* cannot easily apply to plasmonic cavities because of their divergent field profile.[86,118] The "open cavity" architecture of the NP arrays further complicates this problem. Modeling that assesses *F* would be helpful for a complete picture of the plasmonic effect on emitters,[119,120] and experimental methods that determine internal losses would also be beneficial.[121]

Second, because of the accessibility of the NP array platform, more emitters are being coupled to SLRs, and theory that include active and functional materials need to be developed. Although the coupled oscillator model can quantitatively analyze the anti-crossing behavior in the dispersion diagram and calculate coupling between SLR with absorption and emission bands of emitters,[62,109] this model is merely functioning as a data processing tool to extract the coupling strengths. More fundamental approaches describing the electronic structure of quantum emitters and hybridization with SLRs can provide better a physical picture. For example, modeling excitons with electronic band structure and considering the exciton-exciton energy transfer and dephasing at high emitter concentrations will provide more detailed understanding of plasmon-exciton coupling. Also, the amplified spontaneous emission observed in lattice plasmon lasers cannot currently be described

fully because the excitation and emission are off-normal and the propagating mode is dispersive. Recently, the Liouville-von Neumann equations were used to describe plasmon-dye coupling for systems involving 1D slit arrays and showed the expected Rabi splitting.[107] This new method could inspire the next experiments to test the coherence of the emitters in plasmonic cavities.

Finally, open questions and emerging applications of plasmonic NP arrays include strong light-matter coupling and condensation of exciton-polaritons to form macroscopic quantum states. For example, the role of different lattice modes and materials in exciton transport and condensation phenomena is still unclear. Also, although the decay of condensed exciton-polaritons can show coherent emission like stimulated emission in conventional lasers, their origin from the stimulated scattering of bosons is different. NP arrays offer exciting platforms to study condensates because their open cavity structure allows direct access to spatial and temporal evolution of condensation. [1]

Referenced work:
W. Wang, M. Ramezani, A.I. Väkeväinen, P. Törmä, J.G. Rivas, and T.W. Odom, *Mater. Today* **ASAP**. "The rich photonic world of plasmonic nanoparticle arrays"
D. Wang, W. Wang, M.P. Knudson, G.C. Schatz, and T.W. Odom, *Chem. Rev.* **ASAP.** "Structural Engineering in Plasmon Nanolasers"

CHAPTER II. ULTRAFAST DYNAMICS OF LATTICE PLASMON LASERS

2.1. Introduction

Coherent photon sources on the nanometer scale are driving applications in on-chip optical communication, data processing, advanced medical imaging, and sensing.[122-124] Laser cavity designs that have enabled miniaturization include vertically stacked Bragg mirrors,[125] micro disks,[126] photonic crystals,[127-129] and nanowire structures,[130] where the lasing mechanism is based on conventional diffraction-limited Fabry-Pérot modes.[124] Taking advantages of intense nanoscale nearfield, surface plasmon-based lasers can overcome the diffraction limit and enable ultrafast operation on sub-picosecond regime.[131] Nanowire plasmonic lasers were one of the first designs based on a hybrid waveguide-surface plasmon polariton mode, but still relies on a Fabry-Pérot structure defined by the two end facets of the nanowire.[71,132] Before coherent stimulated emission fully built up, amplified spontaneous emission (ASE), a single-pass amplification[84] with less coherence, was observed in nanowire plasmonic lasers as a transitional stage.[83,133] Originated from the same hybrid waveguide mode for lasing,[84] ASE occurred at the same wavelength. Pump-probe measurements revealed the nanowire plasmonic lasers have pulse shorter than 800 fs,[85] but the ultrafast characteristics of lasing build-up was not demonstrated.

A complementary platform for plasmon-based lasing relies on nanoparticle (NP) arrays coupled to organic dye molecules as gain.[124,134] Lattice plasmons or surface lattice resonances (SLRs) are hybrid modes from coupling of localized surface plasmons on individual NPs to diffraction modes in a periodic array.[134] Besides strong near-field enhancement, the array structure can suppress radiative loss and provide optical feedback for directional lasing emission at room temperature.[21,26,28,34,53,135] Transient absorption[53] showed the shortening of excited states lifetime in dyes, which indicates the capability of increasing modulation speed of a laser. Time-correlated

single-photon counting measurements[34] of lattice plasmon lasing demonstrated nearly two-order of magnitude reduction in decay lifetime (~10 ps) due to fast stimulated emission. Ultrafast characteristics of plasmon-assisted emission process such as how photons trapped inside cavity, oscillate, and then emit are still missing, which is critical to understand the dynamics of the coupling between excitons and plasmons. The NP arrays with a dispersive photonic band structure enable other energy output channels such as ASEs co-exist with lasing at high pump powers.[34,53] ASE in NP arrays occurs at off-normal angles with different wavelengths. In this unique platform, we can study the lasing and ASEs simultaneously and clarify the light-emitting mechanism.

In this Chapter, we demonstrate the ultrafast time-resolved lasing action and ASE in lattice plasmon lasers and reveal the dynamics of exciton-plasmon coupling. We first show that the lattice plasmon cavity exhibits a surprisingly long cold cavity lifetime of picosecond scale and suggests that long-range lattice scattering is beneficial for building up stimulated emissions. With dye molecules as gain, plasmon lasing action holds an intrinsic threshold time, which reflects the population depletion in gain and energy transfer from excitons to lattice plasmon. Side-by-side dynamics and spectral properties of ASEs and lasing shows that the dispersive properties of periodic laser cavities will lead to light out-put channels with tunable angle and wavelength dependence. Finally, time-domain simulations provided insights that the relative exciton-plasmon location will influence the coherence in emitted light.

2.2. Photon Lifetime of Plasmonic NP Array

We used cold cavity lifetime measurements to evaluate the intrinsic loss of lattice plasmons by capturing photon dynamics inside the cavity (**Figure 2.1a**). Briefly, a femtosecond (fs) pulsed laser sent photons into the cavity, and scattered photons are collected by a streak camera providing time resolved emission map. We carefully aligned the surface of the sample normal to the detector to investigate the lattice plasmon mode serving as lasing mode first. The mirror M3 (Figure 1a) was

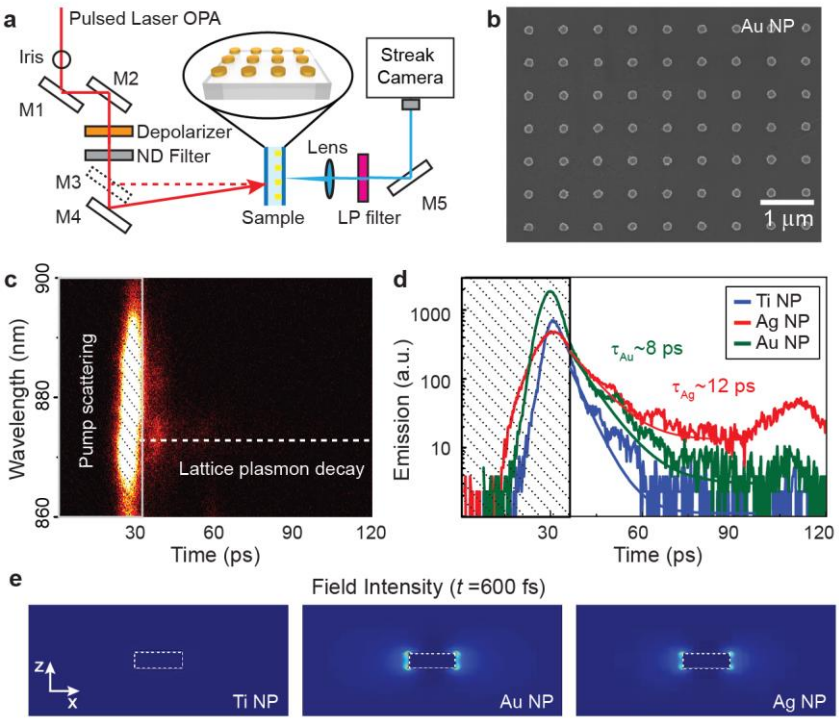

Figure 2.1 Scheme of photon lifetime measurements and photon lifetime of lattice plasmon (a)Scheme of cold cavity lifetime measurements. Samples are pumped at 870 nm by a Ti: Sapphire amplifier (35-fs pulse width, 2-kHz rep rate, 800 nm) tunable with an optical parametric amplifier and emission from the cavity was collected by a streak camera (400-nm spectral window, 110-ps temporal window) (b) SEM image of nanoparticle arrays on quartz substrate. p = 600 nm, h = 50 nm, d = 120 nm, substrate: fused silica, refractive index matched solvent: DMSO, n = 1.45) (c)Time mapping of photon emission of Au 2D arrays. (d) Histogram of photon counts at lattice mode (Au NP, Ag NP and Ti NP). The shaded area is scattering of photons from laser pump source, which will not be included in fitting. (e)FDTD simulations of nearfield at 600 fs.

aligned with the detector horizontally, and the light spot reflected by M3 was used as reference to adjust the sample angle to the detector. The angle of the pump laser was set at 5° off surface normal to avoid collection of the incident laser light.

A 2D AuNP array (**Figure 2.1b**) exhibited a narrow and strong band-edge SLR (λ=865 nm, Q=107) , and demonstrated lasing actions (**Figure 2.2**), was pumped by a femtosecond laser close to the resonance wavelength range (λ_{pump}=870 nm). While most of the photons scattered out of the cavity immediately (**Figure 2.1c**), some photons were trapped inside the lattice plasmon cavity and leak through the cavity at a later timing (following white dashed line in **Figure 2.1c**). The photon lifetime was obtained by fitting the photon histogram with a single exponential decay function. The photon lifetime τ of AuNP was 8 ps (Green line in **Figure 2.1d**). To eliminate the possibility that the photon signals came from photoluminescence of gold, Ag NP arrays were also tested and exhibit a photon lifetime of 12 ps (Red line in Figure 2.1d). As the control group for the lattice plasmonic effect, TiNP arrays and randomly distributed Au nanorods with similar plasmonic resonance were measured with the same set-up. The photon lifetime of TiNP (Blue line

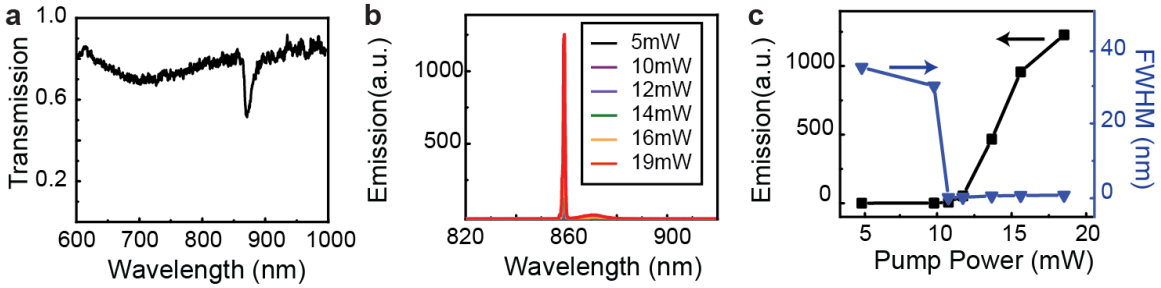

Figure 2.2 Surface lattice resonance and lasing action in 2D AuNP array (a) Transmission spectra of lattice plasmon mode sample λ=865 nm (*p*=600 nm, *h* =50 nm, *d*=120 nm, substrate: quartz, refractive index match solvent: DMSO) (b) lasing signals at sample λ=860 nm at various pump powers. (c) light-light curve and FWHM change with pump power indicating the feature of lasing action.

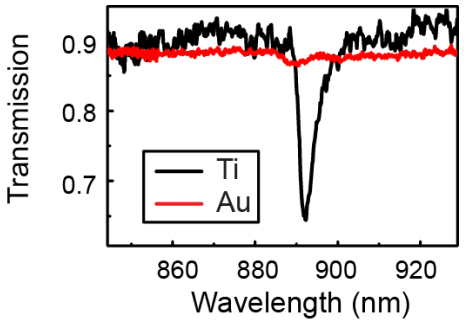

Figure 2.3 Linear properties of TiNP and AuNP arrays TiNP arrays are used as control sample for less-plasmonic material. The transmission spectrum of Ti NP arrays (red line) only showed a weak photonic diffraction resonance.

in **Figure 2.1d**) was not resolvable at best temporal resolution of the streak camera, which strongly indicates that the picosecond scale lifetime is unique to plasmonic NP arrays given that TiNP's do not support SLR (**Figure 2.3**). FDTD simulations showed that the electric field still was oscillating on the plasmonic NPs, while faded immediately after the planewave source coming through (**Figure 2e**). Au nanorods in aqueous solution and dispersed on a quartz substrate also have a non-resolvable photon lifetime, which emphasizes that the periodic arrangement of plasmonic NP is critical to a long-lived photon lifetime (**Figure 2.4**). The lifetime of localized surface plasmon (LSP) in small NPs is typically on the order of 10 fs.[136] The unexpectedly long-lived polaritons inside a cavity made of plasmonic NP arrays suggests that surface lattice resonance can slow the light inside the cavity, which is beneficial for providing good optical feedback inducing strong light-matter interaction such as lasing. The 10-ps scale lifetime also does not match with the estimated value calculated by Q-factor (100~200) and working frequency (~300 THz), which is shorter than 1 ps ($\tau = Q/f$). The unexpectedly long-lived polaritons inside a cavity from plasmonic NP arrays suggests that lattice plasmons can slow down the photons inside the cavity which is beneficial for building up optical feedback.

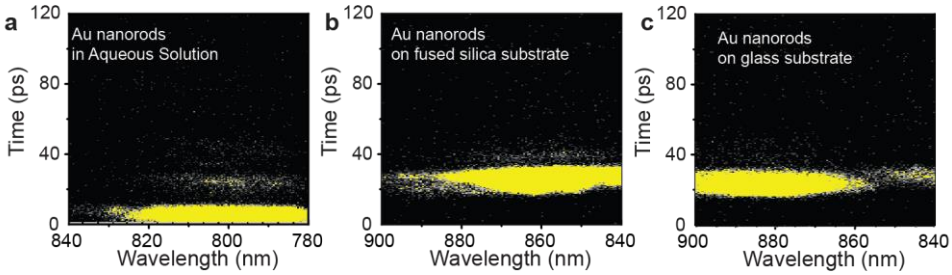

Figure 2.4 Photon lifetime of Au nanorods Photon emission map of Au nanorods (a) in aqueous solution, (b) dispersed on fused silica substrate and (c) cover glass substrate. Only strong scattering from the pump observed on the map. No resolvable photo lifetime.

Photons that are scattered in the surface-normal direction have a long lifetime because they are evolve from a band-edge surface lattice resonance, where infinite arrays of NPs oscillate in-phase. Despite the absence of reflecting mirrors as in a Fabry-Perot cavity, this phase-locked oscillation feature of the band-edge lattice mode will trap the photons inside the "cavity" for a longer time before escaping the cavity. Since the intensity of a long-lived photon is relatively low compared to that of a photon directly scattering outside the cavity, they cannot be observed in transmission spectra. Photon lifetime measurements can separate the slowly decaying photons from the fast

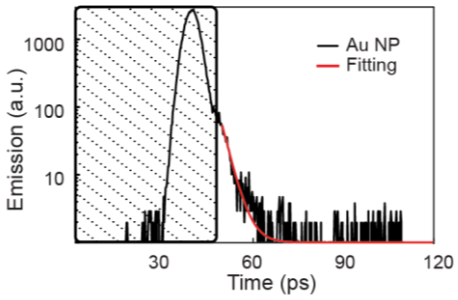

Figure 2.5 Photon lifetime of AuNP with smaller excitation spot size We focused the incident laser beam into a smaller spot (*d*=1 mm). The photon lifetime of AuNP was shortened to 3 ps.

decaying ones by temporal deviation. The long-lived photons appear to be undergoing long time confinement within the lattice, which leads to the picosecond scale photon lifetime. Considering the distance a photon can explore in an array of NPs during the picosecond lifetime ($L = (c/n)*\tau$), the long range scattering process would explore a millimeter scale of NP arrays. When excited by smaller pump spot size, the effective area of photon exploration became smaller, thus there is a shorter photon lifetime. After shrinking excitation spot size from d = 4 mm to d = 1 mm, the average photon lifetime from the samples decreased from 8ps to 3 ps (**Figure 2.5**).

2.3. Lasing Action in A Plasmonic NP Array

In the photon lifetime measurements, a femtosecond laser was used as the photon source for the lattice plasmon cavities. In lasing measurements, dye molecules dissolved in an organic solvent were used as the gain medium to pump lattice plasmons. IR-140 has emission cantered at 860 nm with a broad bandwidth of 80 nm, which spectrally overlaps with the SLR in AuNP arrays on glass. Lasing emission was achieved at 885 nm with a threshold energy of 0.15 mJ/cm^2 (**Figures 2.6a-b**). The time-resolved photoluminescence (PL) measurements revealed unique ultrafast dynamics of lattice plasmon lasing. Below the lasing threshold, the spontaneous emission (SE) of dye

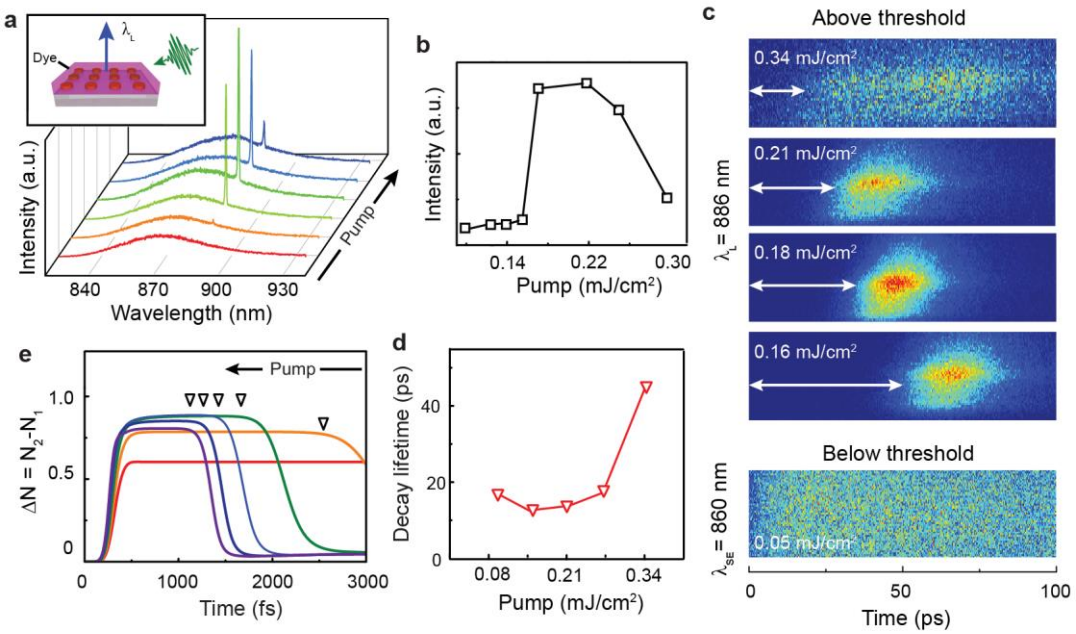

Figure 2.6 Pump power dependent study of dynamics of lasing action in lattice plasmon (**a**)Scheme of lasing signal emitting from the surface normal of the Au NP array with IR-140 (Au NP arrays: p = 600 nm, h = 50 nm, d = 120 nm, substrate: glass, refractive index n = 1.5). Lasing spectra at increasing pump power. (**b**)Light-light curve of lasing signal. (**c**) Time-resolved emission maps of spontaneous emission from IR140 and lasing signals after increasing pump intensity above threshold. (**d**) Lasing decay lifetime above threshold pump power. (**e**) Population inversion time evolution at various pump powers.

molecules has been collected by streak camera at time zero. (**Figure 2.6c**, lower panel**)** Above the lasing threshold, lattice plasmon lasing had an intrinsic rising time and the rising time decreased from 50 ps to 25 ps with increasing pump intensity (Figure 2.6c). We also compared the decay lifetime of lasing emission and SE of dye molecules. **Figure 2.6d** shows that below the lasing threshold (0.05 mJ/cm^2), only the SE of IR-140 dye molecules contributed to the emission signal, which had a decay lifetime of 780 ps, close to the intrinsic lifetime of IR-140 (800 ps). Above the lasing threshold (0.15-0.26 mJ/cm^2), decay of the emission decreased by an order of magnitude (to 10s of ps), indicating strong interactions between dye molecules and the NPs. At high pump power (>0.22 mJ/cm^2), the lasing intensity decreased. One possible explanation for this decrease was the degradation of dye molecules, but this assumption was eliminated by the fact that the lasing intensity increased back again when the pump power was lowered. At extremely high pump power (0.30 mJ/cm^2), not only did the lasing intensity drop dramatically, the lasing decay lifetime also increased to 43 ps, which implies deterioration of lasing action. We address this point in the next section.

To understand the dynamics of plasmonic lasing, we combined the finite-difference time-domain (FDTD) method with a four-level gain model to track the time evolution of population inversion at various pump intensities. Simulations showed that upon a pulsed pump, the population inversion ($\Delta N=N_2-N_1$) started building up and then depletion was triggered, which indicated that the population inversion was reduced to the point where stimulated emission could not overcome losses needed for lasing. At higher pump intensity, the depletion showed up earlier (**Figure 2.6e**). The rising time is a unique feature of plasmonic lasing, which reflects the process of energy transfer from the gain medium to the lattice plasmon. Note that simulations have a sub-picosecond

time scale which is shorter than experimental results, because energy transfer leading to stimulated emission has extremely high efficiency in the model, and cavity loss mechanisms are much less important.

2.4. Competing Between Lasing and Amplified Spontaneous Emission (ASE)

At high pump power, the deterioration of lasing is attributed to the other competing light emission channel - amplified spontaneous emission (ASE)- in the lattice plasmon structure. The lattice plasmon cavity is a unique platform where we can observe ASE and lasing simultaneously and study their competing energy transfer pathways. If the lattice plasmon resonance (dark dispersion line) overlaps with emission by dye molecules (red shaded area), lattice plasmon modified emission can be observed over a wide range of angles (marked with coloured squares)

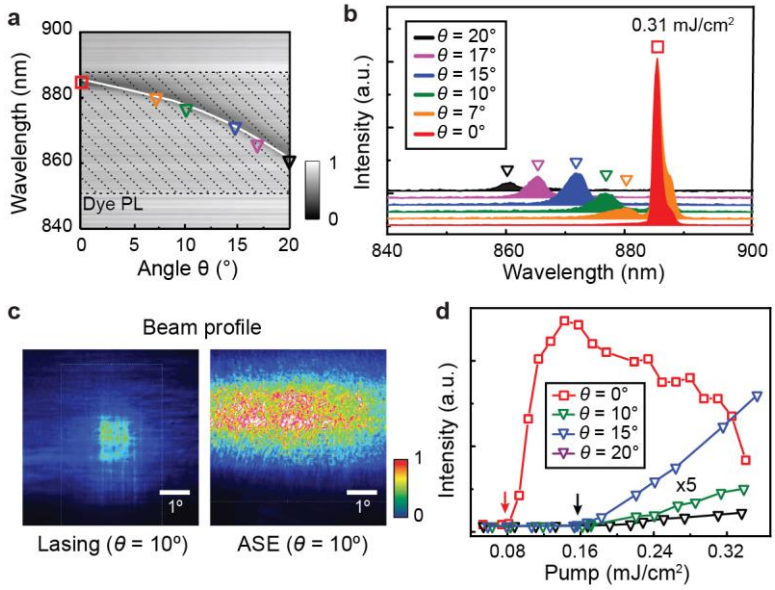

Figure 2.7 Spectral properties of lattice plasmon lasing action and amplified spontaneous emissions (a) Lattice plasmon dispersion diagram. Red boxed region is the emission band of IR140. (b) Emissions follows the dispersion diagram lattice plasmon. (c) Far field beam profile of lasing action and ASE. (d)light-light curve of the emissions of lasing action and ASE.

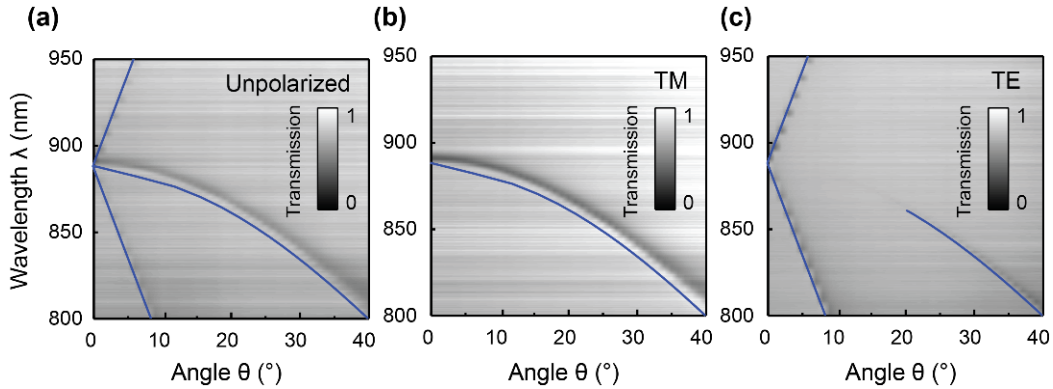

Figure 2.8 Liner dispersion diagrams of SLR under different indent polarization (a) Unpolarized light. (b) TM polarized. (c) TE polarized. Note that at high angle, TE polarized light can also excited the TM polarized lattice plasmon mode by the component of E field along the surface. TE branch of the SLR contributed to the redder shoulder of ASE emission spectra.

and wavelengths at high pump power (**Figures 2.7a-b**). To study this, emission was measured at multiple detection angles θ. ASE signals were observed at various $\theta > 0^{o}$, and they have broader bandwidth (3¬4 nm) than for lasing ($\theta = 0^{o}$, <1.5 nm). We also found that emission from the TE polarized lattice plasmon at small angle contributed to broadening of the orange curve to redder wavelengths, as the TE polarized lattice plasmon follows a more dispersive mode that shifts to longer wavelength (**Figure 2.8**). The far-field beam profile also showed that ASE has a larger beam divergence than the lasing signal (**Figure 2.7c**). Here the ASE (θ=10 º, 15 º, 20 º) and lasing ($\theta = 0^{o}$) light-light signals were collected side by side. As pump intensity was increased, the lasing signal dominated emission above threshold (~0.06 mJ cm^{-2}) and then dropped at around 0.15 mJ cm^{-2}, corresponding to where the ASE signal emerged and then eventually suppressed the lasing signal intensity at higher pump intensities. (**Figure 2.7d)**. For $\theta > 0$ º, the individual NP polarizations no longer oscillate in phase, in contrast to what happens for the band-edge modes ($\theta = 0^{o}$) where a well-defined wave front is formed in the plane of the array (**Figure 2.9**). Hence, the SLR at ($\theta > 0^{o}$) propagating modes, provide less optical feedback and a lower LDOS, and therefore

became a secondary choice for the gain medium to dump energy into when the system was overwhelmed with pump fluence. That the ASE signal has a higher threshold than the lasing signal is also attributed to the fact that nearfield enhancement of the propagating mode is weaker than

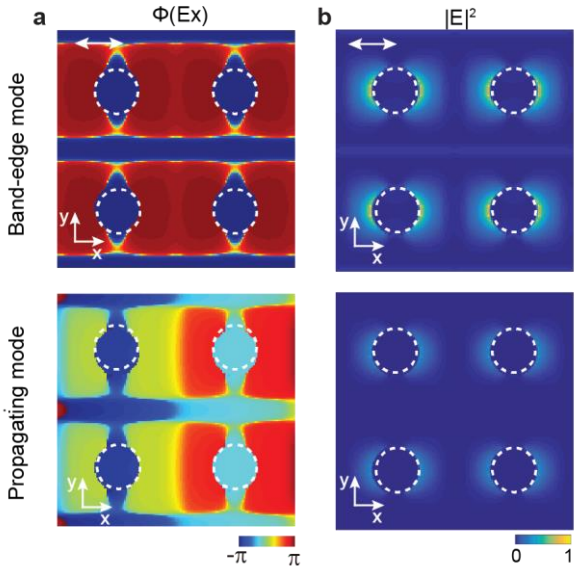

Figure 2.9 FDTD simulation of Au NP (a)Phase information of band-edge and propagating mode. Propagating mode has a well-defined wave front propagating through lattice. At band-edge mode all the NP oscillate in phase. (b) Electric field nearby NP at resonance. Band-edge mode has stronger nearfield enhancement than propagating mode.

that of the band-edge mode (Figure 2.9**).**

2.5. Dynamics of Lasing and Amplified Spontaneous Emission (ASE)

Figures 2.10a-b show that with IR-140 added, and at high pump power (0.15 mJ/cm^2), the ASE (θ = 10 º) decay lifetime (7 ps) became shorter than that of the lasing signal (θ = 0º, 16 ps), which is consistent with cold cavity lifetime results, photons takes different time to scatter out of the cavities. ASE with shorter decay lifetime also could be a preferable and competing energy output channel with lasing. At extremely high pump power (0.3 mJ/cm^2), the decay lifetime of lasing emission increased to 46 ps (Figure 2f) while ASE had a still shorter decay lifetime. This shows how competition from ASE deteriorates the lasing action. **Figures 2.10c-d** show that the

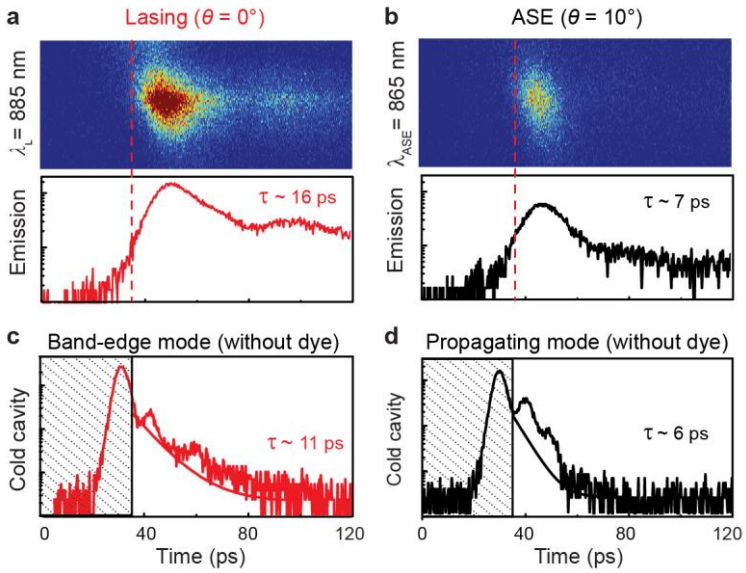

Figure 2.10 Lifetime study of lattice plasmon-enhanced emissions Time resolved (a) lasing emission and (b) ASE (θ=10 º). Cold cavity lifetime of (c) band-edge mode (θ=0 º) (d) propagating mode (θ=10 º). Shaded area is photon scattering from fs laser source.

cold cavity lifetime of the propagating mode (θ = 10 º) in the absence of dye molecules was only 6 ps, shorter than that of the band-edge mode (θ = 0º), which indicates that the propagating mode is more dissipative. This suggests that the photon pathway varies for different lattice plasmons. Photons that are scattered in the surface-normal direction have a long lifetime because they are evolve from a band-edge mode, where the charges of NPs in infinite arrays oscillate in-phase. In contrast, photons scattered at off normal angle with shorter lifetime, due to incomplete phase lock of the propagating mode. A good quality, low-loss band-edge mode leads to lasing action, while a lower quality, high-loss propagating mode will lead to ASE.

The 4-level model showed that with the appropriate laser pump intensity, depletion of population inversion inducing ASE (θ=10 º) started earlier than the lasing action (**Figure 2.11a**). Also, as shown in the experimental results, the intensity of ASE is weaker than lasing action, when pump intensity is slightly higher than ASE threshold (**Figure 2.11b**). By tracking the out-of-plane

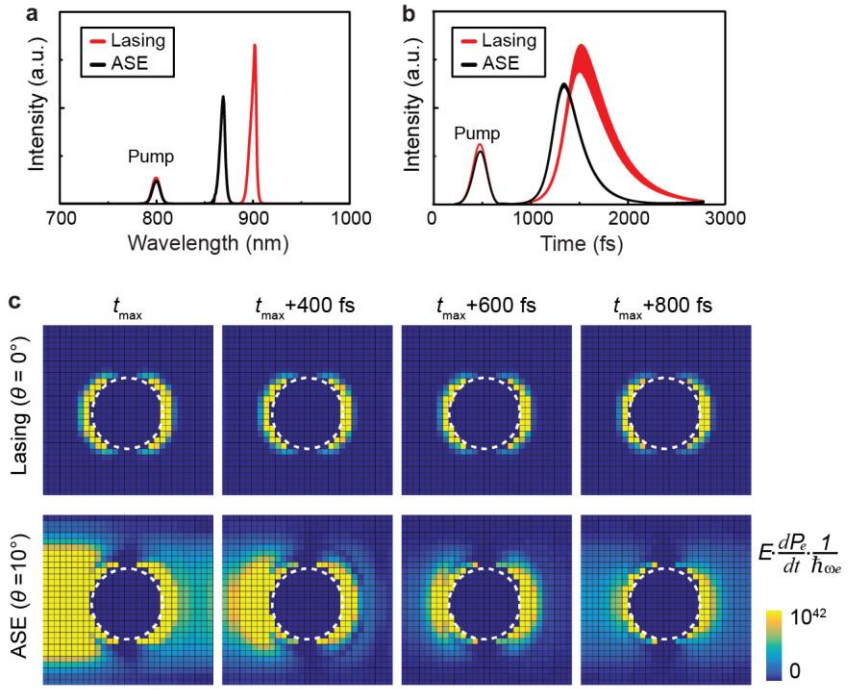

Figure 2.11 FDTD simulation of lattice plasmon-enhanced emissions. (a) Simulated lasing and ASE spectra under same pump intensity at 800nm. ASE shows lower intensity compared to lasing signal. (b)Time evolution of lasing and ASE field intensity with normal excitation (θ = 0º) and off-normal excitation (θ = 10º), correspondingly (c) Time evolution of out-of-plane stimulated emission from ASE and lasing.

stimulated emission, the only contribution to the lasing action from the gain medium is within 20-nm of the NP, which corresponds to the hotspot region for surface lattice resonances (Figure 2.9). ASE has contributions from both the hotspot region also the gain medium distant from the NP. A snapshot of the time evolution of the local field intensity shows that the stimulated emission pattern propagates from the one side of the NP to the other (**Figure 2.11c**). The spatial migration of the stimulated emission process indicates that ASE is an enhanced emission process with a single optical pathway. Due to this bulk contribution from gain, the ASE has less coherence than lasing signals.

2.6. Conclusions

In conclusion, the relatively long cold cavity lifetime of lattice plasmon indicated that the photons undergo long-range scattering inside the plasmonic NP array cavities. Long range lattice scattering can help the gain compensate the loss in a plasmonic structure and enhance the coupling between excitons and plasmons. Also, we found that plasmonic lasing and ASE have an tens of picosecond intrinsic rising lifetime related to the timing of population inversion depletion and energy transfer from gain to plasmons. Using this unique AuNP array lattice plasmon system, we established a stable platform to distinguish and characterize plasmonic ASE and lasing. ASE can co-exist with lasing when the system, which lead to potential applications require wavelength and angle tunable stimulated emission. Understanding the factors that affect the coupling of excitons to plasmons will help better design lattice plasmon devices for strong light-matter interactions.

CHAPTER III. DUAL-MODE PLASMON LASING FROM SPATIALLY DISTINCT HOTSPOTS

3.1 Introduction

Plasmonic nanostructures can confine light into sub-wavelength region and formed hotspots with high electric field intensity in their vicinity. To achieve effective nanoscale light-matter interaction, placing a photoactive medium into the hotspots region is critical. Current approaches such as self-assembly of DNA molecules can integrate an active medium onto the surface of plasmonic structures, but cannot specifically locate them at the hotspot region.[137] More selectively, plasmon-triggered nano-photopolymerization can trap dye molecules at the hotspots,[138] but the dipole orientation in the molecules will also be fixed after polymerization. Similarly, polymerization can also locate two color quantum dots at the hotspot for enhancement PL, while the system only utilized one plasmonic resonance.[139] To investigate energy transfer between active media with plasmonic structures, we designed a more complex system in which the excitons inside gain medium has with controllable dipole orientation and are free to choose between two spatially and spectrally distinguishable energy transfer pathways that lead to lasing actions. This design allows us to to investigate exciton-plasmon coupling under the influence of two SLRs with spatially distinct nano-optical field enhancement on a single NP in the lattice.

Taking advantages of lattice geometry and unit cell design, SLR has both metric as plasmonic system with strong nearfield enhancement and long range diffractive coupling as in photonic system.[134] SLR offers an additional way of controlling nanoscale optical field confinement by taking advantage of long range diffractive coupling in the lattice geometry. Varying the unit cell design, *in-plane*, *out-of-plane*, and higher order SLR can change the hotspots localization on individual NP in arrays. By changing the lattice geometry, SLR can also achieve widely tunable wavelengths.

Surface lattice plasmons offer a promising platform for sustaining multiple SLRs with capability of plasmon-exciton coupling and leading to various applications. Exciton-plasmon coupling results in plasmonic lasing in far field, which can be used as a tool to investigate the factors affecting exciton-plasmon interaction. With gain medium such as organic dye molecules added into system, band structure engineered NP arrays have demonstrated multicolor lasing action with controllable wavelengths. In that system, each lasing mode hotspot is not totally spatially separated and the lasing dynamics cannot be individually tuned.[135]

In this Chapter, we show that dual mode lattice plasmons provide a platform to realize controllable dual lasing devices with polarization dependence. Taking advantages of diffractive coupling of LSP, two types of spatially, spectrally distinct SLRs co-exist in the same platform and preserve high quality plasmonic resonances. Dual-mode lasing is achieved due to selectively induced exciton-plasmon coupling by varying polarization of incident pump. Rising timing and decay dynamics of each lasing mode could be tuned by varying pump polarization. Simulations showed how population inversion evolved spatially. Last, dual mode lasing did not have mode competition, which can prove useful in applications.

3.2. Dual-Mode SLR in A Rectangular Lattice

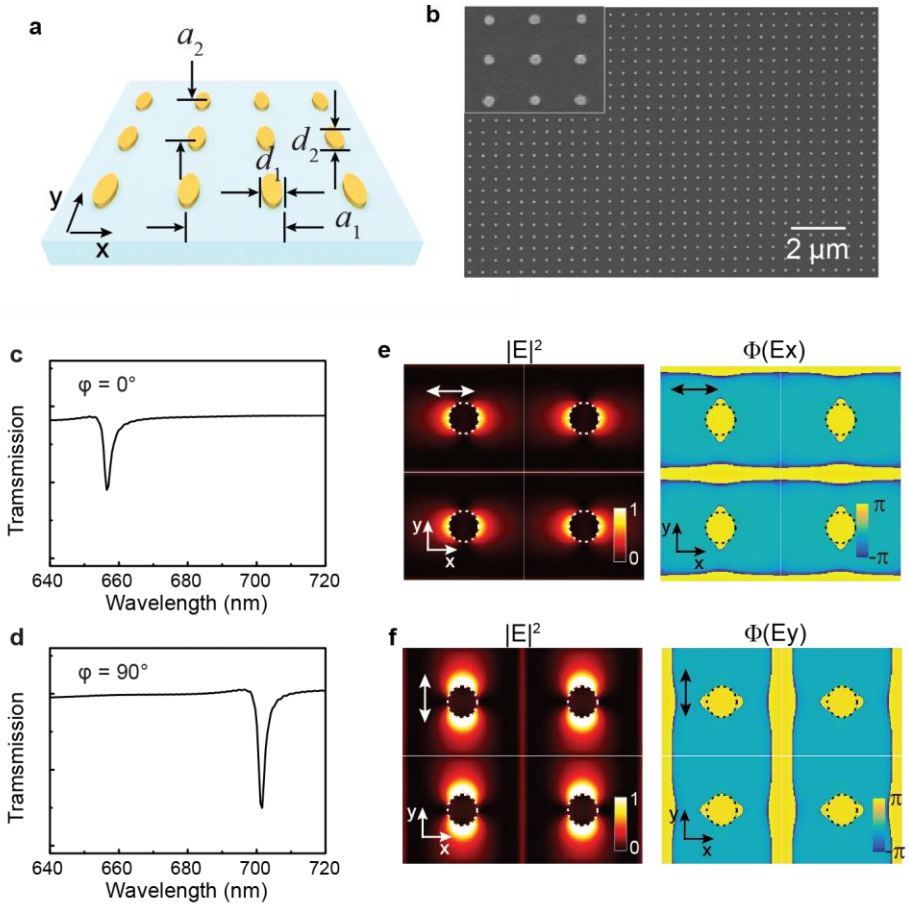

Figure 3.1 Linear optical properties of dual modal surface lattice resonance (a) Scheme of dual-mode SLR design. (b) Scanning electron microscope image of NP arrays on fused silica substrate (n=1.45). Transmission spectra of dual SLR under incident light aligned in (c) x direction, φ=0° and (d) y direction, φ=90°. Nearfield enhancement and phase information of (e) λ_1 mode and (f) λ_2 mode.

We used two-step exposure of line PDMS mask during phase shifting photolithography and fabricated elliptically shaped NP (d_1 = 80 nm, d_2 =100 nm) in a rectangular lattice. (a_1=480nm, a_2= 450 nm) (**Figures 3.1a-b**). To achieve high quality of both SLR, we optimized the combination of lattice periodicity and NP axis length. For a fixed periodicity, smaller NP offered higher mode

quality. Since LSP in individual unit diffractive coupled to (0, ±1) modes in lattice, the NP axis length should be shorter in the direction of longer lattice periodicity, and vice versa. Under different in-plane polarization, band-edge SLR showed up at the corresponding wavelength determined by the periodicity of the 1D NP chains and the refractive index of the surrounding environment (n=1.45) (**Figures 3.1c-d**). When in-plane polarization is aligned with short axis of NP (x direction), a dipole momentum was excited on the individual NP with x orientation. Nearfield enhancement showed a typical dipolar field pattern in x direction (**Figure 3.1e**). In the phase map, the x-orientated dipole on the individual NP diffractively coupled to the neighboring NP in y direction. The in-phase oscillation of NPs provided optical feedback for lasing action.

3.3. Switchable Dual-Lasing Action Via Changing In-Plane Polarization of Pump

By using a dichroic filter, we can pump the system with normal incident light and collect lasing from surface normal (**Figures 3.2a-b**). This set-up guaranteed that the incident light was

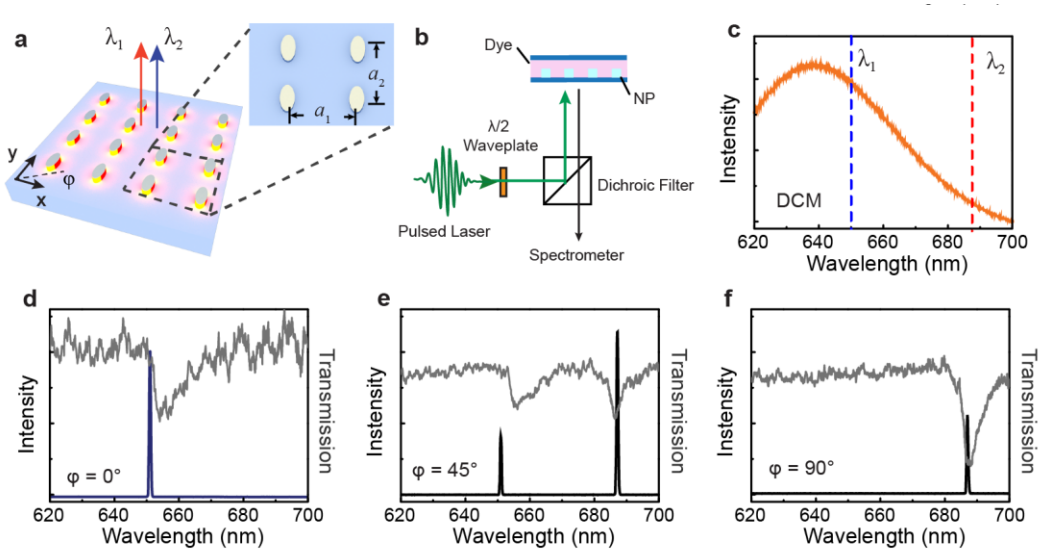

Figure 3.2 Spectral switching of dual mode lasing by in-plane polarization (a-b) Scheme of dual-mode SLR lasing experiment design. (c) DCM dye emission under fs pump. Transmission spectra of dual SLR and lasing emission under incident light aligned in (d) x direction φ=0°, (e) φ=45°, and (f) y direction, φ=90°.

linearly polarized when exciting the dye molecules. Polarization of pump determined most of the dipole orientations in the dye molecules. Specifically, we used DCM laser dye molecules dissolved in DMSO (c = 4mM) and pumped them with 400-nm femtosecond pulsed laser. DCM has the main emission centered at 640 nm and the broad bandwidth of the spontaneous emission covered dual-SLR modes (**Figure 3.2c**). Upon excitation, the population inversion built up and held the energy

as excitons inside dye molecules. Above threshold, excitons started to transfer the energy to the most accessible SLR mode for lasing.

Lasing action can be switched between dual SLR modes by varying in-plane pump polarization (φ). When most exciton orientations are aligned with the short axis of NP (φ=0°) (**Figure 3.2d**), only λ_1 lasing mode showed up. At φ=45°, the exciton does not align with either SLRs, and the dipole orientation is more randomly distributed. Both lasing modes were enabled (**Figure 3.2e**). Similarly, when most of them are aligned with the long axis of NP, λ_2 mode lasing

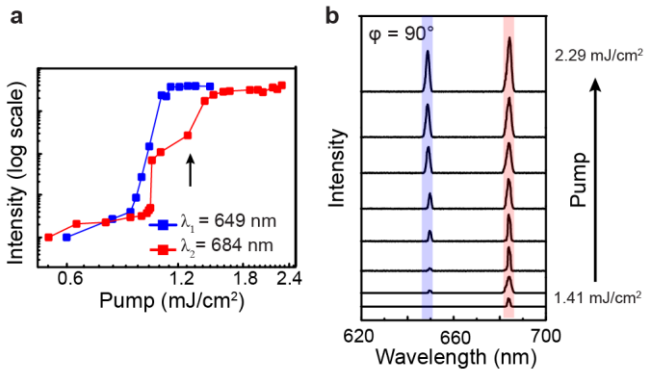

Figure 3.3 Light-light curve of dual-mode lasing under linearly polarized pump (a) Light-light curve of dual-mode lasing. (b) Under higher pump power, both modes lased under φ=90°.

emerged (**Figure 3.2f**). Threshold behavior of both lasing modes was measured under φ=0° and 90° for λ_1 and λ_2 modes, respectively (**Figure 3.3a**). λ_1 mode has a slightly lower threshold than λ_2 mode, because the λ_1 mode has more spectra overlap with the main emission of dyes. With increasing pump power, signal intensity of both modes became stable and saturated. Note that after onset of λ_2 mode lasing, there is an inflection point on light-light curve around 1.4 mJ/cm^2. At this pump intensity, λ_1 lasing mode also emerged in the system, even if the pump was under φ =90° (**Figure 3.3b**), because excessive exciton energy was dumped into λ_1 mode lasing.

3.4. Dynamics of Dual-Mode Lasing

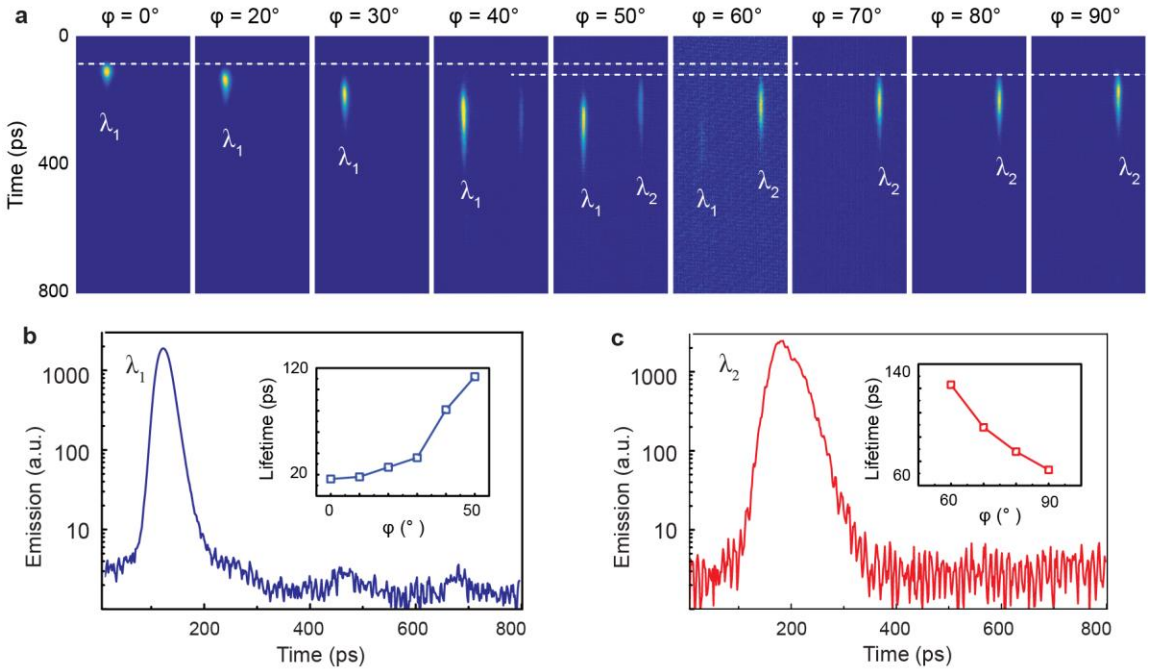

Figure 3.4 Tuning the dynamics by changing *in-plane* pump polarization (a)Time-resolved emission map of lasing signals. White dashed line marked the relative rising timing of two lasing modes. With detuning the polarization from the SLR, the lasing signal showed up later. (b) λ_1 emission decay lifetime. (c) λ_2 emission decay lifetime.

To understand the competition between two lasing modes, we measured time resolved emission by a streak camera. Pump intensity is fixed at a moderate value which is slightly above the dual mode lasing threshold. In-plane polarization (φ) is one key factor determining the rising time of lasing action (**Figure 3.3**). λ_1 mode lasing has earlier rising time, when the *in-plane* polarization is aligned with short axis of the NP. As the majority of dipole exciton orientation turned away from λ_1 SLR (φ increase to 90 °), λ_1 lasing has later rising timing. λ_2 mode signal showed a reversed trend, but the earliest rising timing of λ_2 mode is still later (delayed 17 ps) than

that of λ_1 mode. λ_2 mode lasing was the consequence of the coupling between SLR and excitons whose energy was at the tail of dye main emission. Thus, less spectral overlap compared to λ_1 mode lasing makes the rising threshold longer than that of λ_1 mode. During the measurement, the rising time gap between λ_2 and λ_1 modes has been tuned from more than 40 ps down to 15 ps, which indicates macroscale pump polarization can control the nanoscale ultrafast lasing emission timing.

Shortening of decay lifetime indicated the exciton-plasmon coupling and was affected by the *in-plane* polarization (**Figures 3.4b-c**). The intrinsic DCM spontaneous emission decay lifetime is 2.2 ns. [140] λ_1 mode has shortest decay lifetime of 18 ps, when pumped along the short axis of NP (Figure 2b). When turning the in-plane polarization away from the λ_1 SLR, the decay lifetime increased to 100 ps and eventually λ_1 mode did not lase (Figure 3.4b, insert). λ_2 mode emerged when the *in-plane* polarization shifted from λ_1 SLR hotspots. λ_2 mode has the shortest lifetime of 53 ps, which is relatively longer than that of the λ_1 (Figure 3.4b). Less spectral overlap between dye emission and λ_2 is attributed to slower energy transfer between exciton and SLR.

Finite-difference time-domain (FDTD) method with a four-level gain model was used to track the time evolution of population inversion at various in-plane polarization. The population inversion ($\Delta N=N_2-N_1$) started building up and then depletion was triggered. Depletion of population inversion is a signature of the beginning of plasmonic lasing. Simulation showed that

more population inversion built up when pump is in favor of the corresponding lasing mode, and depletion of population inversion also appeared earlier (**Figures 3.5a-b**).

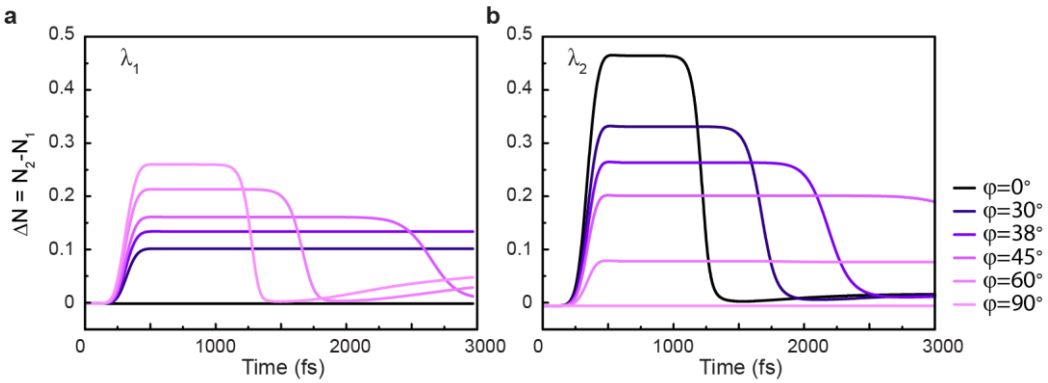

Figure 3.5 Population inversion time evolution under different pump polarization (a) λ_1 and (b) λ_2 modes

3.5. Evolution of Spatial Mapping of Dual-Mode Lasing

Simulation can reproduce two lasing signals by varying *in-plane* polarization of pump source (**Figure 3.6**). Consistent with experimental results, when changing the pump polarization, the depletion of population inversion showed up at a different timing. We specifically investigated the

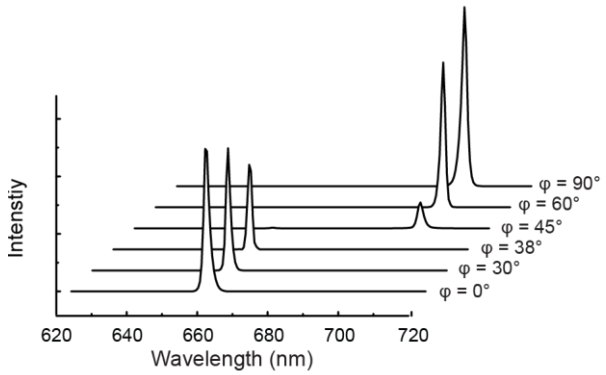

Figure 3.6 Modeling of dual-mode lasing

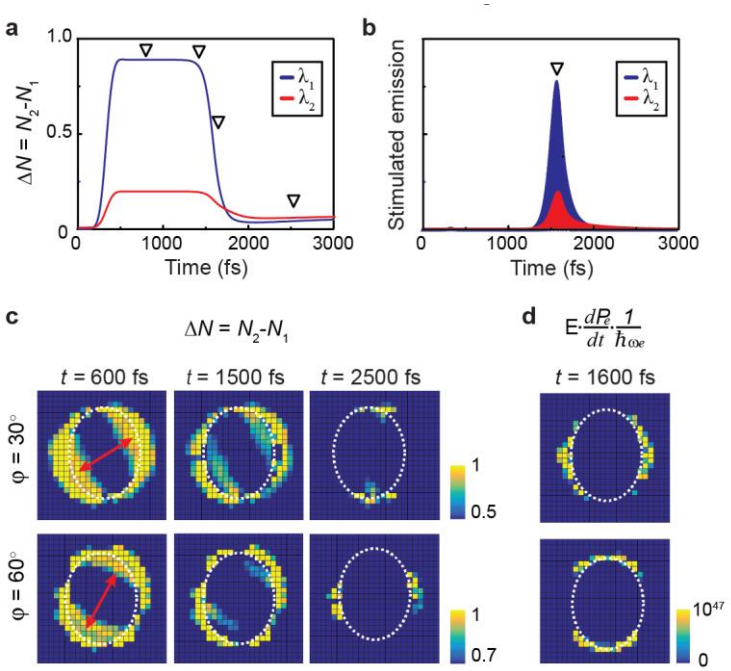

Figure 3.7 Four level-FDTD modeling of dual mode lasing (a)Time evolution of population inversion of dual mode lasing at hotspots. (b)Stimulated emission time evolution at hotspots for λ_1 and λ_2 mode. (c) Spatial map of population inversion at various timing. From left to right, population inversion building, population depletion started at hotspots, remaining population inversion at non-hotspots region. (d) Stimulated emission only shows up at hotspots of each lasing modes correspondingly.

condition when the population inversion was not perfectly aligned with either lasing mode at φ=30° and φ=60°. λ_1 and λ_2 mode lasing showed under 30° and 60°, respectively. Population inversion was monitored at hotspot of dual-mode SLR, and undergoes three stages marked by the triangles in **Figure 3.7a**. At first stage, upon the pump, population inversion has built up but the number of inversion has been holding for a while. Second stage is the lasing action (1500 fs-1800fs). **Figure 3.7b** shows the dual-mode lasing intensity evolution over the time, the peak intensity happens at 1600fs, which is after the population depletiong has been consumed for about half. Final stage, there was some residue population inversion still in the system that does not contribute to any of the stimulated emission. In spatial map of pupulation inversion (**Figure 3.7c**),

we can see that the initial population inversion distribution aligned with the pump polarization. (Figure 3.7c, left panel) Only the population inversion at the hotspots of the SLR was consumed for corresponding lasing (Figure 3.7c, middle panel). In end of simulation, some population inversion remains at λ_2 (λ_1) mode hotspot at 30° (60°) (Figure 3.7c right panel). Stimulated emission spatial map (**Figure 3.7d**) further confirmed that lasing comes from the corresponding hotspots of dual SLR. Upon excitation, population inversion built up in dyes near the NP, but only those locate at hotspots of SLR will contribute to lasing action.

3.6. Dual-Mode Lasing Without Mode Competition

By substituting the halfwave plate with a depolarizer, we pumped the dye molecules with a randomly distributed polarization. Depolarized pump is an affective ensemble of linearly polarized pump at all orientations. The excitons under this pump were not specifically set up with a preferred SLR to couple with. Enhanced PL was observed at both modes below the threshold (**Figure 3.8a**). Above threshold, two modes lased simultaneously. From light-light curve (**Figure 3.8b**), λ_2 lasing peak has a lower threshold than λ_1 lasing peak, but once the lasing action builds up, λ_1 peak had a higher intensity. The lasing signal intensity was determined by the spectra overlap

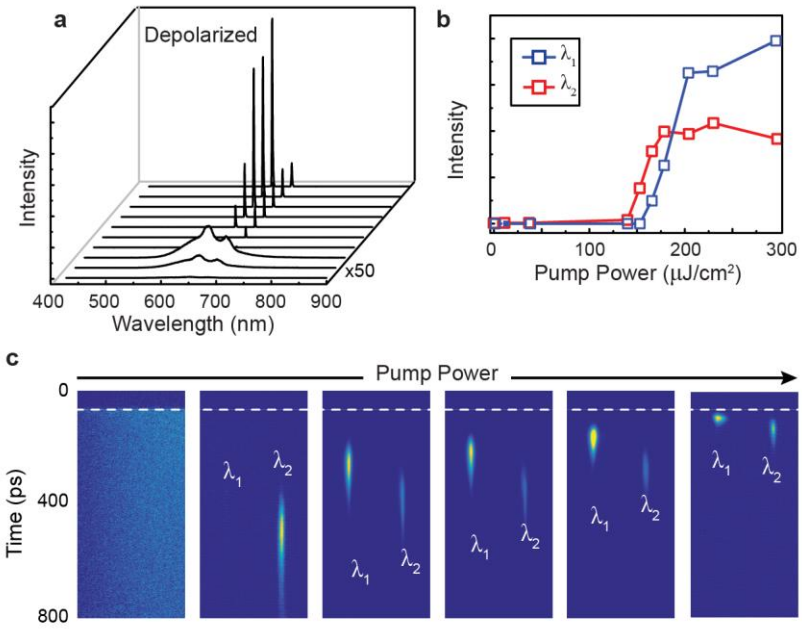

Figure 3.8 Dual lattice plasmon lasing action does not compete under depolarized pump (a) light-light curve of dual lasing (b) threshold behavior of two peaks. (c-e) dynamics of dual mode lasing below and above lasing threshold**.**

with main emission band of dyes. Also, stronger nearfield enhancement benefits lowering lasing threshold. As shown in Figure 3.1f, λ_2 mode has higher nearfield intensity than λ_1 mode does.

Time resolved emission of dual mode lasing peak revealed no competition (**Figure 3.8c**). Below threshold, only enhanced PL was observed, and the decay lifetime of emission were similar intrinsic decay lifetime of dye. (Figure 3.8c, left panel.) With increasing pump power, the rising timing get earlier, and decay lifetime also gets shorter. (Figure 3.8c, right panels) When pumped by non-polarized light, the excitons have random dipole orientations. Energy transfer between exciton to either mode can build up independently. High above threshold, two modes both reached the earliest rising time and shortest decay lifetime with λ_1 mode of 18 ps and λ_2 mode of 48 ps (**Figure 3.9**). Fast decay lifetime of both modes indicated dual mode lasing action was well-built

up. λ_1 mode has more spectral overlaps with main emission band of dye molecules, so the decay lifetime is shorter than λ_2 mode's.

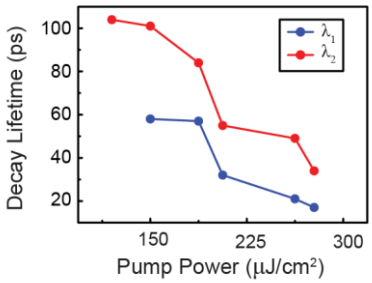

Figure 3.9 Decay lifetime of dual-mode lasing under depolarized pump with increasing pump power

3.7. Conclusions

In conclusion, dual-mode SLR was achieved by introducing an additional lattice periodicity, and the corresponding dual-mode lasing was demonstrated with spectral separation of up to 40 nm. Real time lasing tunability was enabled by controlling incident pump polarization. Study of lasing dynamics and FDTD simulations revealed the exciton energy transfer process to the dual-SLR. Rising time of lasing peak is affected by the initial pump polarization. Lasing signal comes from the exciton located at the hotspots of the SLR. We also demonstrated the capability of tuning the lasing timing at 10 ps scale without mode competitions, which could be useful for multiplexing signal processing. [2]

---

[2] Referenced Work: Weijia Wang, Ran Li, Yuanhai Lin, Jianxi Liu, Danqing Wang, Richard. D. Schaller, George C. Schatz and Teri W. Odom, "Dual-Mode Plasmon Lasing from Spatially Distinct Hot Spots", in preparation

CHAPTER IV. SPATIALLY DEFINED MOLECULAR EMITTERS COUPLED TO PLASMONIC NANOPARTICLES

4.1. Introduction

Although strong coupling between molecular excitons and lattice plasmon can be achieved, there are still challenges to be overcome. For example, localize the molecular excitons with nanometer scale control is critical for the nanophotonic application, because only the excitons near plasmonic NPs are effectively coupled. For most plasmon-based system, organic dyes are either dissolved in solution or embedded in a polymer layer matrix, in which a large number of dye molecules are not distributed within the plasmonic nearfield enhancement region. Moreover, high concentration of dye can result in aggregation-caused photoluminescence quenching.[141] Thus, spatial arrangement of solid-state molecular emitters without self-quenching on nanoscale plasmonics is crucial for effective coupling and efficient energy exchange.

Metal-organic frameworks (MOFs), consisting of organic ligands arranged between the metal-ion nodes, provide a robust and flexible platform for photon emitting and optical sensing.[142,143] The photoactive ligands of MOFs can serve as concentrated molecular emitters to overcome the limitation of organic dyes either in solution or in their solid state. Since the intermolecular distances in these frameworks are usually 1-2 nm and larger than the size of molecular crystals, MOFs do not suffer from aggregation-caused quenching.[141] Unlike *J*- and *H*-aggregates of dyes that exhibit strong transition dipole moments that couple to adjacent molecules,[144] the chromophores in MOFs have weak electronic coupling and do not show aggregation-induced quenching.[141] In addition, MOFs can be easily processed as thin films on different types of substrates and assembled on nanostructures following the surface topologies.[145] Therefore, with the optical properties derived from the properties of molecular building blocks, MOFs can serve as a novel class of molecular emitters in solid-state for coupling to plasmons.

In this Chapter, we show how spatially organizing chromophores via a MOF template around plasmonic NP arrays can produce plasmon-dominated hybridization. Luminescent Zn-porphyrin MOFs were conformally assembled on silver NPs (AgNPs), and hybrid exciton-SLR states were observed. Using femtosecond transient absorption (TA) spectroscopy, we observed that the hybridized modes appeared immediately (within 50 *f*s) after photon excitation and persisted over 1 ns time window. The hybridization led to mode splitting that was dominated by a plasmon-like branch independent of the SLR levels tuned above and below the excitonic resonances. The comparative high splitting energies (53-81 meV) suggested that an intermediate coupling range can be achieved from the molecular emitters located in the near-field enhancement region of AgNP arrays. Interestingly, the preferable radiative decay of the coupled system occurred on the plasmon-like lower branch of the exciton-SLR hybrid modes.

4.2. Sample Preparation and Characterization

Zn-porphyrin MOFs [146] thin films were deposited on AgNP arrays (d = 80 nm, height h = 60 nm, and periodicity p = 450 nm) by layer-by-layer method (**Figure 4.1a**) The Zn-porphyrin structure is depicted on the right side of Figure 4.1a, indicating the coordination of the porphyrin ligands with the Zn-ions with well-defined order. We conducted X-ray diffraction (XRD) measurement to study the crystallinity of the Zn-porphyrin coated on AgNP arrays. Good crystallinity of the Zn-porphyrin thin films was still preserved as is evident from the characteristic (001), (002), and (003) diffraction peaks at 3.5°, 7.0° and 10.5°, respectively (**Figure 4.1b**). We

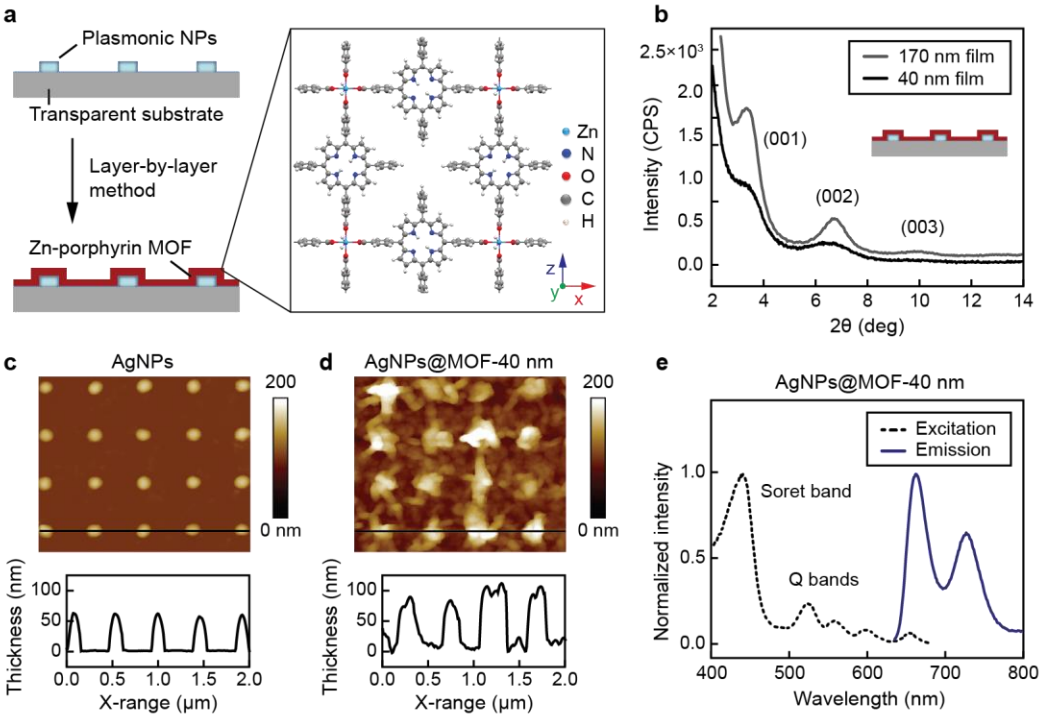

Figure 4.1 Controllable deposition of Zn-porphyrin MOF thin films on plasmonic nanoparticle arrays. (a) Scheme of the MOF thin film on AgNP arrays deposited on fused silica substrate (refractive index n = 1.46), insert shows the crystal structure of Zn-porphyrin. **(b)** XRD patterns of the thickness tunable MOF thin films deposited on AgNPs, the intensity is counts per second (CPS). **(c-d)** AFM analysis of the AgNPs with spacing p = 450 nm, diameter d = 80 nm and height h = 60 nm before **(c)** and after **(d)** coating with Zn-porphyrin thin film: topographical images (top) and cross-section analysis (bottom). **(e)** Excitation and emission spectra of the 40 nm Zn-porphyrin MOF thin film deposited on AgNP array.

noticed the enhancement of peak intensity with the increase of film thickness. The results indicate that MOF thin films are crystalline with preferred [001] orientation perpendicular to the substrate, which shows good agreement with literature report.[146]

To image the nanoscale confinement of MOF on the plasmonic NPs, we applied atomic force microscopy (AFM) to measure the topological details of AgNPs before and after coating with the Zn-porphyrin. (**Figures 4.1c-d**) Conformal coating of Zn-porphyrin on AgNP arrays was confirmed by AFM cross-section analysis, as shown in the bottom of Figure 4.1c-d. We found that the thickness of the Zn-porphyrin is about 40 nm.

Figure 4.1e shows the excitation and emission spectra of the 40 nm Zn-porphyrin thin film prepared on AgNPs using a fluorimeter. A strong band at 440 nm was observed from the excitation spectrum, attributed to *Soret* band of the Zn-porphyrin caused by electronic transition from ground state (S_0) to the second excited singlet state (S_2).[147] Four less pronounced *Q*-bands (Q_1 = 524 nm, Q_2 = 560 nm, Q_3 = 600 nm and Q_4 = 656 nm), originating from the electronic transition from ground state (S_0) to the first excited singlet state (S_1), were observed in visible spectra ranges.[147] The results indicated that free-based porphyrins were immobilized in the MOF structures. Due to large difference in fluorescence quantum yield of the *Soret* band and *Q*-bands, PL emission of the porphyrins arises from the lower energy state of the *Q*-bands.[148] For our Zn-porphyrin MOF, two typical emission bands were observed at 665 and 730 nm. (Figure 4.1e).

4.3. Hybridization of MOF-Lattice Plasmon

Figure 4.2 demonstrates the transmission spectra of the AgNP arrays deposited on fused silica substrate before and after coating with Zn-porphyrin thin film. The measurement was conducted in an index-matched environment consisting of immersion oil (n = 1.50) and fused silica substrate. As shown in **Figure 2.2a** (black line), the broad resonance around 515 nm was the LSP from single AgNP in array, and the peak around 470 nm was due to Rayleigh anomaly. Most importantly, high quality SLR with a narrow line width was generated at 665 nm. As confirmed by FDTD simulation in **Figure 4.3**, the electric field near AgNPs becomes significantly enhanced at SLR, which is

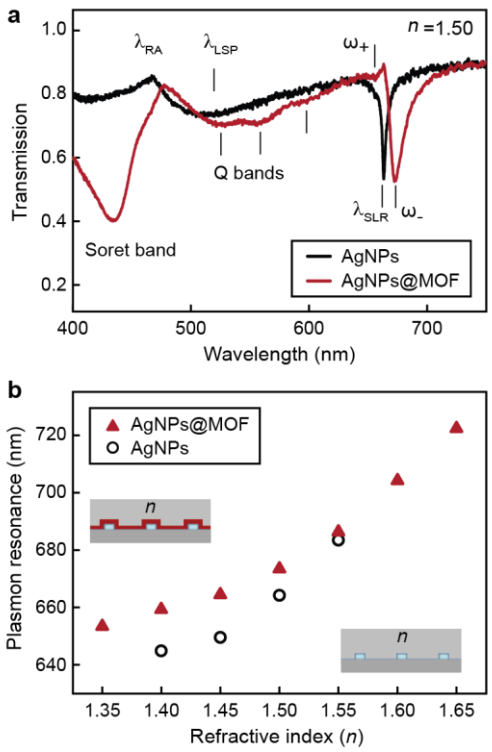

Figure 4.2 Coupling of the surface lattice resonances in AgNP arrays with Q4 band excitons in Zn-porphyrin MOF with refractive index matched environments. (a) Transmission spectra of AgNP arrays before and after coating with the Zn-porphyrin in a homogenous refractive index environment of n = 1.50. **(b)** Peak wavelength of SLR for bare AgNP arrays and peak wavelength of the strong plasmon-like mode (ω_-) for the coupled AgNPs@MOF hybrid system as a function of different indices ranging from n =1.35 to 1.65, and the transmission spectra are plotted in Figure S5. Periodicity of AgNP arrays is p = 450 nm, and the thickness of MOF is t = 40 nm.

much higher than that of the single NPs at LSPs. Figure 4.2a red line shows the transmission spectra of the hybrid AgNPs@MOF system. The *Soret* band and *Q*-bands of Zn-porphyrin appeared upon MOF coating. In addition, the strong plasmon-like mode occurs at 674 nm and is redshifted compared to the SLR of bare AgNPs, and a weak mode appears at 655 nm which is slightly bluer than the Q_4 of Zn-porphyrin. We attribute these modes to lower (ω_-) and upper (ω_+) branch of the exciton-plasmon hybridization. Due to the small transition dipole moment of the excitons in *Q*-bands of porphyrin,[149] exciton-like mode ω_+ is much less intense than the plasmon-like mode ω_-, and the hybridization is dominated by the strong lattice plasmon.

To investigate the hybridization, we tuned SLR over a wide wavelength range by changing dielectric environments.[150] The strong plasmon-like modes are sustained in the coupled system and vary over a broadband by tolerating huge index mismatch between immersion oil and substrate. **Figure 4.2b** exhibits the spectral positions of the SLR in bare AgNPs as well as the strong plasmon-like mode (ω_-) of the hybrid AgNPs@MOF system as a function of the index environments. The plasmon-like mode ω_- in hybrid system is redshifted for 14.7 nm with respect to the SLR of the bare AgNPs in the same index-environment (n = 1.40), and the shift becomes smaller and smaller when the spectra are less overlapped. The results suggest the advantages of study hybridization in our coupled system, since we can detune the plasmon energy without changing the plasmonic nanostructure.

4.4. Transient Absorption Spectra and Dynamics of Hybrid States

To understand the excited-state interactions of the coupled modes, we conducted transient absorption (TA) measurements to monitor the excited-state interactions and dynamics with a

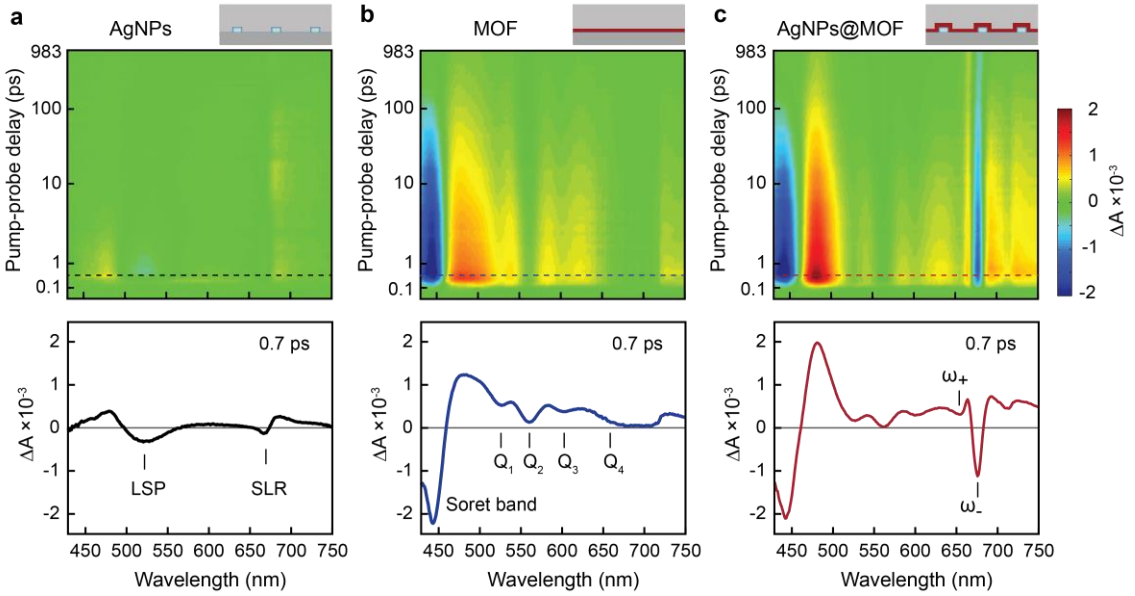

Figure 4.3 Transient absorption (TA) provides evidence of electron population of the hybrid states for coupling of the Zn-porphyrin with AgNP arrays. (a-c) TA spectral maps (top) and cross-section at ~700 fs delay time when the Δ*A* reaches maximal (bottom) for (a) pristine AgNP arrays, (b) Zn-porphyrin and (c) the hybrid AgNPs@MOF pumped at 400 nm with the fluence of 64 μJ/cm^2; Q_1-Q_4 represent the four *Q*-bands of Zn-porphyrin, and ω_+ (upper branch) and ω_- (lower branch) indicate the exciton-plasmon hybrid states. Spectra were recorded with the index of the environment at n = 1.50.

femtoseconds laser excitation at 400 nm. For bare AgNPs (a_0 = 450 nm), we observed a broad bleaching signal at 525 nm associated with transient absorption at the wings of the bleach at 480 nm and 600 nm (**Figure 4.3a**), corresponding to the LSP of isolated Ag NPs. [151] The SLR of the AgNP arrays showed a very weak bleaching signal centered at 669 nm. For the pristine Zn-porphyrin thin film (t = 40 nm), ground state bleaching of the Soret band was at 443 nm along with induced absorption at 481 nm, followed by the *Q*-bands at Q_1 = 526 nm, Q_2 = 562 nm, Q_3 = 602 nm, and Q_4 = 658 nm (**Figure 4.3b**). For the hybrid AgNPs@MOF system (**Figure 4.3c**), we observed a strong photo-bleaching signal, appeared within 50 *f*s after photon excitation (**Figures 4.4a-b**), at 676 nm along with a weaker dip at 655 nm that persisted over the 1 ns window without

completely decaying to zero. The line-shape and intensity of the bleaching signals showed distinctive difference from the exciton and plasmon spectra (spectra of MOF and Ag NPs), which

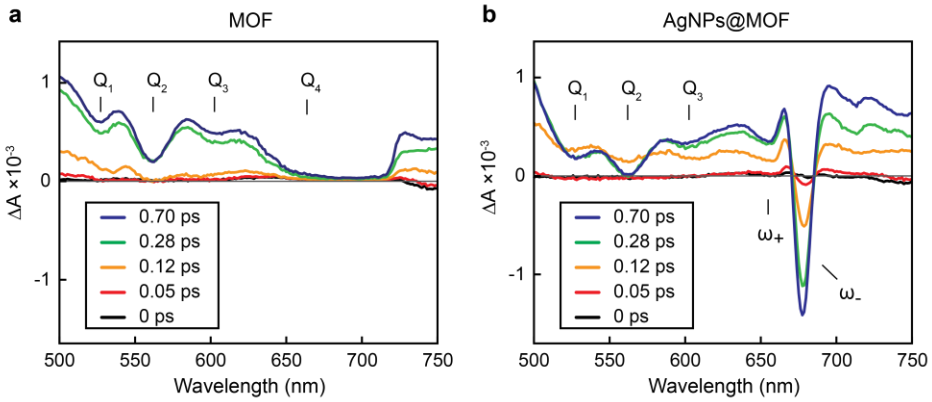

Figure 4.4 Building up the maximal amplitude of ΔA in TA. TA spectra of the early pump-probe delays (0–0.70 ps) for **(a)** pristine MOF (Zn-porphyrin thin film, t = 40 nm) and (b) the same thickness of Zn-porphyrin deposited on AgNP arrays (AgNPs@MOF) in refractive index of n = 1.50. The hybridized modes (ω_- and ω_+) were generated within 50 fs after photon excitation. Note that, no bleaching signal appeared between 650 nm and 750 nm for the pristine Zn-porphyrin

further supported the formation of the hybridized states by exciton-SLR coupling. Consistent with the linear optical properties (Figure 4.2), the lower branch (ω–) has higher intensities due to the stronger plasmonic character of the hybrid mode.

To verify the generality of these hybrid states, we tested coupling between the Q_3-band excitons in Zn-porphyrin and the SLRs in AgNP arrays by changing the lattice spacing (a_0 = 400 nm) and particle size (d = 70 nm and h = 60 nm). Similar photo-bleaching signals were also observed in TA that persisted over 1 ns time window (**Figure 4.5**). Thus, our MOF platform

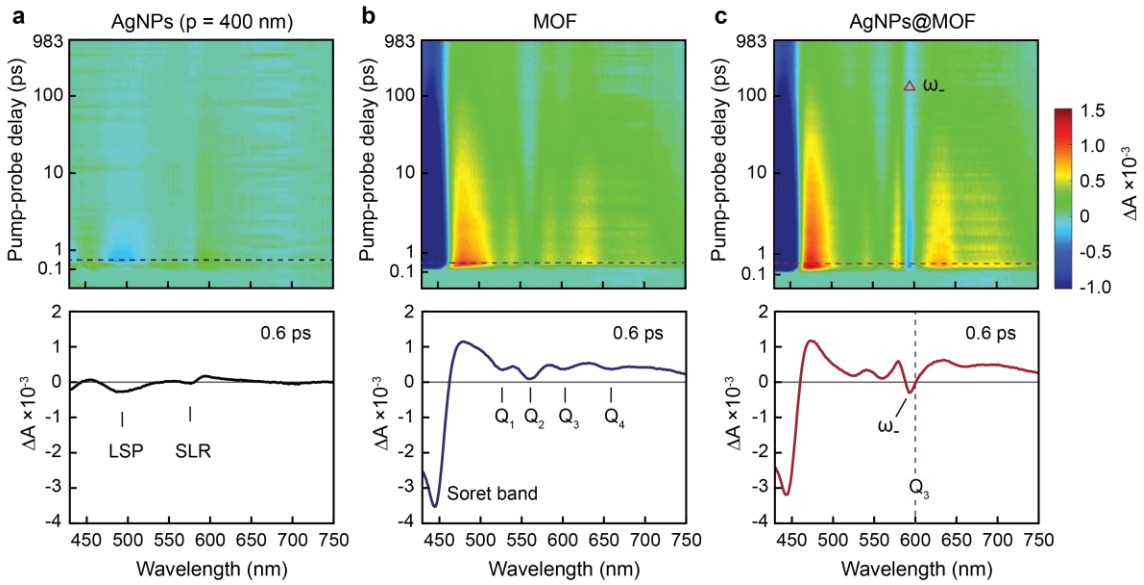

Figure 4.5 Transient absorption (TA) provides evidence of electron population of the hybrid states from coupling of the Zn-porphyrin with AgNP arrays (a_0 = 400 nm). (a-c) TA spectral maps (top) and cross-section at ~600 fs delay time when the Δ*A* reaches maximal (bottom) for (a) pristine AgNP arrays, (b) Zn-porphyrin and (c) the hybrid AgNPs@MOF pumped at 400 nm with the fluence of 32 μJ/cm^2. Spectra were recorded with the index of the environment at n = 1.50.

enabled hybrid plasmon-exciton states at different energy levels using the high quality SLRs in the AgNP arrays.

The hybrid modes for AgNPs@MOF had different decay dynamics compared with either excitons in Zn-porphyrin or the plasmon in AgNP arrays. A bi-exponential decay function fit revealed that the decay lifetimes of the excited upper branch (ω_+) for the hybrid system (τ_1 = 1.0 ps and τ_2 = 48.8 ps) were considerably faster than that of the pristine MOF (τ_1 = 24.2 ps and τ_2 = 277.9 ps) (**Figure 4.6a**). Significant differences also appeared for the excited lower branch (ω_-), where the ΔA signal was negative because of strong photo-bleaching (**Figure 4.6b**). The decay lifetimes of the ω_- mode (τ_1 = 4.9 and τ_2 = 104.8 ps) were comparable to the ω_+ mode but shorter than the pristine MOF at the same wavelength. The long-lived ΔA signal (τ_2) in the pristine MOF has previously been ascribed to triplet state formation,[146] which can be also applied in the hybrid states. For the bare AgNPs, the ΔA signal at the LSP resonance yielded a lifetime of 1.4 ps by fitting with a mono-exponential decay function (**Figure 4.7**), which was typical from electron-phonon scattering.[151] Decay lifetime of the bleaching signal at the SLR (2.3 ps) was longer than that of the LSP due to the weaker plasmonic character of the SLR.[152] Compared to the hybridized

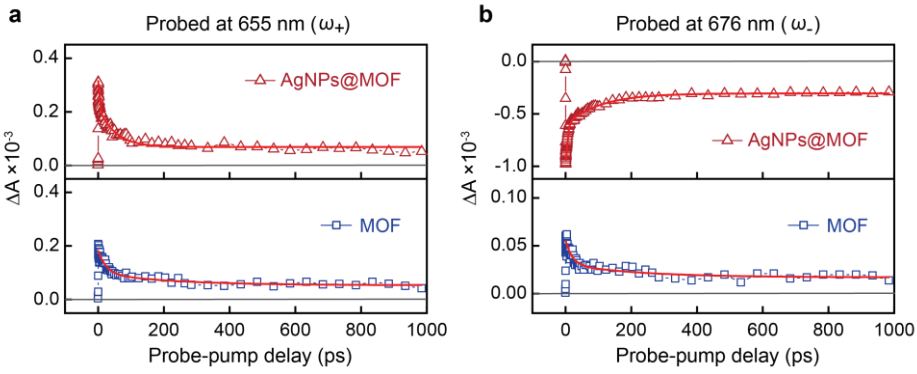

Figure 4.6 Temporal evolution of TA dynamics for the exciton-SLR hybridized state. Decay of ΔA signal at a probe wavelength of 655 nm **(a)** and 676 nm **(b)**, indicating the upper (ω_+) and lower (ω_-) branches of the coupled system in Figure 4.3c; the decay of the ΔA signal for the pristine MOF was probed at the same wavelength for comparison. The red lines represent bi-exponential decay fitting of the kinetics.

states for the AgNPs@MOF system (Figure 4.6), both SLR and LSP decayed rapidly in the bleaching signal (Figure 4.7). We verified that MOF exciton-SLR coupling led to the hybrid states

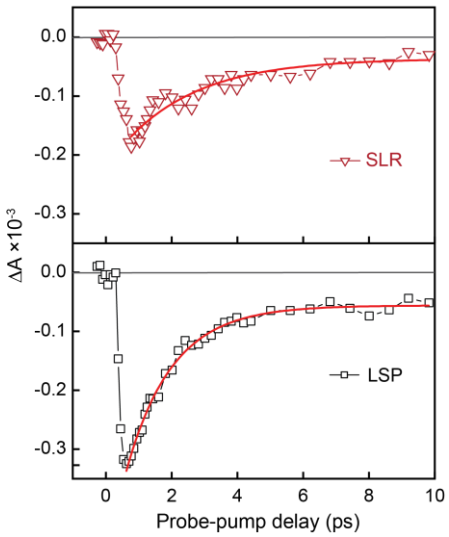

Figure 4.7 Temporal evolution of TA dynamics for the AgNP arrays (a_0 = 450 nm). Decay of Δ*A* signal at 525 nm (**top**, LSP) and 669 nm (**bottom**, SLR) for the bare AgNPs in a refractive index environment of n = 1.50. Sample was pumped at 400 nm with the fluence of 64 μJ/cm^2.

that incorporate the longer excitonic lifetime.

Figure 4.8a depicts a scheme of the energy level diagrams after coupling Q_4-band excitons to SLRs, in which the energy levels of the hybrid states (ω_+ and ω_-) were extracted from the TA spectra (**Figure 4.8b**). Here we observed the variation of the splitting energy by shifting the SLR above and below the Q_4-band exciton resonance of the Zn-porphyrin. All of the hybrid modes were dominated by the lower branch that showed photo-bleaching (Figure 4.8b and **Figures 4.9a-c**). Note that no photo-bleaching signal appeared between 600 and 750 nm for the Zn-porphyrin in different dielectric environment (**Figures 4.9d-e**). In addition, the hybrid modes shifted gradually to longer wavelength by changing the index environment from n = 1.45 to 1.55, while the Q_1-Q_3

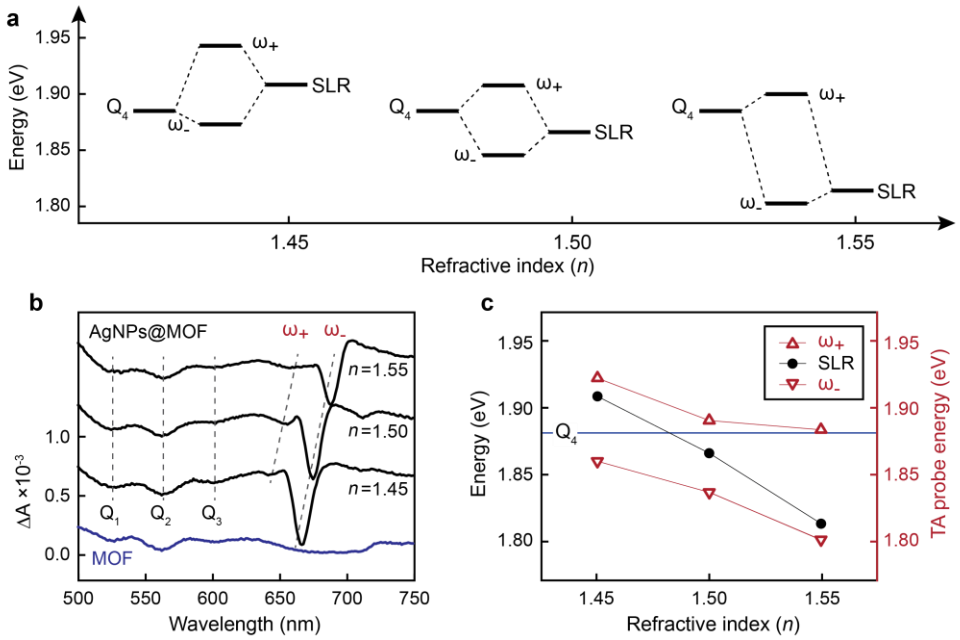

Figure 4.8 The evolution of the exciton-SLR hybridization in a single coupled system. (a) Energy-level diagrams describing the hybridization states in different dielectric environment, where the hybridization is tuned by shifting the SLR. **(b)** TA spectra (at ~600 *f*s) of the hybrid AgNPs@MOF system with index values n = 1.45, 1.50 and 1.55, and the pristine Zn-porphyrin MOF spectrum (with n = 1.50), which extracted from Figure S16. Note that the curves are shifted up from the MOF spectrum for clarity, the pump wavelength is 400 nm and the fluence is 27 μJ/cm^2. **(c)** Variation in the hybridized state energies with refractive index (n) based on the peak wavelengths from Figure 4b, also plotted are the SLR wavelengths for AgNP arrays extracted from Figure 2b. The peak center of the Q_4 band is plotted as a horizontal blue line.

bands of Zn-porphyrin kept stable. **Figure 4.8c** can be used to determine the coupling strength as a function of the SLR levels manipulated by dielectric environment. The splitting energies (difference between ω_+ and ω_-) of the hybrid states were 62 meV, 53 meV and 81 meV for the indices of n = 1.45, 1.50 and 1.55, respectively. Since the oscillator strength of the Q-band excitons in porphyrin is weak,[149] the relatively high splitting energies were contributed by the strong near-field of AgNP arrays at SLR that coupled with excitons in the spatially organized MOFs. In addition, only the lower branch of hybridization appeared in the intermediate coupling regime for

a *J*-aggregate coupled to single nanoparticle plasmons.[153] Therefore, we believe that a new type of coupling regime was reached in the AgNPs@MOF system, which showed asymmetric mode splitting dominated by a strong plasmon-like branch.

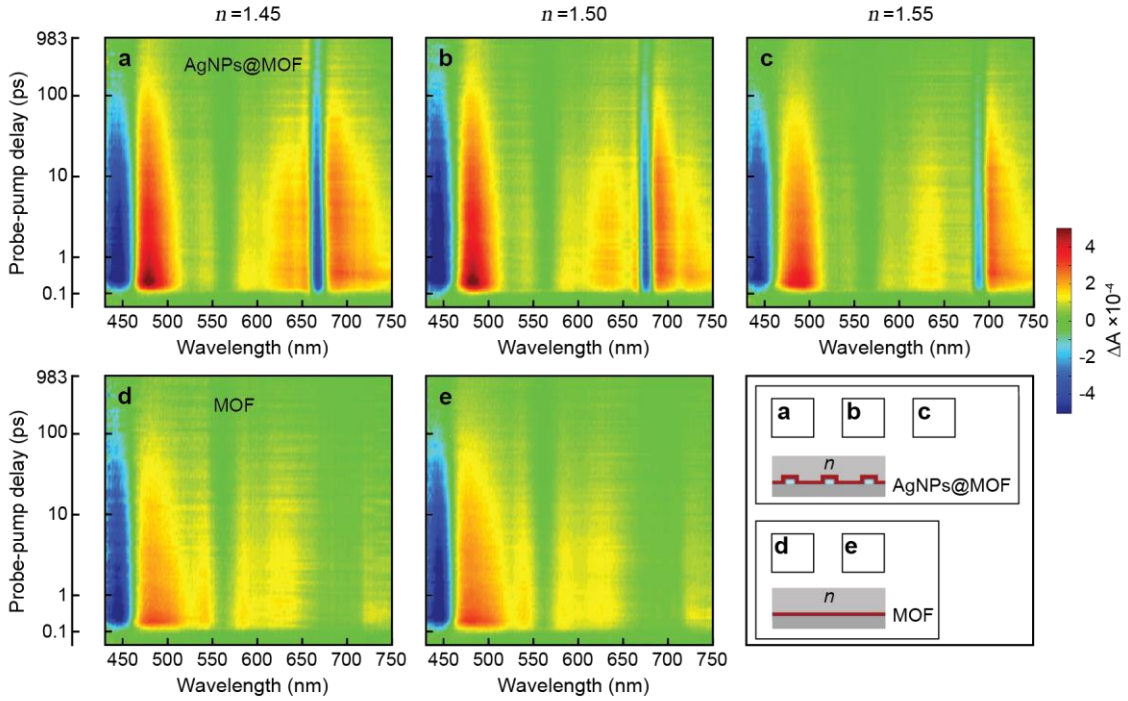

Figure 4.9 Evolution of the Q4-band exciton-SLR hybridization in a single coupled system (a_0 = 450 nm). (a-c) TA maps for the Zn-porphyrin thin film coated AgNP arrays (AgNPs@MOF) for different indices ranging from n = 1.45 to n = 1.55. **(d-e)** transient absorption spectral maps for the Zn-porphyrin thin film deposited on fused silica substrates (MOF) with indices of n = 1.45 and n = 1.50. The pump wavelength is λ = 400 nm with a fluence of 27 μJ/cm^2; Periodicity of the AgNP arrays is a_0 = 450 nm, and thickness of the MOF is t = 40 nm for either on array or off array of the AgNPs.

4.5. Photoluminescence of Hybrid States

We further studied how hybridization influenced the PL emission of our coupled AgNPs@MOF system. In our system, the thickness of the MOF was controlled to be only about

40 nm, so the majority of the molecular emitters were located where the plasmonic near-field enhancement was strong.[154,155] We observed 16-times stronger PL enhancement (at 673 nm) relative to the pristine Zn-porphyrin under the same conditions (**Figure 4.10a**). Although the emission peak at ~727 nm was unaffected by the AgNP arrays, the emission peak at shorter wavelength split into two new peaks at λ_1 = 658 nm and λ_2 = 673 nm. This splitting and enhancing in PL emission were common at different index-environment (n = 1.45-1.55) where the SLR of AgNPs was tuned across the exciton resonance energy (**Figure 4.11**). Notably, these two emission peaks were close to the upper and lower branches of the hybrid modes (Figure 5b) in terms of

spectral position, which indicated that the PL emission originated from the two hybridized states of the AgNPs@MOF system (**Figure 4.10b**).

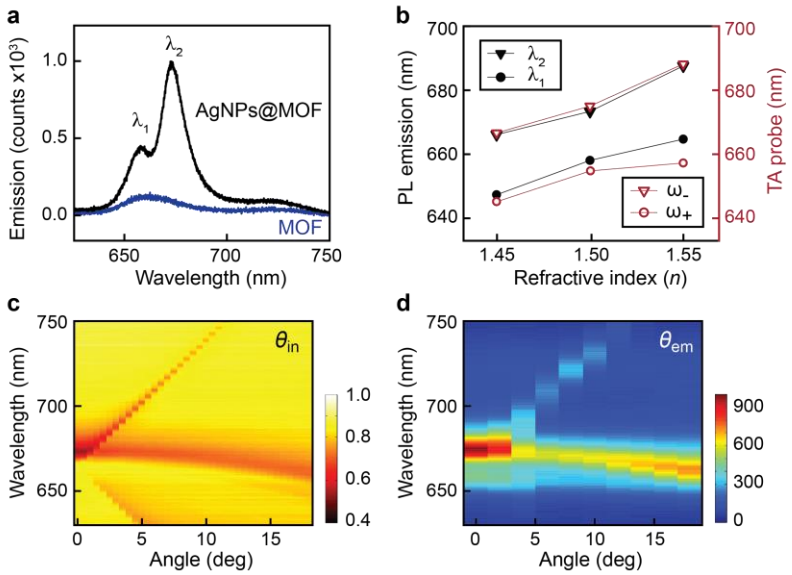

Figure 4.10 PL emission from the hybrid states of the Zn-porphyrin coupled AgNP arrays. (a) PL emission spectra of pristine Zn-porphyrin deposited on plane quartz (bottom) and on AgNP arrays (top) with index of n = 1.50. **(b)** Comparison of the splitting in both PL and hybridization of the AgNP@MOF system as a function of different refractive indices; where, the wavelength of λ_1 and λ_2 was extracted from the PL spectra in Figure 6a and Figure S17, and ω_+ and ω_- was extracted from the TA in Figure 5b. **(c)** Angle dependent transmission spectra and **(d)** angle dependent PL emission of the AgNPs@MOF hybrid system. Periodicity of AgNP arrays is a_0 = 450 nm, the thickness of MOF is t = 40 nm, and index is n = 1.50.

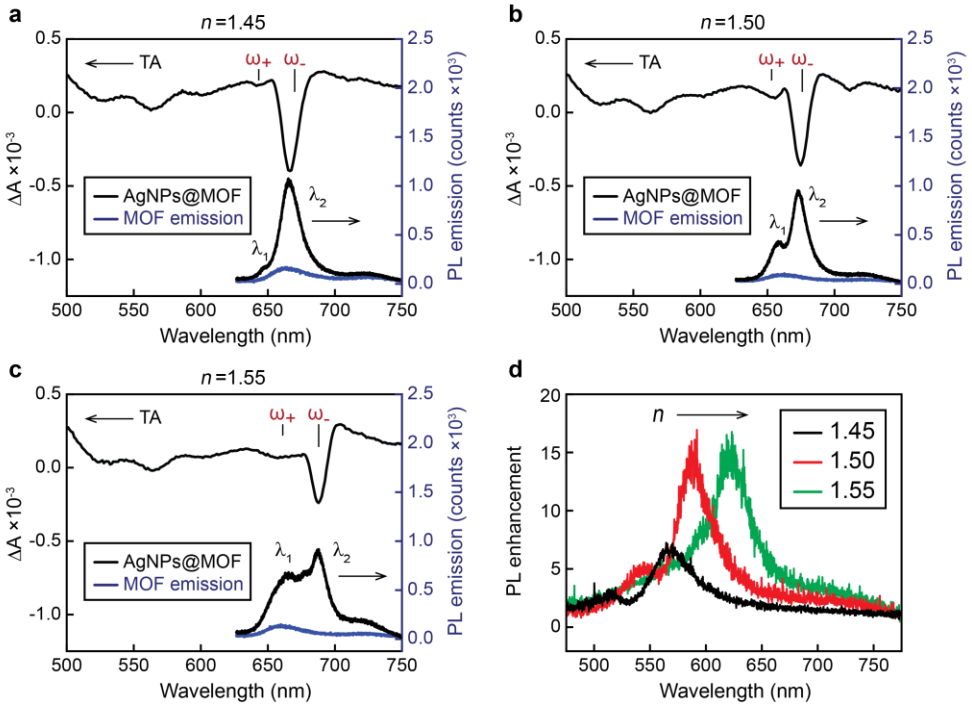

Figure 4.11 PL emission from the hybrid states of the Zn-porphyrin coupled AgNP arrays. (a-c) PL emission spectra of pristine Zn-porphyrin deposited on fused silica (blue) and on AgNP arrays (black) and TA spectra of the AgNPs@MOF (Zn-porphyrin coated AgNP arrays) in different dielectric environment: (a) n = 1.45, (b) n = 1.50, (c) n = 1.55. λ_1 and λ_2 represent the modified PL emission peaks of MOF coated on array of Ag NPs. Periodicity of the AgNP arrays is a_0 = 450 nm, and the thickness of the MOF is t = 40 nm. **(d)** Comparison of PL enhancement of the MOF coupled with AgNPs, in which the PL enhancement was calculated by dividing the AgNP@MOF emission by the pristine MOF emission.

.

No strong PL enhancement was observed on the Zn-porphyrin coated TiNP arrays (**Figure 4.12**), which revealed that PL enhancement stemmed from the plasmonic effect other than diffractive scattering within the lattice. We fabricated TiNP arrays with the diameter d = 80 nm, height h = 60 nm and periodicity a_0 = 450 nm, and then coated with the same thickness of Zn-porphyrin film (~40 nm) (**Figure 4.12**). Like to the Zn-porphyrin coated on AgNPs, the TiNP features were not changed after coating with 15 dipping cycles of Zn-porphyrin (Figures 4.12a-b). Here, weak plasmon resonance was observed in the transmission spectra due to the low polarizability of Ti (Figure 4.12c in black), which did not have a significant effect on the plasmon

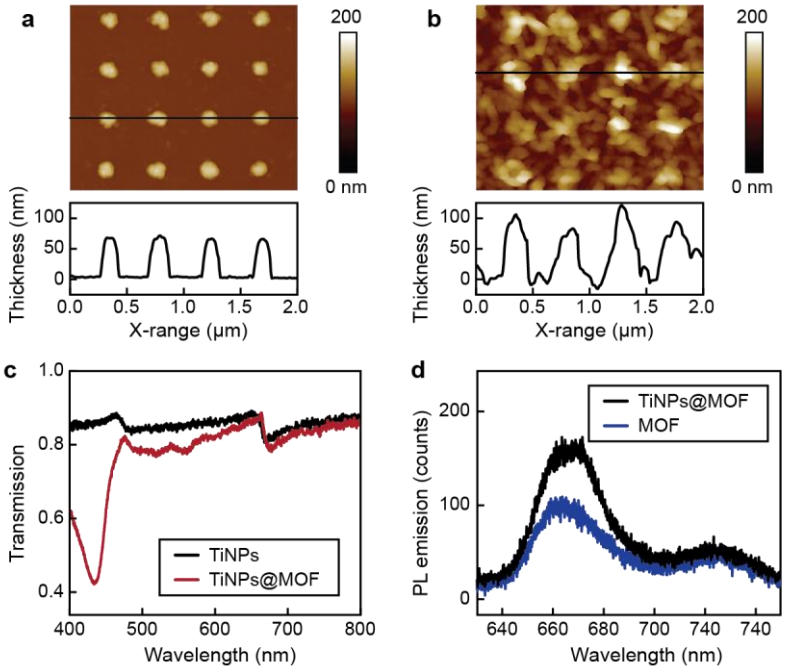

Figure 4.12 TiNP arrays (a_0 = 450 nm) coated with Zn-porphyrin MOF thin films. (a-b) AFM topographical images of the TiNP arrays before **(a)** and after **(b)** coating with Zn-porphyrin MOF thin film (top), and the cross-section analysis cross the line (bottom). **(c)** Transmission spectra of the TiNP arrays before and after coating with Zn-porphyrin. **(d)** PL emission spectra of the pristine Zn-porphyrin deposited on fused silica (blue) and on TiNP arrays (black) in a refractive index environment of n = 1.50.

properties (Figure S18c in red). Compared to pristine Zn-porphyrin deposited on fused silica, only a small enhancement of PL emission was observed on the Zn-porphyrin coated TiNP arrays.

Figures 4.10c-d depict the coupling between Q_4-band excitons in Zn-porphyrin and propagating state of SLR in AgNP arrays that showed guided emission. The (0 ± 1) modes of SLRs in AgNP arrays blueshifted from 664 nm to 654 nm as the angle increased from 0° to 18° (**Figure 4.13**), due to the highly angular dispersion of SLRs.[156] For the coupled AgNPs@MOF system, a strong plasmon-like mode at ~674 nm appeared at surface normal referring to the intense lower branch of the hybridized modes, which blueshifted with increased incident angle θ_{in} (Figure 6c). The exciton-like upper branch was not visible due to its weak intensity. Figure 6d shows the strong PL enhancement with the maximum peak wavelength that evolved from 674 nm to 662 nm as detection angle increased from 0° to 18°. The PL emission of pristine Zn-porphyrin showed no change in both wavelength and intensity (**Figure 4.14**). With the results above, we demonstrated that exciton-SLR hybridization produced mode splitting, corresponding to a weak exciton-like mode (ω_+) and strong plasmon-like mode (ω_-). The radiative decay of the excited hybrid modes led to splitting of PL, and the emission was dominated by the intense peak at higher wavelength due to the large excited state population of the lower branch.

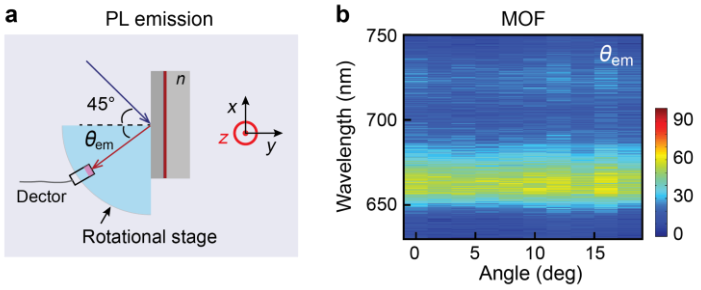

Figure 4.14 PL of MOF. (a) Scheme of the setup for angle-resolved PL emission measurements; the incident angle was kept at 45° for all measurements, and the detector was rotated in the *x*–*y* plane to change the detection angle θ_{em} and to get angle-resolved to get angle-resolved PL emission spectra. **(b)** Angle dependent PL emission of the pristine Zn-porphyrin MOF with the thickness t = 40 nm in a refractive index environment of n = 1.50.

4.6. Conclusions

In summary, we demonstrated the hybridized states arising from the coupling between the excitons from densely packed molecular emitters in a Zn-porphyrin MOF and SLRs in AgNP arrays. Nanoscale confinement of the luminescent MOF provided a noval strategy to concentrate molecular emitters that can be integrated into the near-field enhancement region of the plasmonic nanocavity. We found that the hybrid modes are dominated by a plasmon-like lower branch due to the strong field enhancement of the SLR. Evolution of the modes was observed in a single coupled materials system by simply varying the index-environment. We further demonstrated the splitting in PL from our coupled system that corresponds to enhanced fluorescence from the hybrid modes of the AgNPs@MOF system. We believe spatial organization of the functional MOFs into

plasmonic nanostructures provides a general strategy to develop their applications in nonlinear optics and photovoltaics. [3]

[3] Referenced Work: Jianxi Liu, Weijia Wang, Danqing Wang, Jingtian Hu, Richard D. Schaller, George C. Schatz and Teri W. Odom, “Hybridization of MOF Excitons to Lattice Plasmons of Nanoparticle Arrays”, in preparation

CHAPTER V. PLASMONIC LASING WITH COLLOIDAL QUANTUM DOTS

5.1 Introduction

Plasmonic cavities support a high local density of optical states that enable enhanced gain and even lasing in a variety of cases. While previous studies mostly have focused on laser dyes or bulk semiconductors coupled to plasmonic cavities, there is a great potential for the use of unconventional emitters within these systems. The development of lasers based on nanoscale emitters such as quantum dots (QDs) [157] is of increasing interest to the scientific community. CdSe nanocrystals (NC) have attractive properties that overcome some challenges of using traditional laser dyes or bulk semiconductors as the gain material, such as higher quantum efficiency, resistance to photo-degradation and bleaching, and wavelength tunability based on size.

Quantum dots (QDs) are well-known emitters for supporting extremely high quantum efficiency without photo-degradation. [129,158,159]It has a broad range of absorption, long excited state lifetime, and easily tunable emission wavelength by simply changing their size or composition.[160] Previous studies on quantum dots with a plasmonic structure are mainly focused on manipulating or enhancing PL signals.[161-173] There are few reports on using quantum dots as a quantum emitter transferring energy into plasmonic structure and inducing plasmonic emission. Notably, different from excitons in dye molecules, the excitons in QDs are delocalized Wannier excitons[174], whose interaction with plasmons has not been fully studied. Also, the way in which multi-excitons excitations in QDs will respond to plasmonic enhancement also piques our interest.[175] Although QDs have been theoretically considered as low-threshold gain media and even been used as an ideal emitter in the original SPASER design[176], the QD laser is still a challenge because of the defect formation of QD surface that leads to non-radiative recombination losses.

Here, we will employ biaxially strained QDs as the gain medium and integrate them as films onto plasmonic cavities. This type of CdSe QDs have been proved to have the quantum yield of close to unity and lasing action under a continuous wave pump.[177] We achieved s exciton coupling with SLR for lasing action and characterized the dynamics of lasing signal which shows identical plasmonic lasing feature and material dependence. We also observed p exciton coupling with lattice plasmon mode

5.2. Sample Preparation

Dye molecules in organic solvent provide merits for plasmonic lasing, as the dye molecules can constantly be refreshed at hotspot and thus prevent the deterioration of lasing due to degradation. However, quantum dots in the solution were not an ideal choice since quantum dots has a physical size of nm and the concentration of QD solution cannot reach as high as that of the dye molecules. (~mM) And the solvent such as hexane or octane will evaporate in a very short time scale during experiment. Changing solvent into toluene and xylene can slow down the evaporation rate to mitigate this issue, but the QD concentration (~uM) still affects the coupling between them and plasmonic structure. Methods such as Langmuir–Blodgett[178] applied to transfer compressed monolayers of QD to plasmonic surface. With repetition, multiple monolayers of QDs can be transferred to plasmonic surface, but the technique is limited to form 5-6 layers. (~25 nm) However, more QD layers (~ 100 nm) are required to observe lasing action.

Dropcasting is another straightforward method to transfer compacted 100-nm scale thick QD layers to plasmonic substrate. The coffee ring structure formed during evaporation of solvent caused uneven QD film thickness across samples. There are several important factors to enhance

the film quality of QD during drop casting method. Appropriate concentration of ligands in the QD solution is critical. Excessive ligands will affect the drying process, likely because some micelle formation occurs as the solvent evaporates. Too few ligands will cause the dots to agglomerate during the drying process as the concentration increases. A trial and error process should be applied to figure out how many washing cycles are required for each quantum dot batch. Another issue is the solvent of QDs. A recommended use of a hexane / octane mixture (9:1) as the solvent for the drop cast can balance surface wettability and evaporation rate, but this ratio is also dependent on substrate and atmosphere.

Eventually we used a standard spin casting for QD to achieve high quality compacted 100 nm scale thickness of QD layers (**Figure 5.1**). To achieve maximum coupling efficiency between CdSe NC and plasmonic resonance, we fabricated Al or AgNP arrays with periodicities of 342 nm (hexagonal lattice) and 400 nm (square lattice). Also note that SLR required uniform refractive

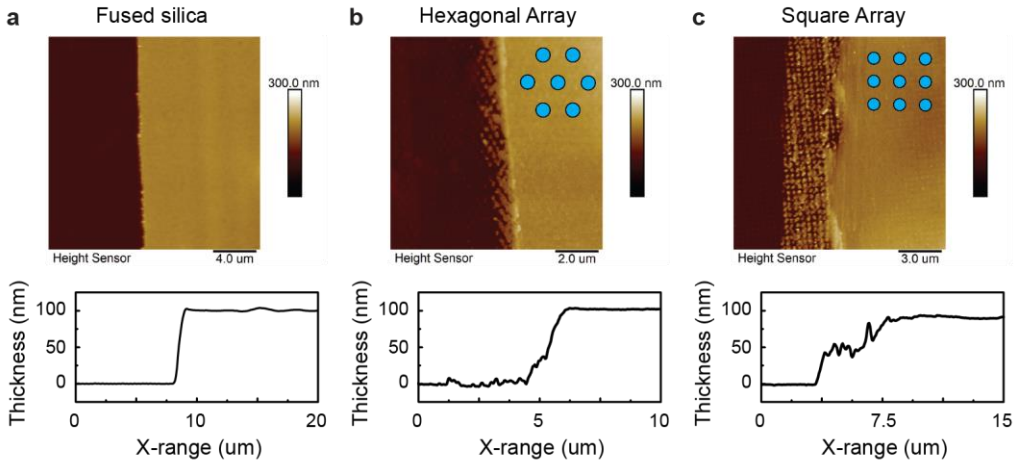

Figure 5.1 AFM of QD film on various plasmonic substrates. (a) fused silica (b) Hexagonal AlNP array (c) Square AlNP array

index environment. Despite the high refractive index of CdSe materials, (n = ~2) we covered samples with PDMS (n = 1.4) as top coating layer. This will also prevent oxidation of samples.

5.3. Exciton Coupling with Lattice Plasmon

Chloride exchanged, biaxially strained QDs dispersed in acetonitrile were spun onto AgNP arrays (p=400 nm, d=80 nm, h=60 nm). The effective refractive index increased because of the CdSe material, SLR redshifted from 575 nm to 646 nm (**Figure 5.2a**). QD has absorption from 350nm -550 nm, and emission centered at 630 nm. 400 nm femtosecond pulsed laser (repetition rate: 1kHz) is used at pump source for QDs.

Lasing action showed up in QD at 635 nm with threshold around 0.063uJ/cm^2, which is 3-order of magnitude smaller than plasmonic lasing with organic dye molecules. (**Figure 5.2c**) When the top coating PDMS layer was peeled off, SLR was extinct due to the refractive index mismatch, but the substrate still offered grating structure for optical feedback for lasing. A lasing mode at 615 nm was observed with QD layers on grating structure (**Figure 5.2d**). Compared to plasmonic lasing, the grating lasing had a higher threshold (0.413 uJ/cm^2) and a

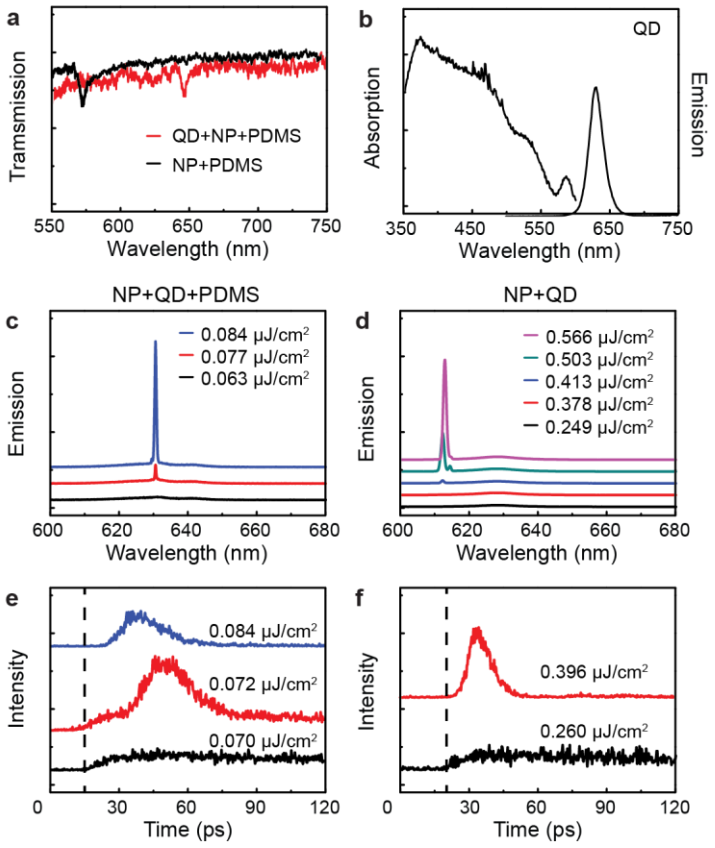

Figure 5.2 S exciton coupling with lattice plasmon (a)Transmission spectra of SLR in AgNP array + QDs (b)Absorption and emission of QDs. (c)Lasing from plasmonic effect. (d)Lasing from grating effect. Time-resolved PL of (e) plasmonic lasing and (f) lasing from grating effect.

wider linewidth (1 nm). The plasmonic factor of the system benefits to lower the lasing threshold and spectral coherence of emission. To further confirm the nature of plasmonic lasing, we measured the emission dynamics with a streak camera. Plasmonic lasing signal had an intrinsic rising time and the lasing signal showed up earlier when increasing the pump intensity, which is similar to the dye molecule system (**Figure 5.2e**). The decay lifetime of the lasing signal is 19 ps, which is dramatically shorter than original nanosecond lifetime. These two features indicate that the exciton-plasmon interaction responds to lasing action. In the grating system, the lasing signal did not have a rising time, and with almost similar start time as spontaneous mission (**Figure 5.2f** black line). The decay lifetime is 9 ps, which is shorter than in the plasmonic case. SLR provides higher quality nanocavities for lasing action, the photons have been trapped inside the cavity for longer time before coherent emission, thus the decay lifetime is longer. Accordingly, the linewidth of plasmonic lasing is narrower.

5.4. Plasmonic Material Dependence

To eliminate the grating factor in SLR samples, we fabricated AgNP and AlNP with idential geometry (hexagonal array, p=346 nm, d=50 nm, h=60 nm). Due to the change of plasmonic material from Ag to Al, the SLR blue shifted 12 nm in simulations with refractive index envrioment n=1.45 (**Figures 5.3a-b**). Note that the wavelength range is close to the interband transition of Ag, and the Ag SLR has lower quality than Al's.

QDs spincaseted onto these two plasmonic substrates, and a lasing peak was observed at 637 nm in Ag system and at 622 nm in Al system. Both emissions had a very short decay lifetime of around 6 ps (**Figures 5.3 e-f**). This 15 nm blue shift of emission peak indicated that the plasmonic compoent of SLR is critial to lasing.

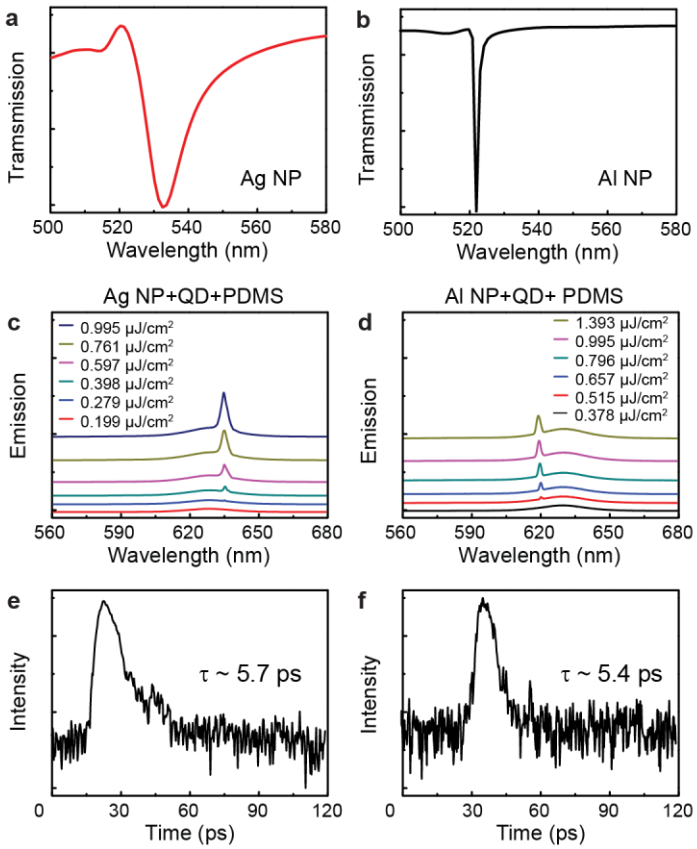

Figure 5.3 Plasmonic material dependence. Simulated transmission spectra of (a)AgNP arrays and (b) AlNP arrays. Lasing from (c) AgNP+QDs and (d)AlNP+QDs. Time resolved emission from (e)AgNP+QDs and (f)AlNP+QDs

5.5. Non-Directional Emission from Hexagonal Arrays

Compared to previous section, the emission has a relatively border linewidth (2 nm), which could be contributed by the degradation of QDs or amplified spontaneous emission. Unlike the plasmonic lasing from square lattice, where lasing has high directionality at surface normal, emissions from hexagonal array do not have specific directionality. The emission was detected from both surface normals up to 20 degree off. (**Figures 5.4 a-b**) The potential exmaplation is the hexagonal lattice provide far field modification with more uniform emission pattern. Similar phenomena have been reported in LED devices embedded with a hexagonal lattice.[37]

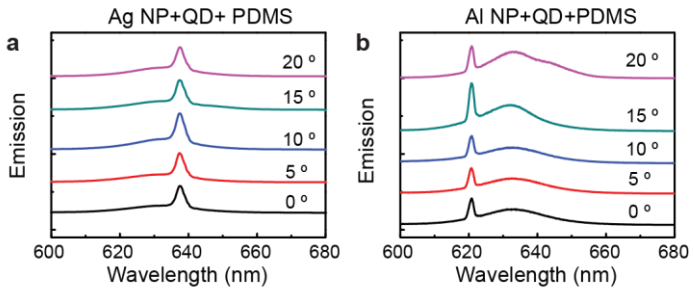

Figure 5.4 Emission of lasing at various detection angles

5.6. Conclusions

In summary, plasmonic lasing with biaxially strained QDs was achieved and with much lower threshold than that of organic dye molecules system. Plasmonic and grating contribution of SLR to the lasing signal was investigated by using different plasmonic material and characterization of the lasing dynamics. If pump-thresholds can be sufficiently lowered in QDs, electrical pumping using current might also be feasible, which would eliminate the use of complicated optical energy sources. Study of excitons in QDs coupling to plasmon might uncover

a new fundamental understanding of exciton-plasmon interactions for emitters of diverse electronic structures. [4]

[4] Referenced Work: Weijia Wang, Fengjia Fan, Oleksandr Voznyy, Ran Li, Jianxi Liu, Richard. D. Schaller, George C. Schatz, Edward H. Sargent and Teri W. Odom, “Plasmonic lasing with Colloidal Quantum Dots”, preliminary results

METHODS

Fabrication of nanoparticle arrays: Poly(dimethylsiloxane) masks with spacing *p*=346 nm, 400, 450, 480nm, 600 nm were used in phase-shifting photolithography/embossing process to produce photoresist pattern on Si (100) wafers. After depositing a thin layer of Cr (10 nm) and lift-off photoresist posts, we used deep reactive ion etching to create cylindrical pits beneath the circular Cr holes into the Si. Additional Au deposition will further shrink the dimension of nanohole arrays. After etching of the Cr sacrificial layer, Au nanohole arrays were floated onto substrates as deposition masks and then could be removed by Scotch tape. Additional atomic layer deposition of Al_2O_3 was used for preventing oxidation of AgNP.

Time-resolved emission dynamics: A streak camera was utilized to characterize fluence-dependent, wavelength-resolved photoluminescence decay experiments and to characterize different lasing modes. A 1 KHz amplified Ti:sapphire laser operating at 400 nm or 800 nm excited samples at an incident angle of 0° or 45°. The photoluminescence signals were passed through longpass and neutral density filters, and then coupled to a fiber optic on a sample-concentric rotational stage. Fiber-coupled signals were directed to the entrance slit of a 0.15m grating spectrometer and the dispersed emission was detected with a single-photon sensitive streak camera. The emission decay lifetime, *t*, was obtained from fitting the data with an exponential decay function $y = y_0 + Ae^{-(x-x_0)/t}$.

Lasing measurement: NP arrays embedded with gain materials were pumped with a mode-locked Ti:sapphire laser with a regenerative amplifier laser (400nm or 800nm wavelength, 100-2 kHz repetition rate and 90 fs pulse width). Lasing signals were collected normal to the sample

surface and directed to a CCD spectrometer (LN2-cooled CCD/Triax 552, Horiba Jobin Yvon, ~0.15 nm resolution) For angle-resolved emission measurements, we fixed the sample at the center of a rotational stage with a protractor and collected emission signals at off normal angles. The collected signals were then directed to a compact spectrometer (USB 2000, Ocean Optics, 0.3 nm resolution) through an optical fiber. The far field emission patterns were analyzed by a high-resolution charge-coupled device beam profiler (LBR-HR, Newport, 1.4 Megapixel). By placing the beam profiler at different emission distances normal to the sample surface, the spatial coherence was characterized.

FDTD simulations of lasing and ASE: FDTD calculations based on commercial software (FDTD solution, Lumerical Inc., Vancouver, Canada) were used to simulate the linear properties of Au NPs. The optical constants of gold were taken from Johnson and Christy (400–1000 nm). A uniform mesh size of 2 nm (x, y and z directions) was used to ensure accuracy of electric and magnetic field calculations within the metal NPs.Simulation of lasing and ASE was performed by the same software (FDTD Solutions, Lumerical Inc.), where a four-level two-electron model was integrated with FDTD for modelling dye molecules. In the four-level systems, we set the NP geometry for optimized SLR, dye concentration same as experimental data. Pump wavelength at λa =400nm or 800 nm and dye emission at $\lambda e = 660$ nm or 860 nm with bandwidth $\Delta\lambda e = 100$ nm, which is close to experimental conditions. Initially, we pumped the four-level system from the ground state (population density $N0 = 1$, $N1 = N2 = N3 = 0$) and collected all emitted flux with a plane monitor placed 0.3 μm away on top of the NPs. Mapping of stimulated emission was collected by a matrix of plane monitors placed in the middle or top cross plane of the NP arrays.

MOF thin film deposition: Zn-porphyrin MOF thin film was produced by a dipping method, which also involves a layer-by-layer approach for MOF production.[146] In this process, a sample of NPs deposited quartz substrate was immersed sequentially in an ethanol solution of zinc acetate (0.5 mM) and 5,15-diphenyl-10,20-di(4-carboxyphenyl)porphyrin (0.02 mM). Ethanol rinsing in between each immersion was performed to remove excess reagents. Different thicknesses of the Zn-porphyrin MOF thin films could be realized by varying the number of dipping cycles. After deposition, the MOF deposited on the backside of quartz substrate was removed by nitric acid (0.1 mM) for all of the following characterizations.

AFM characterization: Tapping mode AFM was applied to characterize the morphology and height of the AgNPs and TiNPs before and after MOF coating. For MOF thickness measurement, a small area of the MOF samples was removed, in order to have an internal reference for the height measurement, from the substrate by immersing into nitric acid (0.1 mM) for about 2 seconds, then immediately rinsed with ethanol and dried under N_2 stream.

TA characterization: A Ti:sapphire laser was used for TA measurements, which produced 35 fs pulses at 2 kHz. The 800 nm output was split into two beams, one beam was directed into a beta barium borate (BBO) crystal to produce the double frequency of 400 nm excitation pulse, another beam was focused into a sapphire crystal to generate white-light-continuum probe pulse. All sample were excited at 400 nm at incidence angle of 45° with a beam diameter of 2 mm, and a probing wavelength from 430 nm to 750 nm was selected to monitor the transient states at different pump-probe delays (beam diameter, 0.5 mm). TA absorption spectra was measured using a CCD-spectrometer settled on backside of sample at normal. At the end, the absorbance difference (ΔA) was plotted as a function of pump-probe delay time from 0 to 983 ps.

PL characterization: Wavelength and time resolved PL data were acquired using the same pulsed laser (Ti:sapphire, 35 fs pulses at 2 kHz) introduced above. A CCD camera was used to record PL spectra, and a streak camera detection system was used separately to record time-resolved PL. Samples were excited at 400 nm at incidence angle of 45° (beam diameter of 2 mm).

REFERENCE

1 Koenderink, A. F., Alù, A. & Polman, A. Nanophotonics: Shrinking light-based technology. *Science* **348**, 516, (2015).

2 Barnes, W. L., Dereux, A. & Ebbesen, T. W. Surface plasmon subwavelength optics. *Nature* **424**, 824-830, (2003).

3 Ozbay, E. Plasmonics: Merging Photonics and Electronics at Nanoscale Dimensions. *Science* **311**, 189 LP-193, (2006).

4 Fernandez-Dominguez, A. I., Garcia-Vidal, F. J. & Martin-Moreno, L. Unrelenting plasmons. *Nat Photon* **11**, 8-10, (2017).

5 Lozano, G., Rodriguez, S. R. K., Verschuuren, M. A. & Gomez Rivas, J. Metallic nanostructures for efficient LED lighting. *Light Sci Appl.* **5**, e16080, (2016).

6 Faraday, M. The Bakerian Lecture: Experimental Relations of Gold (and Other Metals) to Light. *Philosophical Transactions of the Royal Society of London* **147**, 145-181, (1857).

7 Stockman, M. I. Nanoplasmonics: The physics behind the applications. *Phys. Today* **64**, 39-44, (2011).

8 Giannini, V., Fernández-Domínguez, A. I., Heck, S. C. & Maier, S. A. Plasmonic Nanoantennas: Fundamentals and Their Use in Controlling the Radiative Properties of Nanoemitters. *Chemical Reviews* **111**, 3888-3912, (2011).

9 Bharadwaj, P., Deutsch, B. & Novotny, L. Optical Antennas. *Advances in Optics and Photonics* **1**, 438-483, (2009).

10 Hecht, P. B., Jer-Shing, H. & Bert. Nanoantennas for visible and infrared radiation. *Reports on Progress in Physics* **75**, 24402-24402, (2012).

11 Murray, W. A. & Barnes, W. L. Plasmonic Materials. *Advanced Materials* **19**, 3771-3782, (2007).

12 Kelly, K. L., Coronado, E., Zhao, L. L. & Schatz, G. C. The Optical Properties of Metal Nanoparticles: The Influence of Size, Shape, and Dielectric Environment. *The Journal of Physical Chemistry B* **107**, 668-677, (2003).

13 Mühlschlegel, P., Eisler, H. J., Martin, O. J. F., Hecht, B. & Pohl, D. W. Resonant Optical Antennas. *Science* **308**, 1607-1609, (2005).

14 ten Bloemendal, D. *et al.* Local Field Spectroscopy of Metal Dimers by TPL Microscopy. *Plasmonics* **1**, 41, (2006).

15 Romero, I., Aizpurua, J., Bryant, G. W. & Abajo, F. J. G. d. Plasmons in nearly touching metallic nanoparticles: singular response in the limit of touching dimers. *Optics Express* **14**, 9988-9999, (2006).

16 Jia, C.-J. & Schuth, F. Colloidal metal nanoparticles as a component of designed catalyst. *Physical Chemistry Chemical Physics* **13**, 2457-2487, (2011).

17 Anker, J. N. *et al.* Biosensing with plasmonic nanosensors. *Nature materials* **7**, 442-453, (2008).

18 Jain, P. K., Huang, X., El-Sayed, I. H. & El-Sayed, M. A. Review of Some Interesting Surface Plasmon Resonance-enhanced Properties of Noble Metal Nanoparticles and Their Applications to Biosystems. *Plasmonics* **2**, 107-118, (2007).

19 Nie, S. & Emory, S. R. Probing Single Molecules and Single Nanoparticles by Surface-Enhanced Raman Scattering. *Science* **275**, 1102-1106, (1997).

20 Lamprecht, B. *et al.* Metal Nanoparticle Gratings: Influence of Dipolar Particle Interaction on the Plasmon Resonance. *Physical Review Letters* **84**, 4721-4724, (2000).

21 Zou, S., Janel, N. & Schatz, G. C. Silver nanoparticle array structures that produce remarkably narrow plasmon lineshapes. *J Chem Phys* **120**, 10871-10875, (2004).

22 Zou, S. & Schatz, G. C. Narrow plasmonic/photonic extinction and scattering line shapes for one and two dimensional silver nanoparticle arrays. *The Journal of Chemical Physics* **121**, 12606-12612, (2004).

23 Hicks, E. M. *et al.* Controlling plasmon line shapes through diffractive coupling in linear arrays of cylindrical nanoparticles fabricated by electron beam lithography. *Nano Lett* **5**, 1065-1070, (2005).

24 Zou, S. & Schatz, G. C. Silver nanoparticle array structures that produce giant enhancements in electromagnetic fields. *Chemical Physics Letters* **403**, 62-67, (2005).

25 Shengli, Z. & George, C. S. Theoretical studies of plasmon resonances in one-dimensional nanoparticle chains: narrow lineshapes with tunable widths. *Nanotechnology* **17**, 2813, (2006).

26 Kravets, V. G., Schedin, F. & Grigorenko, A. N. Extremely narrow plasmon resonances based on diffraction coupling of localized plasmons in arrays of metallic nanoparticles. *Phys Rev Lett* **101**, 087403, (2008).

27 Chu, Y., Schonbrun, E., Yang, T. & Crozier, K. B. Experimental observation of narrow surface plasmon resonances in gold nanoparticle arrays. *Applied Physics Letters* **93**, 181108, (2008).

28 Auguie, B. & Barnes, W. L. Collective resonances in gold nanoparticle arrays. *Phys Rev Lett* **101**, 143902, (2008).

29 Christ, A., Tikhodeev, S. G., Gippius, N. A., Kuhl, J. & Giessen, H. Waveguide-Plasmon Polaritons: Strong Coupling of Photonic and Electronic Resonances in a Metallic Photonic Crystal Slab. *Physical Review Letters* **91**, 183901, (2003).

30 Abass, A., Rodriguez, S. R.-K., Rivas, J. G. & Maes, B. Tailoring Dispersion and Eigenfield Profiles of Plasmonic Surface Lattice Resonances. *ACS Photonics* **1**, 61-68, (2014).

31 Henzie, J., Lee, M. H. & Odom, T. W. Multiscale patterning of plasmonic metamaterials. *Nat Nanotechnol* **2**, 549-554, (2007).

32 Wang, D., Yang, A., Hryn, A. J., Schatz, G. C. & Odom, T. W. Superlattice Plasmons in Hierarchical Au Nanoparticle Arrays. *ACS Photonics* **2**, 1789-1794, (2015).

33 Lozano, G., Grzela, G., Verschuuren, M. A., Ramezani, M. & Rivas, J. G. Tailor-made directional emission in nanoimprinted plasmonic-based light-emitting devices. *Nanoscale* **6**, 9223-9229, (2014).

34 Yang, A. *et al.* Real-time tunable lasing from plasmonic nanocavity arrays. *Nature Communications* **6**, 6939, (2015).

35 Abass, A. *et al.* Active Liquid Crystal Tuning of Metallic Nanoantenna Enhanced Light Emission from Colloidal Quantum Dots. *Nano Letters* **14**, 5555-5560, (2014).

36 Yang, A. *et al.* Programmable and reversible plasmon mode engineering. *Proc Natl Acad Sci U S A* **113**, 14201-14206, (2016).

37 Lozano, G. *et al.* Plasmonics for solid-state lighting: enhanced excitation and directional emission of highly efficient light sources. *Light Sci Appl* **2**, (2013).

38 Gabriel, L., Tommy, B., Grzegorz, G. & Jaime Gómez, R. Directional absorption by phased arrays of plasmonic nanoantennae probed with time-reversed Fourier microscopy. *New Journal of Physics* **16**, 013040, (2014).

39 Humphrey, A. D., Meinzer, N., Starkey, T. A. & Barnes, W. L. Surface Lattice Resonances in Plasmonic Arrays of Asymmetric Disc Dimers. *ACS Photonics* **3**, 634-639, (2016).

40 Vecchi, G., Giannini, V. & Gómez Rivas, J. Surface modes in plasmonic crystals induced by diffractive coupling of nanoantennas. *Physical Review B* **80**, (2009).

41 Zhou, W. & Odom, T. W. Tunable subradiant lattice plasmons by out-of-plane dipolar interactions. *Nature nanotechnology* **6**, 423-427, (2011).

42 Rodriguez, S. R. K. *et al.* Coupling Bright and Dark Plasmonic Lattice Resonances. *Phys Rev X* **1**, 021019, (2011).

43 Markel, V. A. Coupled-dipole Approach to Scattering of Light from a One-dimensional Periodic Dipole Structure. *Journal of Modern Optics* **40**, 2281-2291, (1993).

44 Carron, K. T., Fluhr, W., Meier, M., Wokaun, A. & Lehmann, H. W. Resonances of two-dimensional particle gratings in surface-enhanced Raman scattering. *Journal of the Optical Society of America B* **3**, 430-440, (1986).

45 Giannini, V., Vecchi, G. & Gómez Rivas, J. Lighting Up Multipolar Surface Plasmon Polaritons by Collective Resonances in Arrays of Nanoantennas. *Physical Review Letters* **105**, 266801, (2010).

46 Evlyukhin, A. B., Reinhardt, C., Zywietz, U. & Chichkov, B. N. Collective resonances in metal nanoparticle arrays with dipole-quadrupole interactions. *Physical Review B* **85**, (2012).

47 Zhou, Y. & Zou, S. Effects of Dipole and Quadrupole Modes on the Switchable Total Transmission and Reflection in an Array of Rectangular Silver Prisms. *The Journal of Physical Chemistry C* **120**, 20743-20748, (2016).

48 Taflove, A. & Hagness, S. C. *Computational electrodynamics: the finite-difference time-domain method*. (Artech house, 2005).

49 Jin, J.-M. *The finite element method in electromagnetics*. (John Wiley & Sons, 2015).

50 Auguié, B., Bendaña, X. M., Barnes, W. L. & García de Abajo, F. J. Diffractive arrays of gold nanoparticles near an interface: Critical role of the substrate. *Physical Review B* **82**, 155447, (2010).

51 Malynych, S. & Chumanov, G. Light-Induced Coherent Interactions between Silver Nanoparticles in Two-Dimensional Arrays. *Journal of the American Chemical Society* **125**, 2896-2898, (2003).

52 Burrows, C. P. & Barnes, W. L. Large spectral extinction due to overlap of dipolar and quadrupolar plasmonic modes of metallic nanoparticles in arrays. *Optics Express* **18**, 3187-3198, (2010).

53 Zhou, W. *et al.* Lasing action in strongly coupled plasmonic nanocavity arrays. *Nat Nanotechnol* **8**, 506-511, (2013).

54 Figotin, A. & Vitebskiy, I. Slow light in photonic crystals. *Wave Random Complex* **16**, 293-382, (2006).

55 Krauss, T. F. Why do we need slow light? *Nature Photonics* **2**, 448-450, (2008).

56 Guo, R., Hakala, T. K. & Törmä, P. Geometry dependence of surface lattice resonances in plasmonic nanoparticle arrays. *Physical Review B* **95**, 155423, (2017).

57 Novotny, L. & van Hulst, N. Antennas for light. *Nat Photon* **5**, 83-90, (2011).

58 Valeur, B. & Berberan-Santos, M. N. *Molecular fluorescence: principles and applications*. (John Wiley & Sons, 2012).

59 Vecchi, G., Giannini, V. & Gómez Rivas, J. Shaping the Fluorescent Emission by Lattice Resonances in Plasmonic Crystals of Nanoantennas. *Physical Review Letters* **102**, 146807, (2009).

60 Barnes, W. L. & Törmä, P. Strong coupling between surface plasmon polaritons and emitters: a review. *Reports on Progress in Physics* **78**, 13901-13901, (2015).

61 Bozhevolnyi, S. I., Martin-Moreno, L. & Garcia-Vidal, F. *Quantum Plasmonics*. (Springer International Publishing, 2016).

62 Väkeväinen, A. I. *et al.* Plasmonic Surface Lattice Resonances at the Strong Coupling Regime. *Nano Letters* **14**, 1721-1727, (2014).

63 Rodriguez, S. R. K. & Rivas, J. G. Surface lattice resonances strongly coupled to Rhodamine 6G excitons: tuning the plasmon-exciton-polariton mass and composition. *Optics Express* **21**, 27411-27421, (2013).

64 Shi, L. *et al.* Spatial Coherence Properties of Organic Molecules Coupled to Plasmonic Surface Lattice Resonances in the Weak and Strong Coupling Regimes. *Physical Review Letters* **112**, 153002, (2014).

65 Deng, H., Haug, H. & Yamamoto, Y. Exciton-polariton Bose-Einstein condensation. *Reviews of Modern Physics* **82**, 1489-1537, (2010).

66 Sanvitto, D. & Kena-Cohen, S. The road towards polaritonic devices. *Nat Mater* **15**, 1061-1073, (2016).

67 Rodriguez, S. R. K., Feist, J., Verschuuren, M. A., Garcia Vidal, F. J. & Gómez Rivas, J. Thermalization and Cooling of Plasmon-Exciton Polaritons: Towards Quantum Condensation. *Physical Review Letters* **111**, 166802, (2013).

68 Ramezani, M. *et al.* Plasmon-exciton-polariton lasing. *Optica* **4**, 31-37, (2017).

69 Hakala, T. K. *et al.* Bose-Einstein Condensation in a Plasmonic Lattice. **1706**, (2017).

70 Bergman, D. J. & Stockman, M. I. Surface plasmon amplification by stimulated emission of radiation: quantum generation of coherent surface plasmons in nanosystems. *Phys Rev Lett* **90**, 027402, (2003).

71 Oulton, R. F. *et al.* Plasmon lasers at deep subwavelength scale. *Nature* **461**, 629-632, (2009).

72 Lu, Y.-J. *et al.* Plasmonic Nanolaser Using Epitaxially Grown Silver Film. *Science* **337**, 450, (2012).

73 Ma, R. M., Oulton, R. F., Sorger, V. J., Bartal, G. & Zhang, X. Room-temperature sub-diffraction-limited plasmon laser by total internal reflection. *Nat Mater* **10**, 110-113, (2011).

74 Zheludev, N. I., Prosvirnin, S. L., Papasimakis, N. & Fedotov, V. A. Lasing spaser. *Nature Photonics* **2**, 351-354, (2008).

75 Stehr, J. *et al.* A low threshold polymer laser based on metallic nanoparticle gratings. *Advanced Materials* **15**, 1726-+, (2003).

76 Schokker, A. H. & Koenderink, A. F. Lasing at the band edges of plasmonic lattices. *Physical Review B* **90**, 155452, (2014).

77 Dridi, M. & Schatz, G. C. Model for describing plasmon-enhanced lasers that combines rate equations with finite-difference time-domain. *J. Opt. Soc. Am. B* **30**, 2791-2797, (2013).

78 Hakala, T. K. *et al.* Lasing in dark and bright modes of a finite-sized plasmonic lattice. *Nature Communications* **8**, 13687, (2017).

79 Hill, M. T. & Gather, M. C. Advances in small lasers. *Nat Photon* **8**, 908-918, (2014).

80 Fan, F., Turkdogan, S., Liu, Z., Shelhammer, D. & Ning, C. Z. A monolithic white laser. *Nat Nano* **10**, 796-803, (2015).

81 Ma, R.-M., Yin, X., Oulton, R. F., Sorger, V. J. & Zhang, X. Multiplexed and Electrically Modulated Plasmon Laser Circuit. *Nano Letters* **12**, 5396-5402, (2012).

82 Wang, D. *et al.* Band-edge engineering for controlled multi-modal nanolasing in plasmonic superlattices. *Nat Nano*, (2017).

83 Svelto, O. & Hanna, D. C. Principles of Lasers, Fifth Edition. *Principles of Lasers, Fifth Edition*, 1-620, (2010).

84 Oulton, R. F. *et al.* in *Nature* Vol. 461 629-632 (Nature Publishing Group, 2009).

85 Sidiropoulos, T. P. H. *et al.* in *Nat Phys* Vol. 10 870-876 (2014).

86 Kristensen, P. T. & Hughes, S. Modes and Mode Volumes of Leaky Optical Cavities and Plasmonic Nanoresonators. *ACS Photonics* **1**, 2-10, (2014).

87 Kristensen, P. T., Van Vlack, C. & Hughes, S. Generalized effective mode volume for leaky optical cavities. *Opt Lett* **37**, 1649-1651, (2012).

88 Griffiths, D. J. *Introduction to Electrodynamics*. (Pearson Education, 2014).

89 Cuerda, J., Ruting, F., Garcia-Vidal, F. J. & Bravo-Abad, J. Theory of lasing action in plasmonic crystals. *Physical Review B* **91**, (2015).

90 Nagra, A. S. & York, R. A. FDTD analysis of wave propagation in nonlinear absorbing and gain media. *Ieee Transactions on Antennas and Propagation* **46**, 334-340, (1998).

91 Yamada, A., Neuhauser, D. & Vallee, R. Path-selective lasing in nanostructures based on molecular control of localized surface plasmons. *Nanoscale* **8**, 18476-18482, (2016).

92 Dridi, M. & Schatz, G. C. Lasing action in periodic arrays of nanoparticles. *Journal of the Optical Society of America B* **32**, 818, (2015).

93 Bermel, P., Lidorikis, E., Fink, Y. & Joannopoulos, J. D. Active materials embedded in photonic crystals and coupled to electromagnetic radiation. *Physical Review B* **73**, (2006).

94 Chang, S. H. & Taflove, A. Finite-difference time-domain model of lasing action in a four-level two-electron atomic system. *Optics Express* **12**, 3827-3833, (2004).

95 Chua, S. L., Chong, Y. D., Stone, A. D., Soljacic, M. & Bravo-Abad, J. Low-threshold lasing action in photonic crystal slabs enabled by Fano resonances. *Optics Express* **19**, 1539-1562, (2011).

96 Huang, Y. Y. & Ho, S. T. Computational model of solid-state, molecular, or atomic media for FDTD simulation based on a multi-level multi-electron system governed by Pauli exclusion and Fermi-Dirac thermalization with application to semiconductor photonics. *Optics Express* **14**, 3569-3587, (2006).

97 Teixeira, F. L. Time-domain finite-difference and finite-element methods for Maxwell equations in complex media. *Ieee Transactions on Antennas and Propagation* **56**, 2150-2166, (2008).

98 Zhukovsky, S. V., Chigrin, D. N., Lavrinenko, A. V. & Kroha, J. Switchable lasing in multimode microcavities. *Physical Review Letters* **99**, (2007).

99 Oskooi, A. F. *et al.* MEEP: A flexible free-software package for electromagnetic simulations by the FDTD method. *Computer Physics Communications* **181**, 687-702, (2010).

100 Dridi, M. & Schatz, G. C. Model for describing plasmon-enhanced lasers that combines rate equations with finite-difference time-domain. *Journal of the Optical Society of America B-Optical Physics* **30**, 2791-2797, (2013).

101 Scully, M. O. & Zubairy, M. S. *Quantum Optics*. (Cambridge University Press, 1999).

102 Sukharev, M., Freifeld, N. & Nitzan, A. Numerical Calculations of Radiative and Non-Radiative Relaxation of Molecules Near Metal Particles. *Journal of Physical Chemistry C* **118**, 10545-10551, (2014).

103 Sukharev, M. & Nitzan, A. Numerical studies of the interaction of an atomic sample with the electromagnetic field in two dimensions. *Physical Review A* **84**, (2011).

104 Shan, G. C., Bao, S. Y., Zhang, K. & Huang, W. Theoretical study of photon emission from single quantum dot emitter coupled to surface plasmons. *Frontiers of Physics* **6**, 313-319, (2011).

105 Deinega, A. & Seideman, T. Interaction of single quantum emitter and dark plasmon supported by a metal nanoring. *Journal of Chemical Physics* **140**, 5, (2014).

106 Deinega, A. & Seideman, T. Self-interaction-free approaches for self-consistent solution of the Maxwell-Liouville equations. *Physical Review A* **89**, (2014).

107 Sukharev, M., Seideman, T., Gordon, R. J., Salomon, A. & Prior, Y. Ultrafast Energy Transfer between Molecular Assemblies and Surface Plasmons in the Strong Coupling Regime. *Acs Nano* **8**, 807-817, (2014).

108 Lopata, K. & Neuhauser, D. Multiscale Maxwell-Schrodinger modeling: A split field finite-difference time-domain approach to molecular nanopolaritonics. *Journal of Chemical Physics* **130**, (2009).

109 Liu, W. *et al.* Strong Exciton–Plasmon Coupling in MoS2 Coupled with Plasmonic Lattice. *Nano Letters* **16**, 1262-1269, (2016).

110 Zakharko, Y., Graf, A. & Zaumseil, J. Plasmonic Crystals for Strong Light–Matter Coupling in Carbon Nanotubes. *Nano Letters* **16**, 6504-6510, (2016).

111 Wang, Q. H., Kalantar-Zadeh, K., Kis, A., Coleman, J. N. & Strano, M. S. Electronics and optoelectronics of two-dimensional transition metal dichalcogenides. *Nat Nano* **7**, 699-712, (2012).

112 Boghossian , A. A. *et al.* Near-Infrared Fluorescent Sensors based on Single-Walled Carbon Nanotubes for Life Sciences Applications. *ChemSusChem* **4**, 848-863, (2011).

113 Green, A. A. & Hersam, M. C. Nearly Single-Chirality Single-Walled Carbon Nanotubes Produced via Orthogonal Iterative Density Gradient Ultracentrifugation. *Advanced Materials* **23**, 2185-2190, (2011).

114 Wang, F., Dukovic, G., Knoesel, E., Brus, L. E. & Heinz, T. F. Observation of rapid Auger recombination in optically excited semiconducting carbon nanotubes. *Physical Review B* **70**, 241403, (2004).

115 Zakharko, Y. *et al.* Broadband Tunable, Polarization-Selective and Directional Emission of (6,5) Carbon Nanotubes Coupled to Plasmonic Crystals. *Nano Letters* **16**, 3278-3284, (2016).

116 Tran, T. T. *et al.* Deterministic Coupling of Quantum Emitters in 2D Materials to Plasmonic Nanocavity Arrays. *Nano Letters* **17**, 2634-2639, (2017).

117 Purcell, E. M. Spontaneous emission probabilities at radio frequencies. *Phys Rev* **69**, (1946).

118 Koenderink, A. F. On the use of Purcell factors for plasmon antennas. *Optics Letters* **35**, 4208-4210, (2010).

119 Teperik, T. V. & Degiron, A. Superradiant Optical Emitters Coupled to an Array of Nanosize Metallic Antennas. *Physical Review Letters* **108**, 147401, (2012).

120 Guo, K., Verschuuren, M. A. & Femius Koenderink, A. Superresolution imaging of the local density of states in plasmon lattices. *Optica* **3**, 289-298, (2016).

121 Guo, K., Lozano, G., Verschuuren, M. A. & Gómez Rivas, J. Control of the external photoluminescent quantum yield of emitters coupled to nanoantenna phased arrays. *Journal of Applied Physics* **118**, (2015).

122 Miller, D. A. B. Device Requirements for Optical Interconnects to Silicon Chips. *Proceedings of the IEEE* **97**, 1166-1185, (2009).

123 Yang, A., Wang, D., Wang, W. & Odom, T. W. Coherent Light Sources at the Nanoscale. *Annual Review of Physical Chemistry* **68**, 83-99, (2017).

124 Wang, D., Wang, W., Knudson, M. P., Schatz, G. C. & Odom, T. W. Structural Engineering in Plasmon Nanolasers. *Chemical Reviews*, (2017).

125 Westbergh, P., Gustavsson, J. S., Kögel, B., Haglund, Å. & Larsson, A. in *IEEE J. Select. Topics Quantum Electron.* Vol. 17 1603-1613 (IEEE, 2011).

126 Armani, D. K., Kippenberg, T. J., Spillane, S. M. & Vahala, K. J. Ultra-high-Q toroid microcavity on a chip. *Nature* **421**, 925-928, (2003).

127 Takahashi, Y. *et al.* High-Q nanocavity with a 2-ns photon lifetime. *Opt. Express* **15**, 17206-17213, (2007).

128 Tanabe, T., Notomi, M., Kuramochi, E., Shinya, A. & Taniyama, H. Trapping and delaying photons for one nanosecond in an ultrasmall high-Q photonic-crystal nanocavity. *Nat Photon* **1**, 49-52, (2007).

129 Altug, H., Englund, D. & Vučković, J. Ultrafast photonic crystal nanocavity laser. *Nat Phys* **2**, 484-488, (2006).

130 Yu, Z. *et al.* Organic Phosphorescence Nanowire Lasers. *Journal of the American Chemical Society* **139**, 6376-6381, (2017).

131 Stockman, M. I. in *J. Opt.* Vol. 12 024004 (IOP Publishing, 2010).

132 Ma, R. M., Oulton, R. F., Sorger, V. J., Bartal, G. & Zhang, X. A. Room-temperature sub-diffraction-limited plasmon laser by total internal reflection. *Nature Materials* **10**, 110-113, (2011).

133 Siegman, A. E. (1986).

134 Wang, W. *et al.* The rich photonic world of plasmonic nanoparticle arrays. *Materials Today*.

135 Danqing Wang, A. Y., Weijia Wang, Yi Hua, Richard D. Schaller, George C. Schatz and Teri W. Odom. Band-edge Engineering for Controlled Multi-modal Nanolasing in Plasmonic Superlattices *Nature Nanotechnology*, (2017).

136 Maier, S. A. (2007).

137 Park, D. J. *et al.* Directional emission from dye-functionalized plasmonic DNA superlattice microcavities. *Proceedings of the National Academy of Sciences* **114**, 457-461, (2017).

138 Zhou, X. *et al.* Selective Functionalization of the Nanogap of a Plasmonic Dimer. *ACS Photonics* **2**, 121-129, (2015).

139 Zhou, X. *et al.* Two-Color Single Hybrid Plasmonic Nanoemitters with Real Time Switchable Dominant Emission Wavelength. *Nano Lett*, (2015).

140 Bondarev, S. L., Knyukshto, V. N., Stepuro, V. I., Stupak, A. P. & Turban, A. A. Fluorescence and Electronic Structure of the Laser Dye DCM in Solutions and in Polymethylmethacrylate. *Journal of Applied Spectroscopy* **71**, 194-201, (2004).

141 Medishetty, R. *et al.* A New Class of Lasing Materials: Intrinsic Stimulated Emission from Nonlinear Optically Active Metal-Organic Frameworks. *Adv Mater* **29**, (2017).

142 Medishetty, R., Zareba, J. K., Mayer, D., Samoc, M. & Fischer, R. A. Nonlinear optical properties, upconversion and lasing in metal-organic frameworks. *Chem Soc Rev*, (2017).

143 Cui, Y. J., Yue, Y. F., Qian, G. D. & Chen, B. L. Luminescent Functional Metal-Organic Frameworks. *Chemical Reviews* **112**, 1126-1162, (2012).

144 Lydon, J. Chromonic review. *J. Mater. Chem.* **20**, 10071-10099, (2010).

145 Shekhah, O., Liu, J., Fischer, R. A. & Woll, C. MOF thin films: existing and future applications. *Chem Soc Rev* **40**, 1081-1106, (2011).

146 Liu, J. *et al.* Photoinduced Charge-Carrier Generation in Epitaxial MOF Thin Films: High Efficiency as a Result of an Indirect Electronic Band Gap? *Angew Chem Int Ed Engl*, (2015).

147 Gouterman, M. Spectra of Porphyrins. *J. Mol. Spectrosc.* **6**, 138-&, (1961).

148 Bialkowski, B., Stepanenko, Y., Nejbauer, M., Radzewicz, C. & Waluk, J. The dynamics and origin of the unrelaxed fluorescence of free-base tetraphenylporphyrin. *Journal of Photochemistry and Photobiology a-Chemistry* **234**, 100-106, (2012).

149 Hashimoto, T., Choe, Y. K., Nakano, H. & Hirao, K. Theoretical study of the Q and B bands of free-base, magnesium, and zinc porphyrins, and their derivatives. *J. Phys. Chem. A* **103**, 1894-1904, (1999).

150 Yang, A. K. *et al.* Real-time tunable lasing from plasmonic nanocavity arrays. *Nature Communications* **6**, (2015).

151 Hodak, J. H., Martini, I. & Hartland, G. V. Spectroscopy and dynamics of nanometer-sized noble metal particles. *J. Phys. Chem. B* **102**, 6958-6967, (1998).

152 Wang, D. *et al.* Band-edge engineering for controlled multi-modal nanolasing in plasmonic superlattices. *Nat. Nanotechnol.*, (2017).

153 Zengin, G. *et al.* Realizing Strong Light-Matter Interactions between Single-Nanoparticle Plasmons and Molecular Excitons at Ambient Conditions. *Phys. Rev. Lett.* **114**, 157401, (2015).

154 Wang, W. *et al.* The rich photonic world of plasmonic nanoparticle arrays. *Materials Today*, (2017).

155 Zhou, W. *et al.* Lasing action in strongly coupled plasmonic nanocavity arrays. *Nat. Nanotechnol.* **8**, 506-511, (2013).

156 Zhou, W., Hua, Y., Huntington, M. D. & Odom, T. W. Delocalized Lattice Plasmon Resonances Show Dispersive Quality Factors. *Journal of Physical Chemistry Letters* **3**, 1381-1385, (2012).

157 Boghossian, A. A. *et al.* Near-infrared fluorescent sensors based on single-walled carbon nanotubes for life sciences applications. *ChemSusChem* **4**, 848-863, (2011).

158 Klimov, V. I. *et al.* Optical Gain and Stimulated Emission in Nanocrystal Quantum Dots. *Science* **290**, 314-317, (2000).

159 Nomura, M. *et al.* Room temperature continuous-wave lasing in photonic crystal nanocavity. *Optics Express* **14**, 6308-6315, (2006).

160 Resch-Genger, U., Grabolle, M., Cavaliere-Jaricot, S., Nitschke, R. & Nann, T. Quantum dots versus organic dyes as fluorescent labels. *Nature methods* **5**, 763-775, (2008).

161 Belacel, C. *et al.* Controlling Spontaneous Emission with Plasmonic Optical Patch Antennas. *Nano letters* **13**, 1516-1521, (2013).

162 Curto, A. G. *et al.* Multipolar radiation of quantum emitters with nanowire optical antennas. *Nature communications* **4**, (2013).

163 Chan, Y. H. *et al.* Using Patterned Arrays of Metal Nanoparticles to Probe Plasmon Enhanced Luminescence of CdSe Quantum Dots. *Acs Nano* **3**, 1735-1744, (2009).

164 Hu, L. *et al.* Plasmon-Enhanced Surface-State Emission of CdSe Quantum Dots and Its Application to Microscale Luminescence Patterns. *J Phys Chem C* **116**, 11283-11291, (2012).

165 Ureña, E. B. *et al.* Excitation Enhancement of a Quantum Dot Coupled to a Plasmonic Antenna. *Advanced Materials* **24**, OP314-OP320, (2012).

166 D'Agostino, S., Alpeggiani, F. & Andreani, L. C. Strong coupling between a dipole emitter and localized plasmons: enhancement by sharp silver tips. *Optics express* **21**, 27602-27610, (2013).

167 Nepal, D., Drummy, L. F., Biswas, S., Park, K. & Vaia, R. A. Large Scale Solution Assembly of Quantum Dot-Gold Nanorod Architectures with Plasmon Enhanced Fluorescence. *Acs Nano* **7**, 9064-9074, (2013).

168 Song, M. *et al.* Photoluminescence Plasmonic Enhancement of Single Quantum Dots Coupled to Gold Microplates. *The Journal of Physical Chemistry C* **118**, 8514-8520, (2014).

169 Ji, B. T. *et al.* Non-blinking quantum dot with a plasmonic nanoshell resonator. *Nature nanotechnology* **10**, 170-175, (2015).

170 Le-Van, Q. *et al.* Temperature dependence of quantum dot fluorescence assisted by plasmonic nanoantennas. *Phys Rev B* **91**, (2015).
171 Wing, W. J., Sadeghi, S. M. & Campbell, Q. Improvement of plasmonic enhancement of quantum dot emission via an intermediate silicon-aluminum oxide interface. *Appl Phys Lett* **106**, (2015).
172 Kawawaki, T. *et al.* Efficiency Enhancement of PbS Quantum Dot/ZnO Nanowire Bulk-Heterojunction Solar Cells by Plasmonic Silver Nanocubes. *Acs Nano* **9**, 4165-4172, (2015).
173 Rakovich, A., Albella, P. & Maier, S. A. Plasmonic Control of Radiative Properties of Semiconductor Quantum Dots Coupled to Plasmonic Ring Cavities. *Acs Nano* **9**, 2648-2658, (2015).
174 Kayanuma, Y. Wannier excitons in low-dimensional microstructures: Shape dependence of the quantum size effect. *Physical Review B* **44**, 13085-13088, (1991).
175 Schaller, R. D., Agranovich, V. M. & Klimov, V. I. High-efficiency carrier multiplication through direct photogeneration of multi-excitons via virtual single-exciton states. *Nat Phys* **1**, 189, (2005).
176 Stockman, M. I. Spasers explained. *Nature Photonics* **2**, 327-329, (2008).
177 Fan, F. *et al.* Continuous-wave lasing in colloidal quantum dot solids enabled by facet-selective epitaxy. *Nature* **544**, 75-79, (2017).
178 Roberts, G. *Langmuir-blodgett films*. (Springer Science & Business Media, 2013).